OVERLOAD PROTECTION FOR AC-DC TRANSFER MEASUREMENT STANDARDS

by

Thato Ernest Kgakatsi
(216045840)

A Master's research dissertation submitted in fulfilment of the requirements for the degree of

Master of Philosophy
in
Electrical and Electronic Engineering (RD)

Faculty of Engineering and the Built Environment

at the

UNIVERSITY OF JOHANNESBURG

SUPERVISOR: **Dr Johan Venter (UJ)**
CO-SUPERVISORS: **Dr Eugene Golovins (NMISA)**
Prof Dan Valentin Nicolae (UJ)

June 2020

DECLARATION

I, **Thato Ernest Kgakatsi,** hereby declare that this master's research dissertation is wholly my own work and has not been submitted anywhere else for academic credit either by myself or another person. I understand what plagiarism implies and declare that this dissertation is my own ideas, words, phrases, arguments, graphics, figures, results and organisation, except where reference is explicitly made to another's work. I understand further that any unethical academic behaviour, which includes plagiarism, is seen in a serious light by the University of Johannesburg and is punishable by disciplinary action.

Signature: **Date:** 24 April 2020

DEDICATION

This work is dedicated with love to my late mother, Mmanko Fredah Kgakatsi, my grandmother, Mmantshadi Pauline Kgakatsi, my sister, Lerato Kgakatsi, and my family and friends.

ACKNOWLEDGEMENTS

Special thanks go to the National Metrology Institute of South Africa for hosting my research project and for providing me with resources and support.

To my supervisor, Dr Johan Venter, my co-supervisors, Dr Eugene Golovins (also mentor) and Prof Dan-Valentin Nicolae, your support and guidance throughout the journey of this study are greatly appreciated. It was you who introduced me to postgraduate research, and I am not the same as when I started this research project, all thanks to you. Thank you.

To my colleagues, Brian Maboko, Marcus Hlakola and Dr Tshepo Dinoko, thank you for always being there whenever I needed you. You are appreciated.

To my family, especially my grandmother, Mmantshadi Kgakatsi, my uncles, Matlere Kgakatsi and Rapula Kgakatsi, and my aunts, Mmakau Kgakatsi and Matlakala Kgakatsi, thank you for always encouraging me to go an extra mile to achieve the things that have never been achieved by anyone in our family. The role that you have all played in raising this young man, especially after the passing of his mother, cannot go unnoticed. Thank you.

To my friends, Oreabetse Malope, Mmakamohelo Phantsi, Katlego Mooketsi, Rebaone Setsome, Oarabile Maetla and Maximilian Mogoregi, you have always been there for me from the time we became friends. I appreciate you all and I am very grateful to have you as my friends.

To my special friend, Keotshepile Menoe, no words can describe my sincere gratitude for the love, support and encouragement you have given to me ever since we met, especially during the period of this research study. Thank you.

To those who played a role in my journey of career development whom I have not mentioned, you are all highly appreciated, and I will forever be grateful. You have all played a crucial role. Thank you.

ABSTRACT

Electrical transient overloads (ETOs) are inherent to electrical and electronic systems, especially those that are composed of semiconductor materials. However, as the subject has received research attention since the mid-1900s, design engineers are familiar with this class of electrical or electronic disturbance. Thus, in most electrical and electronic applications, ETOs are compensated for through the implementation of an ETO protection device(s). Nevertheless, more work is still to be done to develop efficient techniques to mitigate this class of disturbance.

The work presented in this dissertation identifies the most probable sources of ETOs in the alternating current-direct current (AC-DC) transfer measurement system. The AC-DC transfer measurement system is used to provide electrical calibration services to the national industry and national and regional standardisation bodies, thus complementing the metrological traceability of the international (SI) units of AC current, voltage and power. Thermal converters (TCs), which serve as the main elements of the AC-DC transfer measurement system, are most susceptible to damage and destruction from ETO events, which may arise during the measurement process or be caused by human error. This work also presents a conceptual ETO protection solution for thermal converters, developed through mathematical and simulation analysis.

Possible ETOs in the AC-DC transfer measurement systems could result from human error or systematic errors, thus, implementing an ETO protection circuit at the input circuit of the TCs presents a better chance of protecting them from damage or destruction that could be caused by ETOs.

The findings of this study indicate that the transient voltage suppression (TVS) devices used in this work (Zener diode and metal-oxide varistor) greatly reduce current, voltage and power dissipation magnitudes on the 5 mA nominal current single-junction thermal converter (SJTC). However, since the input ratings of the SJTC in question are very low, neither of the TVS devices in question can offer protection at a low milliampere or sub one volt level; thus, their implementation (even in a multi-stage protection element) does not offer sufficient protection to the SJTC.

TABLE OF CONTENTS

LIST OF TABLES

LIST OF FIGURES

LIST OF ACRONYMS AND ABBREVIATIONS

AC	:	Alternating current
AC-DC	:	Alternating current – direct current
ANSI	:	American National Standards Institute
CDE	:	Cable discharge event
CDM	:	Charged device model
CUT	:	Circuit under test
DC	:	Direct current
DVM	:	Digital voltmeter
EMC	:	Electromagnetic compatibility
EMF	:	Electromotive force
ESD	:	Electrostatic discharge
ETO	:	Electrical transient overload
GPIB	:	General purpose interface bus
HBM	:	Human body model
HE	:	Heater element
HMM	:	Human metal model
HV	:	High voltage
IC	:	Integrated circuit
IEC	:	International electrotechnical commission
IEEE	:	Institute of Electrical and Electronics Engineers

ILT	:	Inverse Laplace transform
I-V	:	Current – voltage
JEDEC	:	Joint Electron Device Engineering Council
LT	:	Laplace transform
MIL-STD	:	Military standard
MJTC	:	Multijunction thermal converter
MM	:	Machine model
MOV	:	Metal-oxide varistor
NMI	:	National Metrology Institute
NMISA	:	National Metrology Institute of South Africa
OrCAD	:	Oregon computer-aided design
PMJTC	:	Planar multi-junction thermal converter
PSpice	:	Personal simulation program with integrated circuit emphasis
REF	:	Reference
RMS	:	Root-mean-square
SI	:	International system of units
SJTC	:	Single-junction thermal converter
SSTC	:	Solid-state thermal converter
TC	:	Thermal converter
TCC	:	Thermal current converter
TE	:	Thermal element

TFMJTC	:	Thin-film multi-junction thermal converter
TJTC	:	Thermocouple-junction thermal converter
TOPD	:	Transient overload protection device
TOPM	:	Transient overload protection module
TS	:	Transfer standard
TVC	:	Thermal voltage converter
TVS	:	Transient voltage suppressor
UHF	:	Ultra-high frequency
UUT	:	Unit under test
V-I	:	Voltage – current

LIST OF SYMBOLS

α_T	:	Thomson coefficient
α_{TC}	:	Temperature coefficient
μ_0	:	Vacuum magnetic permeability
Δv_{Cs}	:	Transition frequency of Caesium
δ	:	AC-DC difference
e	:	Elementary charge
ε	:	Emissivity
ρ	:	Resistivity
σ	:	Stefan-Boltzmann constant

CHAPTER 1: RESEARCH BACKGROUND

1.1 Introduction

The world is in the dawn of the fourth industrial revolution, which puts a lot of strain on the reliability of modern electrical and electronic devices. Therefore, scientific and industrial electrical metrology activities such as calibration, testing and measurement with application to consumer measuring instrumentation and industrial process control equipment are necessary to ensure production competitiveness and improved quality of life. Furthermore, modern electronic devices are facing a rapidly increasing make-over trend, which includes nanoscale sizing and faster operation. However, these and related developments, have led to the increased susceptibility of electronic devices to electric transient overloads (ETOs); therefore, in many electronic device applications, integration of transient overload protection devices (TOPDs) into the design is highly desirable [1].

ETOs are momentary changes in the circuit electrical conditions where the magnitude of either voltage or current, or both, exceeds the maximum rating level(s); thus, a signal with high amplitude and a high energy content is imposed on the circuit. These changes often cause damage (latent or catastrophic) or disturbances in circuit performance. The two commonly known major sources of ETOs are lightning strikes (direct or indirect) and the switching mechanism of the circuit [2][3]. Electrostatic discharges (ESDs) from a charged human being, cable, or even equipment are also considered major sources of ETOs [4]. The robustness of the circuit design is the one factor that determines the capability of the circuit to withstand ETO. This is often achieved by implementing ETO protection measures in the circuit design. Clamp-type transient voltage suppressors (TVSs) with *p-n* junction semiconductor properties, such as the TVS diode, Zener diode and metal-oxide varistor (MOV), are the most commonly used TOPDs [5].

The National Metrology Institute of South Africa (NMISA) develops and maintains high accuracy alternating current – direct current (AC-DC) transfer standards (TSs), which are used to disseminate volt and ampere traceability by calibration of precision AC measuring instruments [6]. The national measurement standards line is represented by thermocouple junction (temperature sensor) thermal converters (TJTCs) and state-of-the-art solid-state (transistor/diode temperature sensor) thermal converters (SSTCs), which are the most accurate commercially available AC-DC TSs [7].

The purpose of this work was to study the possible ETO sources in the AC-DC transfer measurement system and design a conceptual transient overload protection module (TOPM), which would protect the TSs against ETOs. Appropriate protection devices were identified and analysed for steady state and transient state operation modes through mathematical and simulation modelling. Experimental implementation of the solution on an economically viable hardware platform was performed for validation purposes.

The dissertation starts by outlining the background of this study, including the problem identification and the rationale of this work. A literature review about AC metrology is then presented, followed by thermal modelling of a single-junction thermal converter (SJTC). Characterisation of switching and ESD-induced ETOs and their respective defining standards (IEC 61000-4-5 and IEC 61000-4-2, respectively) is presented with reference to the literature study. The most probable sources and paths of ETOs in the AC-DC transfer measurement system are also identified and outlined. Devices and techniques used to protect components and systems against ETOs are discussed and characterised. The methods used to obtain the solution and the findings of this research are presented and discussed as well.

1.2 Research Problem Statement

In the AC-DC transfer measurement system, the customer instrumentation is calibrated by comparison against thermal voltage converters (TVC) or thermal current converters (TCC). The Fluke 792A root-mean-square (RMS) SSTC used for calibration purposes at NMISA has a built-in input TOPD [8], whereas the SJTCs, studied in this work, do not have any embedded TOPD and can be damaged by even a relatively minor short-term increase above the rated input current or voltage [9].

In the AC-DC transfer measurement system, the potential sources of ETOs could be attributed to ESD and the switching mechanisms of the switch used to toggle between the AC and DC input quantities during the measurement process. In the event of an ETO, latent damage to the thermal TS could occur, resulting in the alteration of the device's electric parameters (loss of calibration state) or, in the worst case, catastrophic damage could occur, resulting in the complete destruction of the TS.

A suitable solution to this problem is to apply one or more TOPD, which would be able to divert most of the transient current away from the protected circuit and lower the transient voltage by clamping it to a level lower than or equal to the maximum input rating of the

protected circuit. Thermal converters (TCs) are used for precision measurements where it is imperative to keep the measurement uncertainty low. It means that the implemented TOPD(s) should not influence the uncertainty of the measurements. Therefore, it is necessary to implement a customised solution with the least or no interference for integration into the AC-DC transfer measuring system. Furthermore, it is necessary to understand the architecture and specifications of the precision AC instrumentation and account for a configuration of the measurement circuit in order to identify suitable ETO protection devices.

1.3 Research Questions

ETOs occur within a short period of time and are characterised by fast rising signal waveforms with high amplitude and energy content. These signals pose a greater threat to any circuit or even system of which the design does not account for ETOs exposure. Therefore, the following questions were used as a guideline in the implementation process of a conceptual TOPM solution for the precision AC-DC TS):

- How fast can each of the investigated TVS devices respond to an ETO event? What is the difference between the responses of the TVS devices when used individually and when used simultaneously in a TOPM circuit?
- How much power can each TVS device and the TOPM dissipate (energy absorption capacity)?
- How does the integration of the TOPM into the AC-DC transfer measurement system affect its performance (in terms of accuracy and stability)?

1.4 Research Aim

This research aims to study the possible ETO sources in the AC-DC transfer measurement system, implement a conceptual protection circuit (TOPM) for an AC-DC transfer measurement system and validate the solution through mathematical and simulation analysis methods and experimental implementation.

1.4.1 Research Objectives

- Conduct a research study of the recent advancements in TOPDs and their implementation techniques to yield effective protection capabilities in low-power electronic applications.
- Identify suitable technology for implementing a faster responding and higher energy-absorbing protection circuit with minimal interference to the performance of the AC-DC transfer measurement system.
- Implement mathematical models (solve differential equations resulting from the modelling networks using the Laplace transform (LT) technique) and carry out PSpice simulation analysis (Cadence OrCAD Lite) as part of the conceptual design validation procedure.
- Perform measurement experiments to compare the promising off-the-shelf protective devices that satisfy the application scenario.

1.5 Research Motivation

The precision AC measuring standards are sensitive to ETO stresses. Their exposure to ETOs could result in the alteration of their electric parameters or even cause complete destruction. Therefore, implementation of protection measures against ETOs is necessary to ensure the safety of the measurement standards and the quality of the measurements.

1.6 Research Impact

This research serves as part of the measurement standards safety and measurement quality assurance aspects of the AC-DC transfer project run at NMISA under the Energy Efficiency Programme. It can be established through the literature study conducted during this study that ETO problems (discussed in this work) in the AC-DC transfer measurement systems have not been addressed previously; this study, therefore, contributes to the body of knowledge.

1.7 Research Method

The initial step of this project was to establish an understanding of the subject of ETOs and identify the ETO problem in the AC-DC transfer measurement system, which constitutes the basis of this study. A literature study was conducted to identify a viable technique and TOPD(s)

as a solution. Sources of ETOs, TOPDs and the TS were characterised with reference to the literature review.

The next step was to develop mathematical models using the LT technique to solve the differential equations resulting from analysis of the complete equivalent electrical circuit models representing the ETOs source, TOPDs and the TS. Verification of the results obtained through mathematical analysis was performed by implementing the equivalent electrical circuit models in Cadence Capture and obtaining their simulation results in Cadence PSpice. The feasible TOPDs were then implemented on the experimental platform to compare the hardware measurement results with the ones obtained through mathematical and simulation analysis. A waveform generator was used to generate the arbitrary transient waveform for experimental analysis.

1.8 Scope of the Study and Limitations

The primary focus of this study was the development of a working conceptual TOPM circuit for precision AC-DC TS (ultra-high frequency (UHF) pattern SJTC with 5 mA current rating) using low-power TOPDs such as TVS devices. The proposed solution was verified by comparing mathematical, simulation and experimental results of model analyses.

One major limitation encountered in this study was the absence of commercial ETO testers such as a high-voltage-rated ESD gun or a surge generator. However, the equivalent circuit models that represent these devices were implemented using mathematical models, simulation tools and in-circuit pulse generation of lower amplitude and matching shape to reproduce the standardised signal waveforms of ETO testers.

Another limitation was in the development of mathematical models of the TOPD. These devices are described by nonlinear power-law equations for current and voltage. The LT technique cannot be implemented for nonlinear equations; therefore, they needed to be linearised first.

1.9 Structure of the Dissertation

The general background and rationale for this study are outlined in Chapter 1. The literature survey relevant to this study is presented in Chapters 3, 4 and 5. Original contributions of this

research are presented in Chapters 3, 6 and 7. The conclusions and recommendations of this study are presented in Chapter 8.

Chapter 1: Research background. The background and the rationale of this study are outlined. The objectives and scope of this study are listed. The chapter further describes the scientific methods used in the study to obtain the results. A research output (peer-reviewed conference paper), and the structure of the dissertation are also outlined.

Chapter 2: Electrical AC Metrology. This chapter starts by giving a brief outline of the history of electrical AC metrology and the definition of the SI unit for current. The AC-DC transfer measurement process, instrumentation and formulation used in the establishment of the definition of the AC quantities through the DC electrical standards are discussed. The traceability chain and the method of ensuring global standardisation or dissemination of traceability through calibration are also discussed.

Chapter 3: Modelling a Single-junction Thermal Converter. In this chapter, an equation governing the temperature distribution of the thermal element (TE) of the SJTC due to an applied electric signal is derived. The maximum power dissipation by the TE due to a maximum permissible current is calculated using the temperature-dependent resistance of the TE.

Chapter 4: Transient Overloads. A literature overview presenting the events leading to ETOs is outlined. The standards developed for testing of components and systems qualification for switching and ESD-induced ETOs are further discussed. The equivalent electrical circuit models for reproducing the standardised testing waveforms used for simulation purposes are also presented. Possible ETOs in the AC-DC transfer measurement system and their probable propagation paths are identified and discussed.

Chapter 5: Transient Overload Protection Devices. In this chapter, clamp-type TOPDs such as TVS devices (TVS diode, Zener diode, and MOV) are characterised as part of a literature review. Techniques for obtaining effective protection capabilities are also examined and discussed. The equivalent electrical circuit models representing the operational states of the TOPDs are characterised for further modelling in the mathematical and simulation analysis platforms.

Chapter 6: Research Method. This chapter presents the methods used for the analysis of the response of the SJTC to ETOs when protection measures are not implemented and when they are implemented. The equivalent circuit models are presented, and the model parameters are analysed.

Chapter 7: Research Findings and Discussion. The findings of this research project are presented and discussed in this chapter.

Chapter 8: Conclusions and Recommendations. This chapter presents the general conclusions of this dissertation. The findings, accomplishments and recommendations are presented.

1.10 List of Publications

Peer-reviewed conference paper:

- Thato E. Kgakatsi, Eugene Golovins, Johan Venter, Dan V. Nicolae, "Protection against transient overvoltage in precision AC-DC transfer measurement system," Proc. SPIE 11043, Fifth Conference on Sensors, MEMS, and Electro-Optic Systems (SMEOS 2018), 110430X (24 January 2019); DOI: 10.1117/12.2501142.

CHAPTER 2: ELECTRICAL AC METROLOGY

2.1 Introduction

The unit for electrical current, called the ampere (A), is one of the seven fundamental SI base units and other electric metrological units are derived from the ampere [10]. The ampere was previously defined through the magnetic force between parallel electric current-carrying conductors with the ability to hold the numerical value of vacuum magnetic permeability constant μ_0 [10]. However, quantum DC electrical standards could not correlate with this definition. This led to the present definition, which came into effect on 20 May 2019, based on a fixed numerical value for an elementary charge *e*, equal to $1.602\ 176\ 634 \times 10^{-19}$ Coulomb (C) or Ampere-second (A· s), where the SI unit for time (second (s)) is defined in terms of the hyperfine transition frequency of Caesium $\Delta\nu_{Cs}$, equal to $9\ 192\ 631\ 770$ oscillations per second (s^{-1}). Hence, the present definition of ampere is given by:

$$1\ \mathrm{A} = \frac{e}{1.602\ 176\ 634 \times 10^{-19}} \cdot \frac{\Delta\nu_{Cs}}{9\ 192\ 631\ 770} = 6.789\ 686\ 817 \times 10^{8} \Delta\nu_{Cs} \qquad (2.1)$$

The realisation of the ampere depends on quantum DC electric standards for volt and ohm, and the relationship is established through Ohm's law [11]. The measurement standards are used to define a unit or reproduce the value(s) of a measurand (the unit representing a measured quantity) to serve as a reference measurement standard (etalon).

Several methods of establishing traceable AC measurements exist; however, a method called AC-DC thermal transfer, using the heating characteristics of a TC, is by far the most precise and commonly used method [12][13]. A TC is an electro-thermic device that uses the thermal effects produced by the RMS value of AC quantity and DC quantity on a resistive heater element (HE) to establish the relationship between the applied AC quantity and the known DC quantity by measuring their power dissipation on the HE.

In this chapter, the definition of the unit for electrical current is presented. A method of realising the AC electrical quantities using TC, called AC-DC thermal transfer, and the mathematical expressions associated with AC-DC thermal transfer are outlined.

2.2 AC-DC Transfer

Unlike the definition of DC quantities, the definition of AC quantities has not been established through absolute standards. Instead, their definition relies on quantum DC electric standards (as seen in Figure 2.1), the quantised Hall effect standard (resistance standard) and Josephson standard (voltage standard).

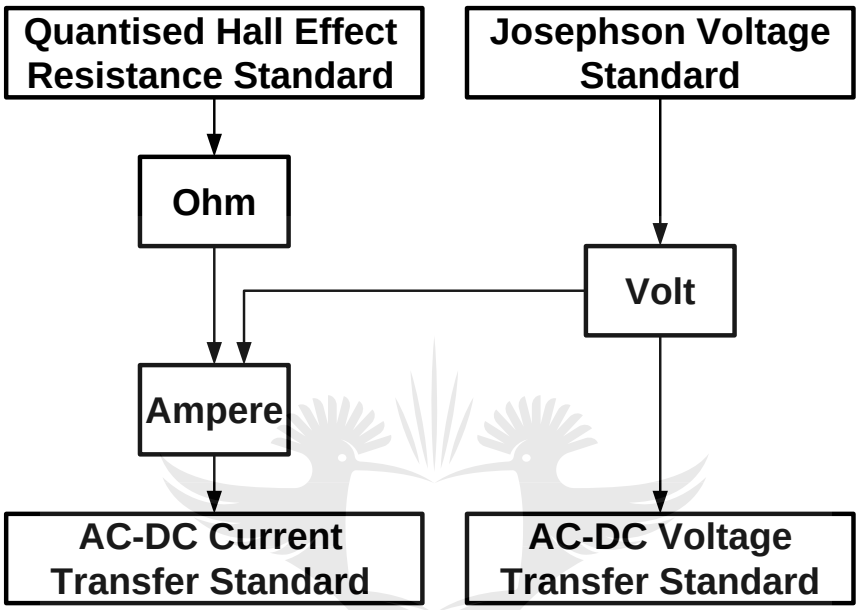

Figure 2.1: Realisation of AC current and voltage standards through DC standards [11]

The TCs are the key components in the realisation of the definition of AC quantities. When an electric signal is applied through a resistive HE of a TC, the energy content of the applied signal is revealed as a temperature rise on the HE [14]. Hence, power is dissipated by the HE, which is directly proportional to the square of the applied electric quantity (current or voltage) that leads to a temperature increase on the HE. In the case where an AC signal is applied on the HE, the power dissipated by the HE is proportional to the square of the RMS value of the AC input quantity:

$$P_{diss} = R_{HE} \times i_{rms}^2 = \frac{v_{rms}^2}{R_{HE}} \tag{2.2}$$

where

- R_{HE} is the electrical resistance of the HE, and

- $i_{rms} = \sqrt{\frac{1}{T_{per}} \int_0^{T_{per}} i^2(t) \times dt}$ and $v_{rms} = \sqrt{\frac{1}{T_{per}} \int_0^{T_{per}} v^2(t) \times dt}$; with $i(t)$ and $v(t)$ being the arbitrary periodic signals, and T_{per} being the period of the signal.

The applied electrical quantity Q_{app} is related to the output thermal voltage (EMF) E through a power law [15]:

$$E = k_{cons} \times Q_{app}^{n} \tag{2.3}$$

where

- k_{cons} is a constant, and
- $n = \frac{\Delta E/E}{\Delta Q_{app}/Q_{app}}$ is the exponent of the TC.

The relationship between the AC and DC quantities is established by determining the value of the AC quantity, which results in the same output EMF as the predetermined or known value of the DC quantity. If the TC was ideal, the relationship between AC and DC quantities required to give the same EMFs, (E_{AC}) and (E_{DC}), would be:

$$Q_{AV} = Q_{DC}|_{E_{AC}=E_{DC}} \tag{2.4}$$

where Q_{AC} and Q_{DC} are either current (A) or voltage (V) corresponding to AC and DC, respectively. However, a real TC is subject to intrinsic errors, which causes a divergence between the AC and DC quantities required to give the same EMF. This divergence is often referred to as the AC-DC difference (δ_{AC-DC}) and it is conventionally expressed in µV/V or parts per million (ppm) as:

$$\delta_{AC-DC} = \frac{Q_{AC}-Q_{DC}}{Q_{DC}}\Big|_{E_{AC}=\frac{1}{2}(E_{DC_-}+E_{DC_+})}. \tag{2.5}$$

The mean of both positive and negative polarities of the DC response must be taken to satisfy Eq. (2.5). After rearranging Eq. (2.5), the relationship between the AC (Q_{AC}) and DC (Q_{DC}) quantities required to give the same EMFs is given as:

$$Q_{AC} = (1 + \delta_{AC-DC})Q_{DC}|_{E_{AC}=\frac{1}{2}(E_{DC_-}+E_{DC_+})}. \tag{2.6}$$

The effect of Eq. (2.6) is that the measured AC quantity required to produce the same power dissipation effects on a nonideal TC as the known DC quantity is dependent on the magnitude of δ_{AC-DC}. A positive δ_{AC-DC} indicates that more AC than DC quantity was required to produce the same EMF and the opposite holds true for a negative δ_{AC-DC}. The presence of δ_{AC-DC} of a TC is owed to a number of factors, which are inherent to the materials and construction of a TC or the system used with a TC [9][11]. However, the most common major contributors to δ_{AC-DC} of a TC are related to its input circuit frequency response and thermoelectric effects [16], and can be expressed as:

$$\delta_{AC-DC} \cong \delta_{LF}(f) + \delta_{HF}(f) + \delta_{thermoelectric-effect} \tag{2.7}$$

where $\delta_{LF}(f)$ and $\delta_{HF}(f)$ are the low and high frequency-generated AC-DC differences, respectively, and $\delta_{thermoelectric-effect}$ is the thermoelectric effect AC-DC difference. Using Eq. (2.7), Eq. (2.6) can be expressed as:

$$Q_{AC} \cong \left(1 + \delta_{LF}(f) + \delta_{HF}(f) + \delta_{thermoelectric-effect}\right) Q_{DC}|_{E_{AC}=\frac{1}{2}(E_{DC_-}+E_{DC_+})}. \tag{2.8}$$

2.2.1 Major Sources of AC-DC Difference of a Thermal Converter

Low-frequency errors

At frequencies below 100 Hz, double frequency thermal oscillations (thermal ripples) are observed. This is due to the insufficient thermal inertia created by the shorter thermal time constant.

High-frequency errors

At frequencies higher than 10 kHz, the skin effect of the conductor and the stray reactance (resistance due to capacitance and inductance components) in the input circuit influence the measurements.

Thermoelectric effects errors

A DC signal gives rise to reversal errors in the measurements owing to the Thomson effect on the HE and Peltier effects at the HE and conductive input lead junctions (dissimilar materials). However, the errors are often minimised by taking the mean of the responses of both polarities of the DC signal.

2.3 AC-DC Thermal Converter

A TC basically constitutes a resistive wire (HE), through which an electrical quantity is applied, and a thermal sensor for detection and measurement of the heating effects imposed on the HE by the applied signal. Two classes of TCs have been developed to date – TJTCs and the SSTCs [7] – which are discussed in Sections 2.3.1 and 2.3.2, respectively. The TJTCs include the SJTC, multi-junction thermal converter (MJTC) and the thin-film (planar) multi-junction thermal converter (TFMJTC or PMJTC), whereas state-of-the-art SSTCs are among others the patented Fluke 792A and Fluke 5790B.

2.3.1 Thermojunction Sensor Thermal Converters

The SJTC was the first AC-DC thermal transfer device to be used for precision measurement of AC quantities. Then the MJTC was developed to reduce the errors due to the thermoelectric effects observed in the SJTC. The TFMJTC was subsequently developed through semiconductor manufacturing technology to improve the performance of the MJTC [16]. A thermocouple junction attached to the HE is the main sensor device, through which the Seebeck effect (conversion of thermal energy into an electrical signal) takes place [17]. The TJTCs suffer from several drawbacks, which make the SSTCs preferable over them. These include longer settling time, lower output thermal voltage, inability to withstand even moderate ETOs and long, difficult and expensive calibration processes [18]. SJTCs, MJTCs and TFMJTCs are each briefly characterised as described below.

2.3.1.1 Single-junction Thermal Converters

Prior to their development as AC-DC TSs, SJTCs were used in radio frequency measurements in the early 1940s [13]. Hermach then developed them as TCs in the mid-1900s [12] and later reviewed the subject of AC-DC thermal transfer in the 1970s before Inglis continued the work in the 1980s [11][19]. Figure 2.2 presents a schematic diagram of a UHF-pattern SJTC with its full-scale image [20]. The device comprises an HE, a thermocouple attached to the midpoint of the HE and the conductive input and output leads. A signal is applied to the HE through the conductive input leads. The conductive output leads are connected to a nanovolt detector for measuring the EMF. The glass or ceramic bead provides electrical insulation and thermal conduction between the HE and the thermocouple junction. The structure, including a certain portion of the conductive input and output leads, is enclosed in a vacuumed glass bulb to

minimise external thermal influence. The advantages and limitations presented by the SJTC are listed in Table 2.1.

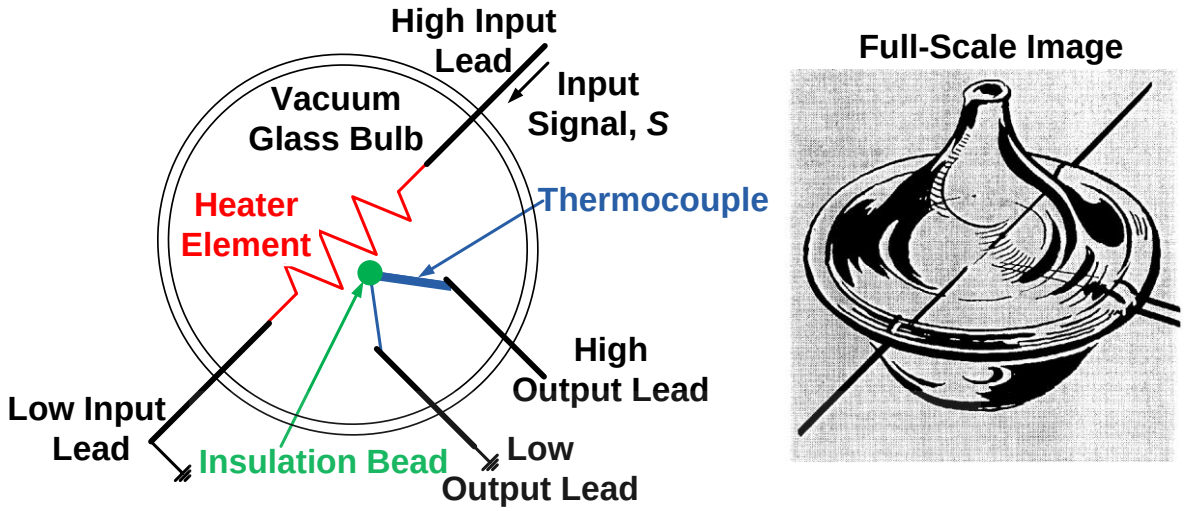

Figure 2.2: Schematic diagram of a UHF-pattern single-junction thermal converter with its full-scale image [20]

Table 2.1: Advantages and disadvantages of SJTC [9][11][16][21]

Advantages	**Limitations**
Small size and low cost	Difficult to manufacture and mass-produce
Applicable to a wide range of frequencies	Maximum input voltage and current are approximately a few hundreds of milli-volt and tens of milliampere, thus any input signal slightly above the threshold will destroy the HE
	Lower output EMF, about 7 mV to 12 mV at full-scale input, which makes measurement difficult and may lead to high measurement uncertainty
	Measurement errors due to higher thermoelectric effects

2.3.1.2 Multi-junction Thermal Converters

The design of MJTCs was developed by Wilkins in the 1970s-1980s [11][13]. The purpose was to improve the performance of the SJTC by reducing thermoelectric errors on the SJTCs. Figure 2.3 presents a schematic diagram of a typical MJTC. The MJTC consists of multiple

series-connected thermocouples (as many as 200 or more [11]) with their junctions attached and distributed on the entire length of a twisted bifilar HE to sample the temperature of the HE [22]. Table 2.2 presents the advantages and limitations offered by MJTC.

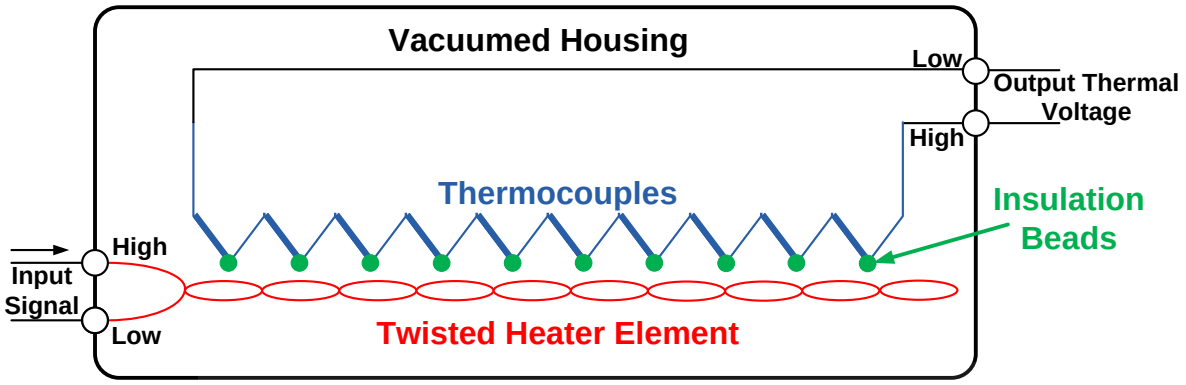

Figure 2.3: Generic schematic of the multi-junction thermal converter [22]

Table 2.2: Advantages and disadvantages of MJTC [7][9][23]

Advantages	**Limitations**
Higher output EMF, approximately 100 mV to 120 mV at full-scale input, which is easier to measure	Expensive compared to the SJTC, and difficult to construct owing to the complexity of their structure, therefore difficult to mass-produce
Distribution of thermocouples along entire HE greatly reduces thermoelectric errors	Frequency response range limited from approximately 30 Hz to 10 kHz
	Errors due to dielectric losses

2.3.1.3 Thin-film Multi-junction Thermal Converters

TFMJTCs were developed by Klonz in the late 1980s [11]. The design was developed as a revision of MJTC HE material and its construction technique was based on modern semiconductor fabrication technology [17]. The design features a Ω-shaped HE and thermocouples distributed on the HE, as presented in Figure 2.4 [22][24]. Table 2.3 presents the advantages and limitations offered by TFMJTCs.

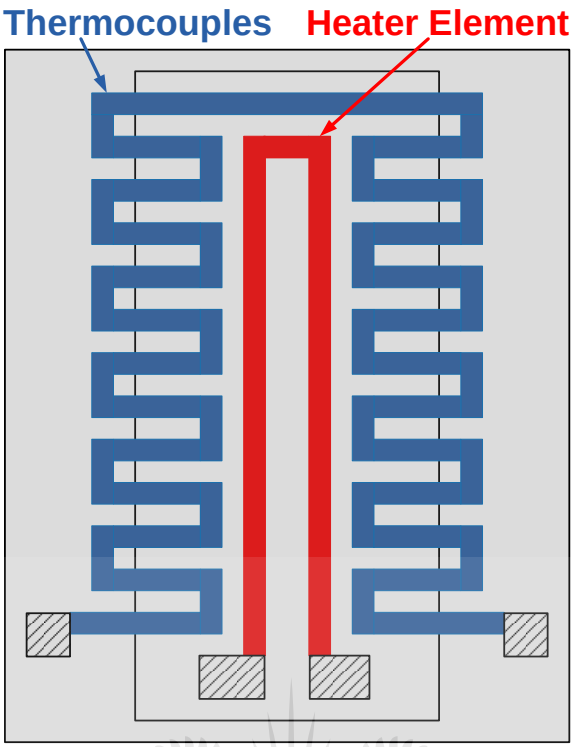

Figure 2.4: Thin-film multi-junction thermal converter [22]

Table 2.3: Advantages and disadvantages of TFMJTC [11][24]

Advantages	**Limitations**
Not difficult to manufacture or mass-produce since their design is based on modern semiconductor fabrication technology	Significant errors are observed at higher frequencies owing to current leakage paths through the silicon structure
Production technology allows adjustment of the thermal settling time constant	Complex and costly

2.3.2 Solid-state Sensor Thermal Converters

SSTCs were developed to improve the accuracy of AC voltage measurements offered by TJTCs. The temperature-sensitive junctions of solid-state devices (transistor and diode) are used as thermal sensors instead of the thermocouple [9][25]. The Fluke 792A solid-state RMS TC, discussed in this work, is the most commonly used SSTC. SSTCs are preferable over their counterparts (TJTCs) because of the shorter thermal time constant (shorter settling time), higher output EMF, embedded input protection, and lower drift rate [26].

2.3.2.1 Fluke 792A

The Fluke 792A was developed by the Fluke Corporation in the 1990s [18]. The standard uses the base-emitter junction of bipolar transistors as the thermal sensor and resistive HEs for accurate conversion between the RMS value of an AC quantity and a DC quantity [14]. The schematic diagram of a TC with a transistor-based solid-state RMS sensor is presented in Figure 2.5. The bipolar junction transistor sensor T_1 detects the heat generated on the input HE H_1, which then unbalances the amplifier. The amplifier eventually develops an output voltage sufficient to energise the output HE H_2 and be detected by transistor sensor T_2, which is supposedly at the same temperature as T_1 [5]. The advantages and limitations offered by this standard are presented in Table 2.4.

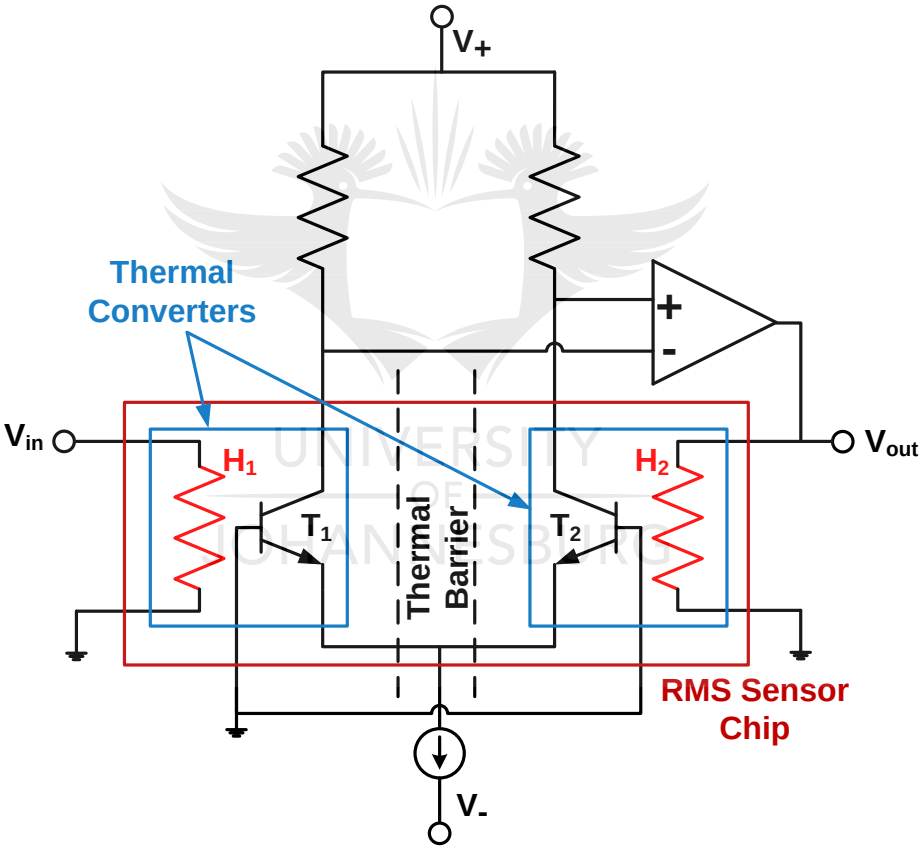

Figure 2.5: Solid-state thermal converter [14][20]

Table 2.4: Advantages and disadvantages of the SSTC [18]

Advantages	**Limitations**
High and precise output EMF, approximately 2 V for full-scale input (2 mV to 1 kV over a frequency range 10 Hz to 1 MHz), which does not need a sophisticated detector to measure	Poor performance with low-frequency inputs due to the shorter thermal time constant (shorter settling time)
Protected against ETOs	
Shorter settling time constant	

2.4 AC-DC Difference

2.4.1 Traceability of AC Quantities

In the event of calibration of the customer's precision AC measuring equipment, the unit under test (UUT) is measured against a reference (REF) TVC (a series combination of a TC and a range resistor) or TCC (a parallel combination of a TC and a shunt resistor), depending on whether it is the voltage or current that is being measured on the UUT. The uncertainty of the measurand is established through post-calibration calculations and indicated in the calibration certificate. The uncertainty of measurement is a measured and calculated doubt of the instrument's accuracy and defines the range in which the expected value is found. Another term, often confused with uncertainty, is measurement error, which is defined as the difference between the measured value and the true value of the measurand.

2.4.2 AC-DC Difference Measurement

NMISA provides traceability for AC current and voltage measurements in the audio-frequency range by calibration of customer equipment or TSs in comparison with a reference standard whose AC-DC difference has been carefully established. Calibrations of the TVCs and TCCs rated from 2 mV to 1 kV over a frequency range of 10 Hz to 1 MHz [28] and 2 mA to 100 A over a frequency range of 10 Hz to 100 kHz [29], respectively, are performed through a dual method [27], using an automated measurement system (Figure 2.6).

The automated measurement system consists of

- an IEEE-488.2 network, through which the equipment is remotely controlled using in-house built computer software,
- a programmable source with both AC and DC output embedded in one unit,
- a microcontroller-driven AC-DC relay latching switch,
- a UUT (either a lower accuracy TS or precision AC metering equipment) and REF thermal TS (either TVS or TCC), and
- two digital voltmeters (DVMs) (one connected to a UUT and the other one to a REF) [28][29]. The output readouts by the DVMs are sampled and recorded on a computer.

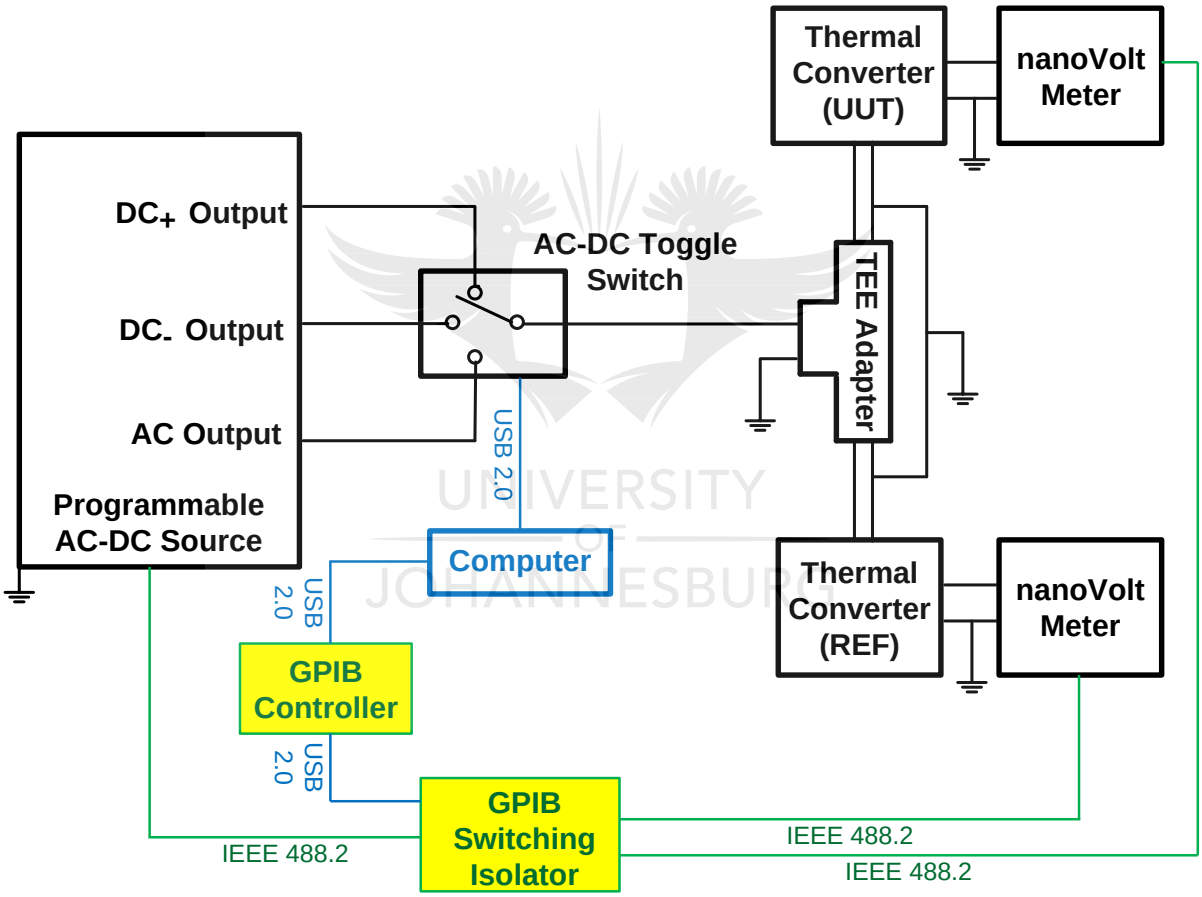

Figure 2.6: AC-DC difference measurement setup or system

The automated measurement system presents a number of advantages, [15][30], such as:

- Measurements are faster and more accurate.
- Fewer human errors occur, since automation ensures minimal human involvement.

However, like any other system, the automated measurement system has imperfections leading to performance limitations [15], such as:

- The limitations of the AC output from the programmable source presents a constraint in the voltage, current and frequency ranges over which the automated system can be used.
- Interference occurs owing to system components' interaction.
- Digital short-time events (transients) occur.
- The reversal of the polarities of the DC quantity is slower.

For voltage measurements, the AC voltage output of the programmable source and the output of an auxiliary amplifier are coupled to share the same output (Figure 2.7(a)) [28]. For current measurements, the output of the AC-DC toggle switch is connected to the transconductance amplifier (Figure 2.7(b)) [29], which serves as a buffer between the low power constant voltage circuit and higher power voltage-controlled current circuit.

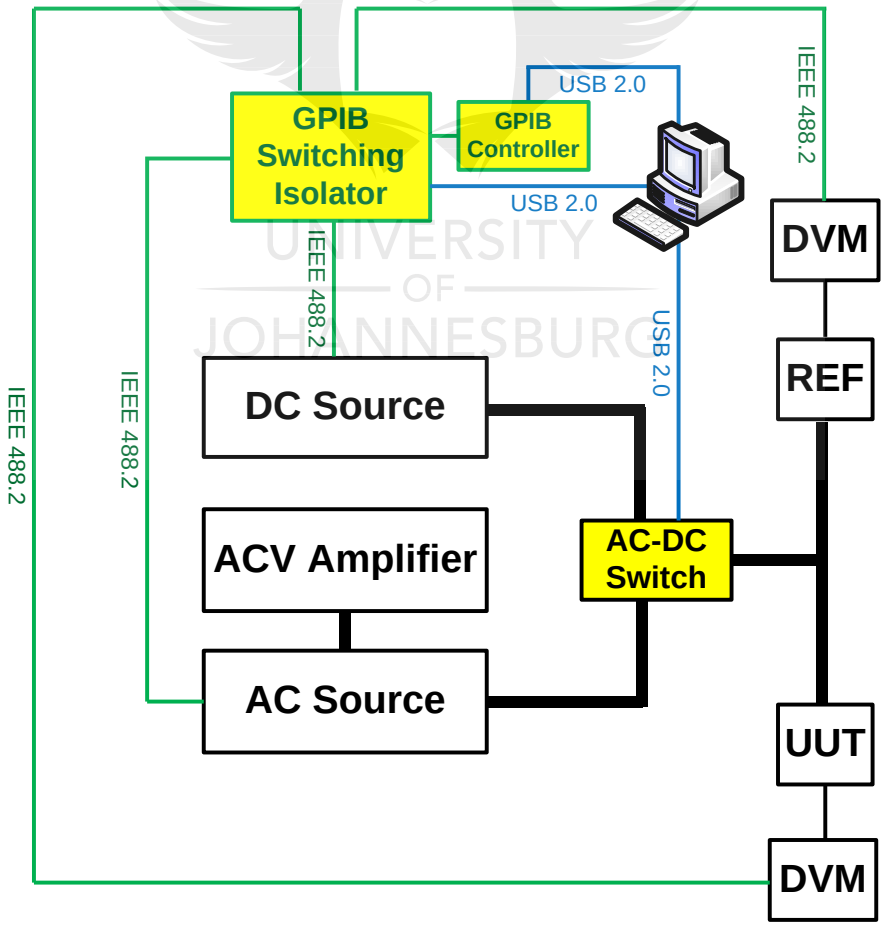

(a)

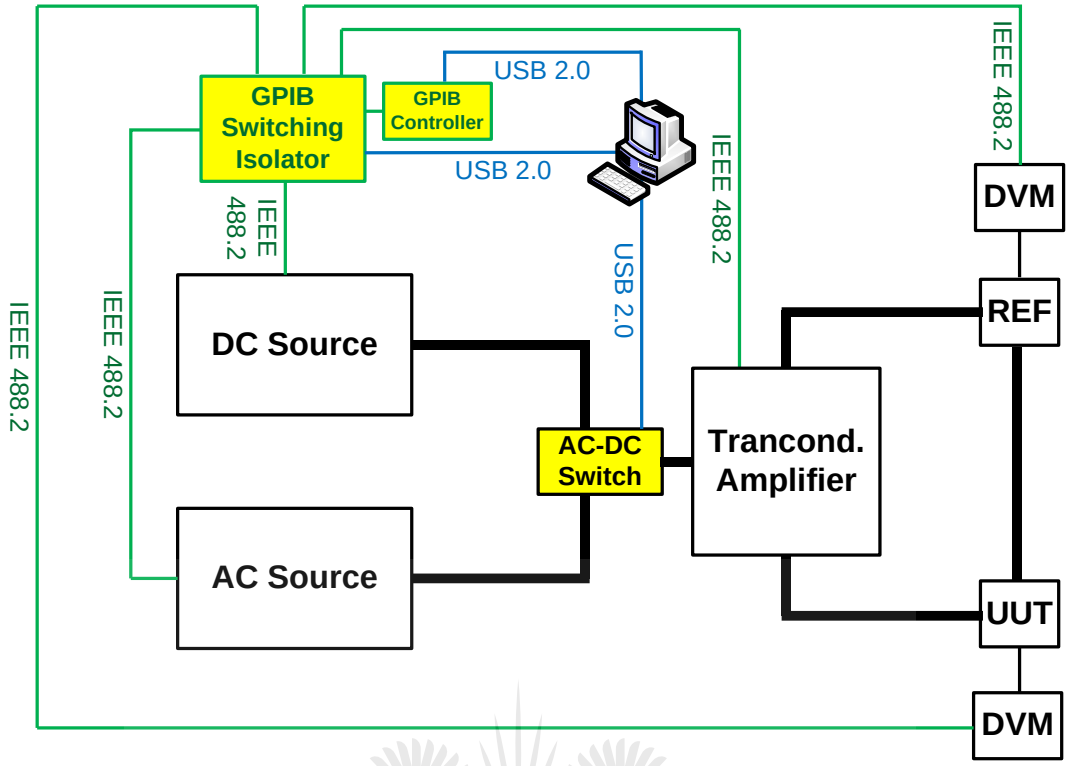

(b)

Figure 2.7: AC-DC transfer measurement schematic diagrams: (a) setup for voltage-transfer measurement [28], (b) setup for current-transfer measurement [29]

2.4.3 Calculation of the AC-DC Difference Standards and Instruments

The AC-DC difference between the UUT and REF standard is measured by a typical automated measurement system shown in Figure 2.6. A measurement sequence with time intervals of about 35 s is used to determine at least one AC-DC difference sample [28][29]:

$$AC_1, DC-, AC_2, DC+, AC_3$$

Each of the AC-DC difference samples is approximated by Eq. (2.9), following the above measurement sequence:

$$\delta_{UUT} \equiv \frac{E_{AC,REF}-E_{DC,REF}}{n_{REF}\cdot E_{DC,REF}} - \frac{E_{AC,UUT}-E_{DC,UUT}}{n_{UUT}\cdot E_{DC,UUT}} + \delta_{REF} \tag{2.9}$$

where

- $E_{DC} = \frac{1}{2}\,(E_{DC-} + E_{DC+})$ and $E_{AC} = \frac{1}{3}\,(E_{AC_1} + E_{AC_2} + E_{AC_3})$ are the mean output EMF of the REF and UUT due to DC and AC input signals, respectively,
- δ_{REF} is the pre-established AC-DC transfer difference of the REF standard, and
- n_{REF} and n_{UUT} are the normalised exponent coefficients of the REF and UUT, respectively.

2.5 Conclusions

In this chapter, the unit for electrical current was defined. A method of establishing the definition of the AC electric quantities through quantum DC electric standards, called AC-DC thermal transfer, was outlined. Furthermore, commercially available and more accurate TCs were characterised and compared. The TC output response deviations between the AC and DC quantities (AC-DC difference) were discussed and further expressed mathematically.

CHAPTER 3: MODELLING A SINGLE-JUNCTION THERMAL CONVERTER

3.1 Introduction

The UHF-pattern SJTC briefly characterised in Section 2.3.1.1 and presented schematically in Figure 2.2 is studied in this work. Since no special care is needed for the electrically isolated TC output circuit, only the input circuit is considered for ETOs' modelling. The devices consist of a fine Evanohm or Nickel-Chromium alloys wire (HE, with low thermoelectric effects [31]) and conductive input Evanohm (or even Platinum or Dumet) lead wires [32][33]. A thermocouple junction is attached to the midpoint of the HE with a ceramic or glass bead to provide electrical insulation and thermal conduction between the HE and the thermocouple. The HE, thermocouple, glass bead and a certain portion of the conductive lead wires are all enclosed in vacuumed glass to minimise the thermal influence from the surroundings.

In this chapter, the UHF-pattern SJTC is modelled for thermal characteristics and its maximum power dissipation (by the HE) is determined by means of calculations.

3.2 Thermal Model of a Single-junction Thermal Converter

Figure 3.1 presents a schematic diagram with the boundary conditions of the HE position x_H and temperature T_H used to determine the thermal characteristics of the UHF-pattern SJTC. An HE of length L, approximately 5 mm (suspended between the conductive lead wires), 10 µm in diameter, is heated by an electric current (I_{AC} or I_{DC}) when it is applied. The thickness of the conductive lead wires (approximately 250 µm in diameter) ensures that heating occurs on almost the entire HE, leaving the conductive leads relatively cooler [19][34]. This could be explained by the inversely proportional relationship between the thermal resistance and the cross-sectional area of the conductor (the larger the cross-sectional area, the smaller the resistance) [35][36]. The junctions formed by the HE and conductive leads are kept at a temperature of about 293 K. Nonetheless, the temperatures of the HE-lead junctions at the beginning ($x_H = 0$) and the end ($x_H = L$) of the HE are given by $T_H(0) = T_0$ and $T_H(L) = T_L$, respectively. A thermal conductor (bead) is connected at the midpoint of the HE. It is assumed that all the HE heat losses by conduction are through heat flow to the HE-lead junctions and through the bead to the thermocouple junction (where the Seebeck effects take place and the output is measured as voltage). Since the system is in a vacuum seal, there are no convection

heat losses [37] and the radiation heat losses from the HE are small enough to be neglected. The Peltier heating or cooling effects are also neglected, since they are independent of the length of the HE.

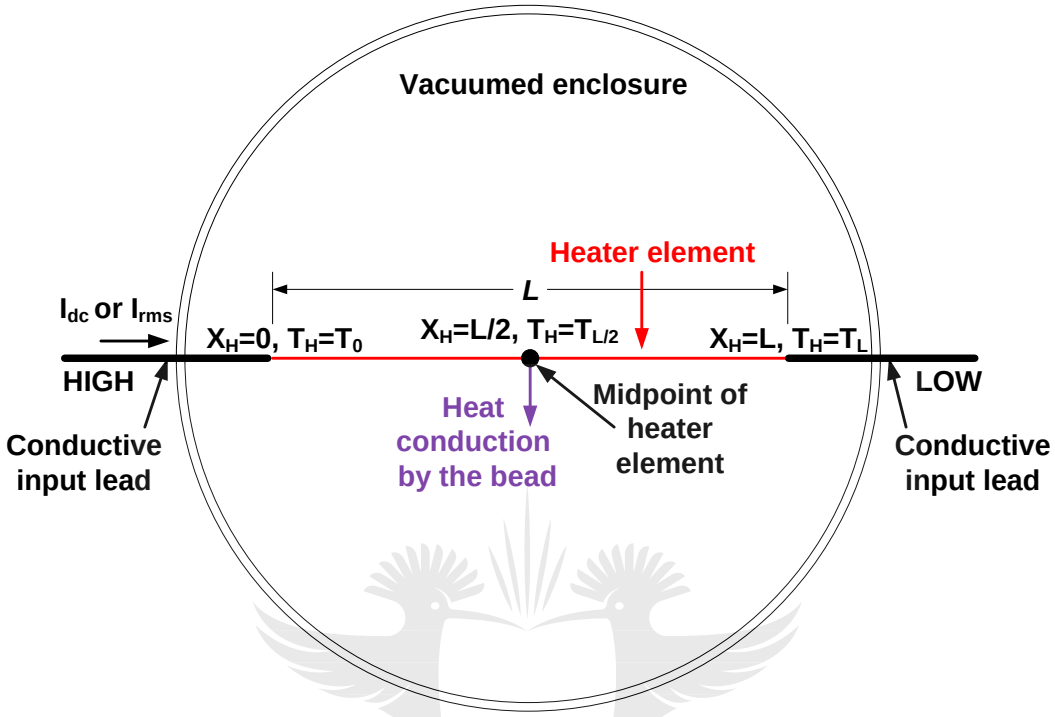

Figure 3.1: Schematic diagram of a UHF-pattern SJTC

Assuming that the temperature is uniform at any cross-sectional surface of the HE, the system is one-dimensional, and the complete modelling equation for the temperature distribution, $T_H(x_H, t)$, of an HE of a vacuum SJTC heated by current I, is given by [34][38]:

$$A_H k_H \frac{d^2 T_H(x_H,t)}{dx_H^2} - \alpha_T I \frac{dT_H(x_H,t)}{dx_H} + \frac{I^2 \rho_H}{A_H} = A_H m_H s_H \frac{dT_H(x_H,t)}{dt} \tag{3.1}$$

where the terms on the left side of Eq. (3.1) are the thermal conduction, Joule heating created by the flow of electric current, Thomson heat absorption (hence, minus sign), and radiation heat losses, respectively, and the term on the right side of Eq. (3.1) presents the rate of heat gained at any point or position of the HE. Table 3.1 presents the symbols in Eq. (3.1).

Table 3.1: Symbols of the heat flow equation

Symbol	Description
A_H	Area of the cross-section of the heater element (m^2)
α_T	Thomson coefficient of the heater (V/K)
I	Applied current (A)
k_H	Thermal conductivity of the heater wire (W/m K)
ρ_H	Resistivity of the heater wire (Ω m)
m_H	Mass density of the heater element (kg/m^3)
s_H	Specific heat of the heater element (J/kg K)
x_H	Position at which the temperature of the heater is measured (m)
t	Time (s)

For steady-state operations, $\frac{dT(x_H,t)}{dt} = 0$ [39]; therefore, Eq. (3.1) becomes a second-order nonhomogeneous linear differential equation, whose general solution is found using a method of integrating factor (derivation in Appendix A):

$$T(x_H) = \frac{I\rho_H}{\alpha_T A_H} x_H + C_1 \frac{A_H k_H}{\alpha_T I} e^{\frac{\alpha_T I}{A_H k_H} x_H} + C_2 \tag{3.2}$$

where $C_1 = \frac{T_0 - T_L + \frac{I\rho_H}{\alpha_T A_H} L}{\frac{A_H k_H}{\alpha_T I}\left(1 - e^{\frac{\alpha_T I}{A_H k_H} L}\right)}$ and $C_2 = \frac{T_0 e^{\frac{\alpha_T I}{A_H k_H} L} - T_L + \frac{I\rho_H}{\alpha_T A_H} L}{\left(1 - e^{\frac{\alpha_T I}{A_H k_H} L}\right)}$ are the constants of integration found using the boundary conditions ($T_H(0) = T_0$ and $T_H(L) = T_L$) of the HE temperature distribution. Equation (3.2) is similar to the general solution obtained by Widdis [37]. Simplifying Eq. (3.2) further results in:

$$T_H(x_H) = T_0 + \frac{I\rho_H}{\alpha_T A_H} x_H - \left(T_0 + T_L - \frac{I\rho_H}{\alpha_T A_H} L\right)\left(\frac{1 + e^{\frac{\alpha_T I}{A_H k_H} x_H}}{1 - e^{\frac{\alpha_T I}{A_H k_H} L}}\right). \tag{3.3}$$

The effect of Eq. (3.3) is that it provides the temperature at a particular cross-sectional position of the HE, assuming a steady-state operation and a constant current. The exponential terms also account for the nonlinearity of the temperature distribution due to the thermoelectric effects and other internal heat sources [39]. The first derivative of Eq. (3.3) with respect to x_H and

multiplication by $-k_H A_H$ gives the rate of heat conduction or heat flux at a particular HE position x_H.

3.3 Power Dissipation by the Single-junction Thermal Converter

The resistive component of the HE of the SJTC is responsible for the Joule heat generation and power dissipation. Appendix B contains the technical information and datasheet of the vacuo-junction SJCTs, where their respective DC resistance values are published. These resistance values correspond to certain reference temperature values of the HE within a vacuumed glass enclosure. The well-known relationship between the dependence of a conductor (HE in this case) and temperature variations is given by:

$$R_H(T) = R_{H_0}(T_0)(1 + \alpha_{TC}\Delta T) \tag{3.4}$$

where R_H is the resistance (Ω) of the HE corresponding to a particular temperature T (K), which is measured at a particular time after energising the HE by an electrical signal, R_{H_0} is the resistance (Ω) of the HE corresponding to the reference temperature T_0 (K) measured before energising the HE, ΔT is the difference between temperatures T and T_0, and α_{TC} is the temperature coefficient of the resistivity (K^{-1}) of the HE.

For a UHF-pattern SJTC with a 5 mA nominal current, the resistance of the Nichrome (80% Ni and 20% Cr) HE at a reference temperature of $T_0 = 293$ K is $R_H = 90$ Ω (Appendix B). This HE only allows a maximum of $I_{max} = 12.5$ mA (250% of the nominal current) input current. Any current input greater than the set threshold constitutes an energy level that could potentially damage or destroy the HE. It was established that the temperature rise in a vacuumed UHF-pattern SJTC could as high as 423 K [37] and its corresponding temperature coefficient of electrical resistivity is $\alpha_H = +0.0001\ K^{-1}$ (Appendix B). Therefore, using Eq. (3.4), the resistance of this Nichrome HE corresponding to the temperature rise of 423 K is $R_H(423\text{ K}) = 91.17$ Ω, where $\Delta T = 130$ K. The power dissipation by the HE energised to a maximum operating temperature by the maximum permissible current input is given by:

$$P_{H_{max}} = R_H(423\ K) \times I_{max}^2 = 14.25\text{ mW} \tag{3.5}$$

This corresponds to the maximum power that the HE will dissipate if energised by a maximum permissible current input. Consequently, if the input signal is a voltage corresponding to a resistance $R_H(423\text{ K})$, i.e., $V_{max} = I_{max} \times R_H(423\text{ K}) = 1.14$ V, the maximum power

dissipated by the HE because of this voltage input is also 14.25 mW. If the input current or voltage is set to a value greater than 12.5 mA or 1.14 V, the HE is expected to dissipate power greater than 14.25 mW, and this could potentially damage or destroy the HE.

3.4 Conclusions

In this chapter, the UHF-pattern SJTC was characterised and modelled for thermal characteristics. The geometry of the input circuit of the SJTC was outlined and characterised in preparation for modelling the thermal characteristics. The general solution governing temperature distribution of the HE energised by a positive DC current was established; a detailed derivation is included in Appendix A. The power dissipation by the HE corresponding to the maximum temperature rise was determined by the method of calculation for a vacuumed SJTC with a 5 mA nominal current.

CHAPTER 4: TRANSIENT OVERLOADS

4.1 Introduction

The subject of ETOs, like other electromagnetic compatibility (EMC) issues, has been studied and characterised. ETOs are momentary modifications of the circuit electric conditions resulting when the circuit transitions from one operational state to another or when electromagnetic coupling events occur. In the event of ETO, the voltage and/or current magnitude at the load exceeds the maximum input rating levels:

$$\begin{matrix} V_{load}=V_{max}+V_{transient} \\ I_{load}=I_{max}+I_{transient} \end{matrix} \quad (4.1)$$

The two most commonly known major sources of ETOs in low-voltage AC circuits are lightning strikes, even if the lightning strike was not direct, and the switching mechanism of the circuit [2][3]. Sources of ETOs are not limited to the two mentioned; any event that may change the circuit parameters can be considered a source of ETO. Another interesting source of ETO, which is very annoying, is the ESD from a charged human being, charged cable, or even the equipment itself. ETO events occur in a short time and often have high energy content, enough to cause damage (latent or catastrophic) or hinder the circuit performance.

Since each characterising waveform contains information about the peak value, duration, and energy content of a particular ETO event, the waveforms characterising ETO phenomena are the most important properties to study. Standards defining the testing methods, testing environmental conditions and specifications of the commercial test equipment required to reproduce the standardised test waveforms have been developed over the years. The ETO signal waveform defined and specified, as per standard, is injected from the test equipment into an electronic circuit under test (CUT). The robustness of the CUT is determined by its ability to survive the signal waveform being tested for.

Nowadays, simulation tools have made it possible to model different ETO signal waveforms using equivalent circuit models representing the tester and CUT. However, the test equipment may have different RLC parameter values, depending on the manufacturer's specifications. Nonetheless, waveforms with predefined peak current and voltage values and their respective rise times provide standardisation to compensate for parameter choice by the manufacturer and researchers. The two most important aspects are reproducibility of the standard signal

waveform and the compatibility of the test equipment (i.e. failure levels being independent of the test equipment).

In this chapter, switching and ESD-induced ETOs are discussed. The standards and waveforms characterising each ETO event are further outlined. Lastly, ETOs observed in the AC-DC transfer measurement system at NMISA are characterised.

4.2 Transient Overload Sources

4.2.1 Switching Overvoltage

Switching ETOs are often caused by sudden changes in the circuit operating state due to switching of reactive (capacitive or inductive) loads and current interruptions by relays or circuit breakers [40]. These events are characterised by fast voltage build-up, substantially high energy content and high-frequency damped oscillations until the circuit reaches a new steady state; therefore, any electronic circuit whose design was not compensated for switching ETOs will be exposed to transient overvoltage (also called surge).

4.2.1.1 Switching Transient Overload Standards

Standardised lightning and switching ETO testing waveforms are defined and characterised in the ANSI/IEEE Standard C62.41.2 and IEC 61000-4-5 [2][41] standards. These standards provide a basis for the design and implementation of the effective TOPD(s) in low-voltage AC power circuits. The standardised voltage and current waveforms are produced one at a time by the combination wave generator when open-circuited (voltage measurements) and when short-circuited (current measurements). The open-circuit voltage has a rise time of about 1.2 µs (±30%) and a half value duration of about 50 µs (±20%), whereas the short-circuit current waveform has a rise time of about 8 µs (±20%) and a half value duration of about 20 µs (±20%). The major difference between the ANSI/IEEE Standard C62.41.2 and IEC 61000-4-5 standards is that the ANSI/IEEE Standard C62.41.2 does not define the negative undershoot of short-circuit current (for a positive ETO), which is defined in the IEC 61000-4-5 having a maximum peak of about 30% of the positive peak [41].

4.2.1.2 IEC 61000-4-5 Standard

For a certain test voltage level, the maximum peak current delivered by an IEC 61000-4-5 standard combination wave generator with an impedance of 2 Ω is always half of the applied

test voltage level, e.g., a test voltage level of 0.5 kV will deliver a peak current of 0.25 kA [42]. The equivalent electrical circuit model representing the IEC 61000-4-5 standard combination wave tester is presented in Figure 4.1. The model parameters are tuned to produce the standardised current or voltage waveforms. The HV source is a high-voltage source for the charging network, C_{Store} is the voltage charge storing capacitor of the testing equipment, $L_{Rise-time}$ is the rise time tuning inductor, and R_{CH}, $R_{Matching}$, and R_1 and R_2 are the charging, matching, and impulse shaping resistors, respectively. The discharging network is complete only when the switch is in position 2. R_{Load} is in the order of infinite-ohms for open-circuit voltage measurements and in the order of a few milliohms for short-circuit current measurements.

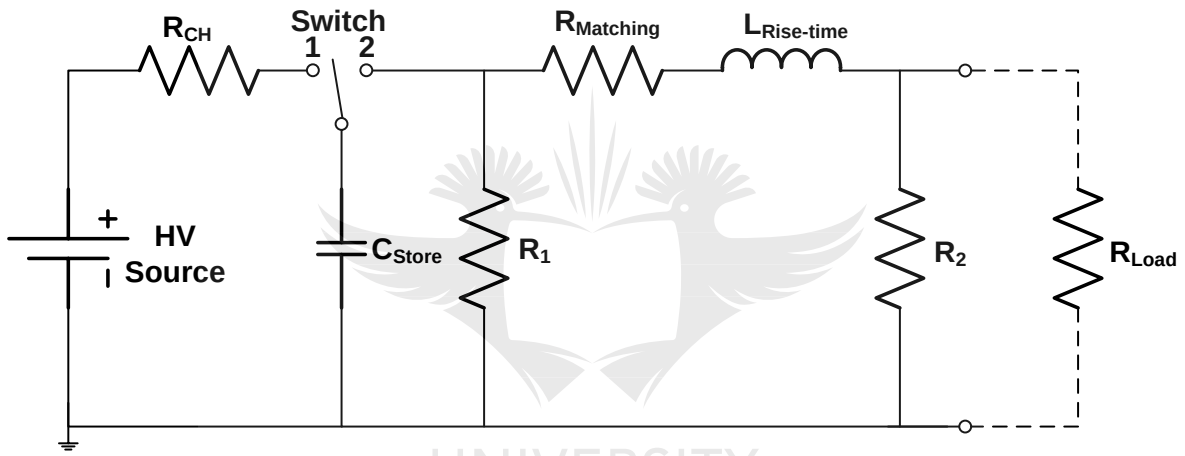

Figure 4.1: Equivalent electrical circuit model of the IEC 61000-4-5 standard combination wave generator

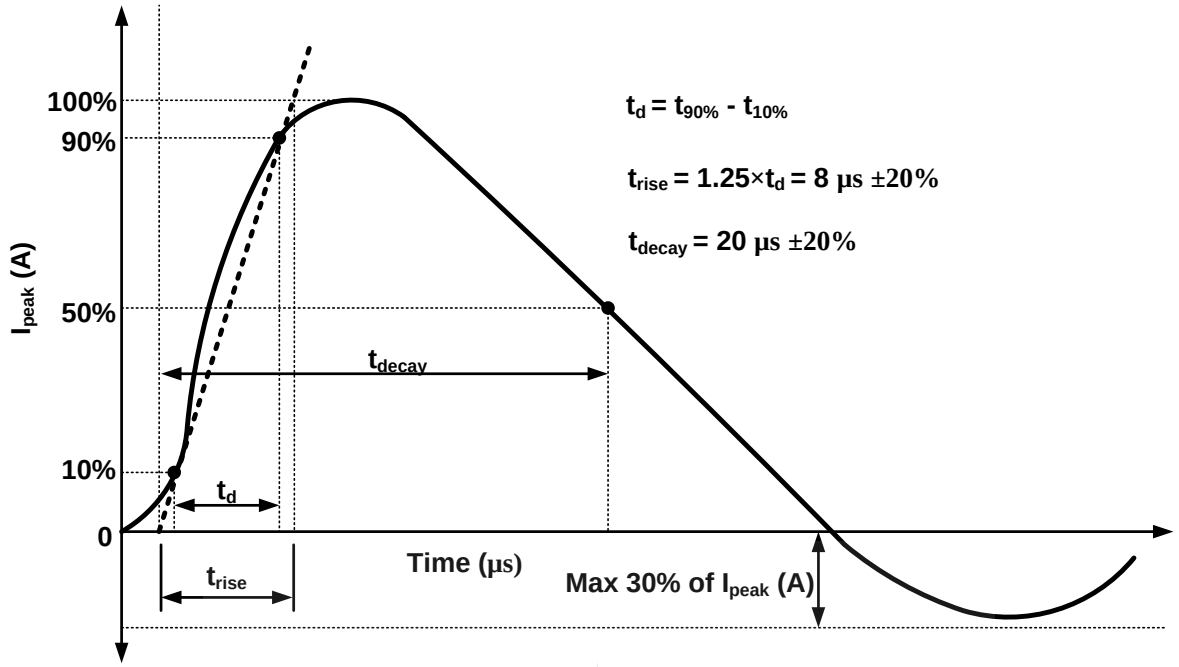

(a)

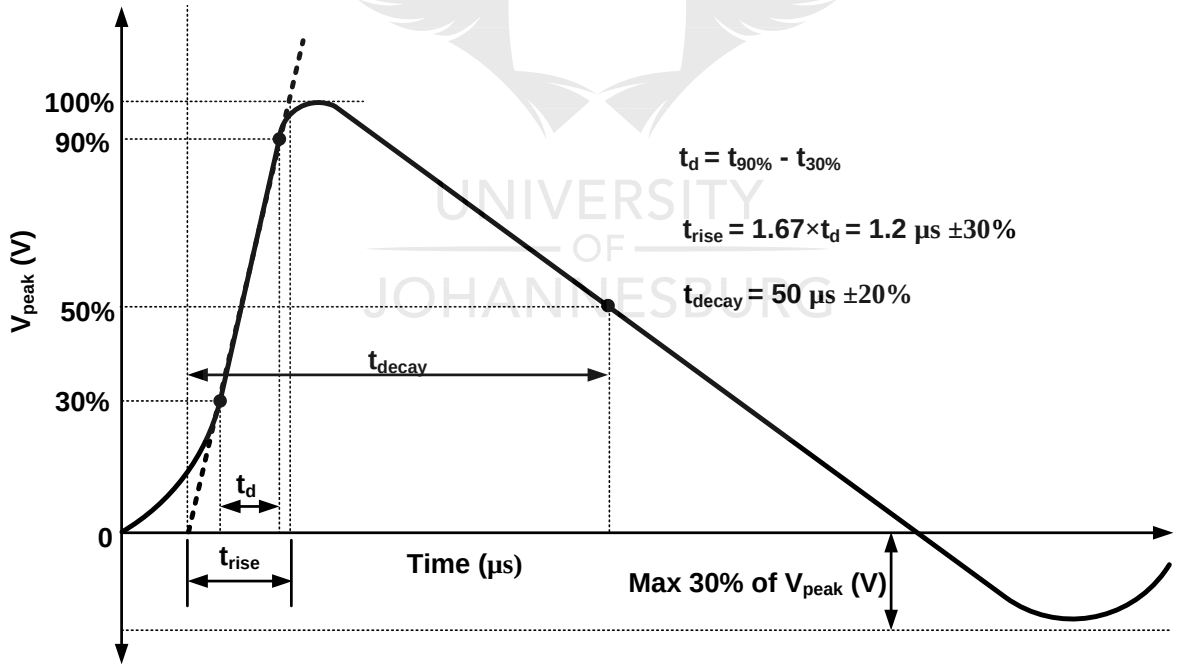

(b)

Figure 4.2: Standard waveforms produced by the IEC 61000-4-5 standard combination wave generator: (a) short-circuit current, and (b) open-circuit voltage

4.2.2 Electrostatic Discharge

ESD is defined in the IEC 61000-4-2 ESD standard as the transfer of static electric charge between objects with different electrostatic potential either in close proximity or direct contact [4]. Almost every person has experienced a shock when touching a doorknob after walking on a non-ESD compensated floor, or when touching the outer surface of a motor vehicle immediately after rising from a cloth vehicle seat, or when discharging through a metal piece after accumulating static charges by either triboelectric charging or electrostatic charge induction. The amount of energy produced by a single discharge event is enough to cause damage or destruction to a component or system (especially semiconductor integrated circuits (ICs)) not protected from ESD. Static charging may take longer, but discharge occurs very fast, approximately in the nano-second time scale. Therefore, ESD can be thought of as a single shot of non-oscillatory high-energy inrush current with a fast rise time and moderately long duration and can be classified as an impulsive ETO [43].

4.2.2.1 Electrostatic Discharge Immunity Standards

ESD immunity test standards have been developed with the mandate to establish electronic circuit immunity by implementing electronic products' reliability test methods, where electronic components or systems are exposed to predefined or standardised ESD current waveforms to test for their survival. These tests are necessarily performed in the production environment and this greatly reduces the number of product returns by customers owing to ESD failure in the end-user environment. Two classes of standards have been developed, the component-level and the system-level test standards [44]. The component-level ESD standards reproduce the ESD current waveforms that may occur in the product manufacturing and assembly environment. The most commonly used of these include:

- Human-body-model (HBM) – which was the first component-level ESD standard developed with the military standard MIL-STD-883. The discharge is from a charged human being into an electronic circuit or component through a fingertip. The MIL standard does not adequately specify the HBM tester; therefore, it is no longer recommended for use. However, the ANSI-ESD and JEDEC-JESD22 standards offer better approximation to the model specifications [45].

- Machine-model (MM) – developed as an extension, “worst-case”, of the HBM by the Japanese car industry. It is now popular in the automotive industry [45]. The discharge is from a charged metallic object or machine into an electronic circuit by direct contact.
- Charged-device-model (CDM) – the component under test accumulates static charges and discharges through its grounding network.

The system-level ESD standards reproduce the ESD current waveforms that may occur in the system manufacturing and assembly environment and extend over to an uncontrolled end-user environment (handling or use of an electronic system). The most commonly used ones include:

- IEC 61000-4-2 – also known as ESD gun, replicates the HBM standard discharges into a system. It accounts for both direct contact discharge and proximity discharge (also known as air discharge).
- Human-metal-model (HMM) – used to qualify a component exposed to the system-level ESD test; therefore, it is the component-level equivalent of the IEC 61000-4-2 standard test. However, the grounding of the HMM tester is not the same as that of the IEC 61000-4-2 standard.
- Cable-discharge-event (CDE) model – most popular in communication cables and systems and occurs when a previously charged cable (usually charged during handling) is connected to an electronic system.

4.2.2.2 Human Body Model vs. IEC 61000-4-2

The HBM and IEC 61000-4-2 standards both reproduce the ESD current waveforms of a charged human being discharging into an electronic CUT. Apart from that, they are at component-level and system-level, respectively. The differences between these standards are observed in the shape of the current waveforms delivered by their respective test equipment, as shown in Figure 4.3. Only one peak is observed in the HBM standard waveform (as seen in Figure 4.3(a)), whereas more current peaks are observed in a single current waveform delivered by the IEC 61000-4-2 standard (Figure 4.3(b)). The HBM standard current waveform has a rise time of about 10 ns and a half value duration of about 150 ns, whereas the current waveform of the IEC 61000-4-2 standard has a rise time of about 0.7 to 1 ns and a half value duration of less than 100 ns [45][46]. Table 4.1 presents a comparison of the current peak values corresponding to certain standard voltage test levels.

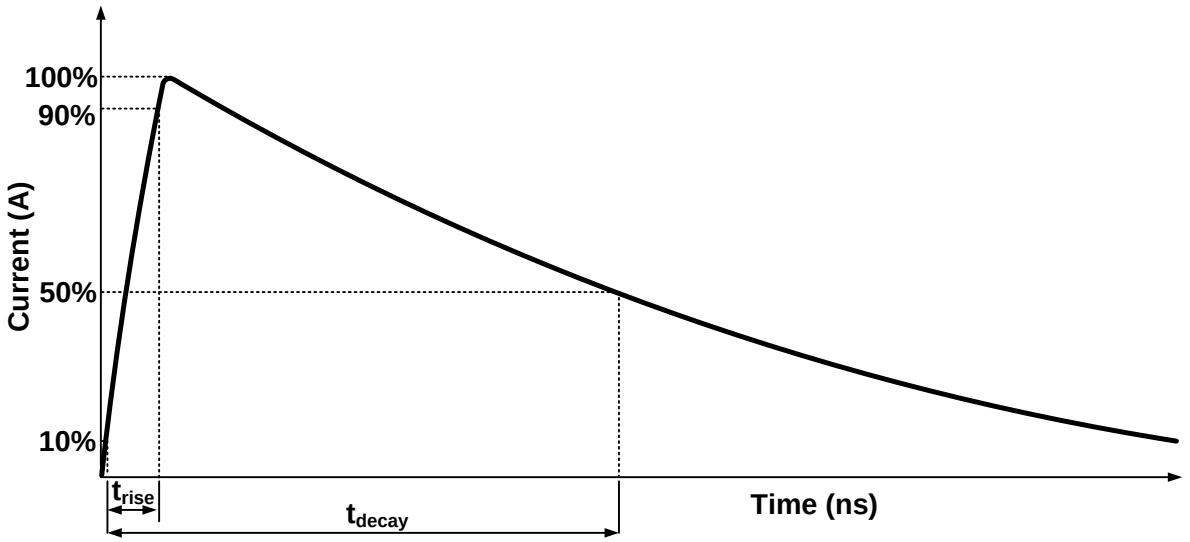

(a)

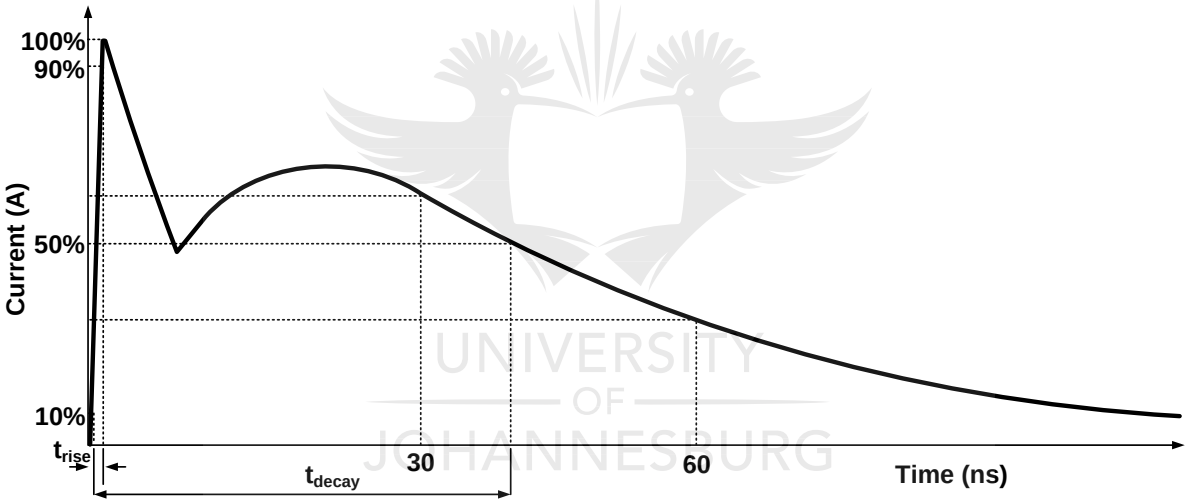

(b)

Figure 4.3: ESD current waveforms: (a) HBM current discharge waveform, and (b) IEC 61000-4-2 ESD current discharge waveform

Table 4.1: Comparisons of the maximum current delivered by HBM and IEC 61000-4-2 ESD standard testers, per voltage test level

Applied Voltage (kV)	Peak Current (A)	
	HBM	IEC 61000-4-2
2	1.33	7.50
4	2.67	15.0
6	4.00	22.5
8	5.33	30.0

Figure 4.4(a) presents a general charging and discharging circuit model used for simulation of ESD current waveforms. To represent the dynamic behaviour of the simulation model of the test equipment, parasitic elements of both the test equipment and electronic CUT are included (Figure 4.4(b) and (c) of the HBM and IEC 61000-4-2 standards, respectively). Prior to discharge, the switch in Figure 4.4(a) is in position *1* and the capacitor C_{ESD} (representing the body of a human being) is charged to a certain voltage level by an HV source through a high-value charging resistor R_{ESD-CH}. This circuit represents a human being charging by either triboelectric charging or electrostatic charge induction methods. At the instance where a discharge is initiated (touching the CUT with a finger-tip), the switch is assumed to be in position *2* and C_{ESD} is discharged into the CUT through a series resistor R_{ESD}, representing the resistance of the human skin. This circuit represents a charged human being discharging into a CUT through a fingertip.

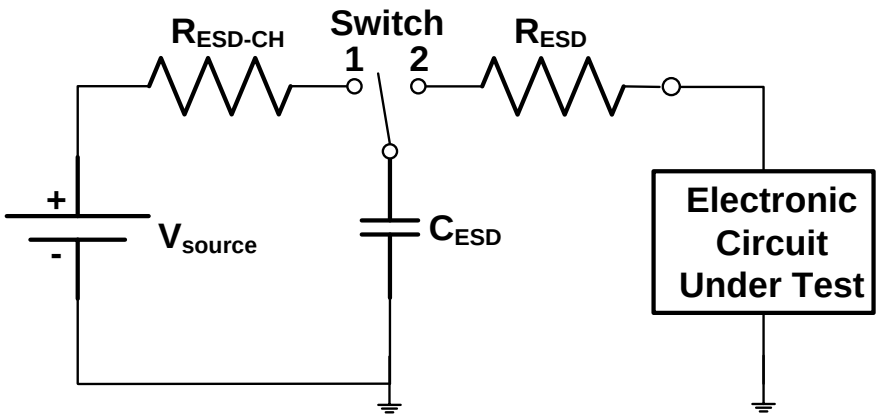

(a)

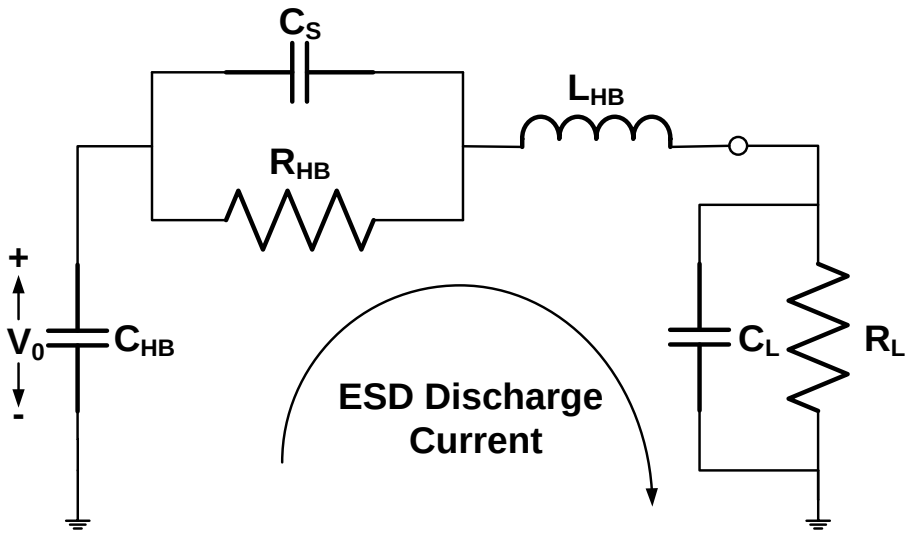

(b)

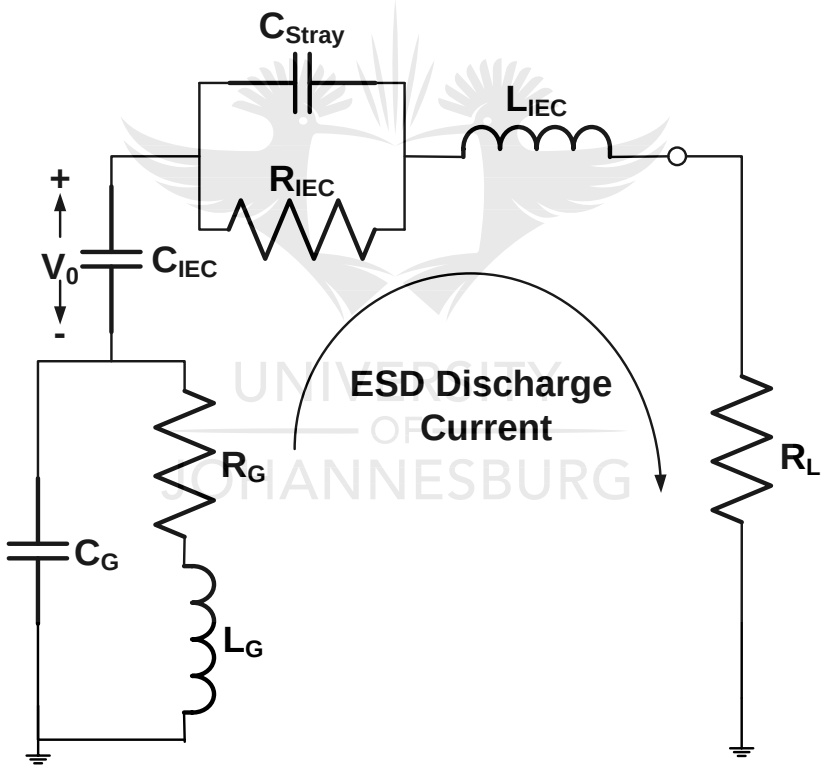

(c)

Figure 4.4: Electrical equivalent circuit models for simulations of the ESD current discharge waveform: (a) general ESD current discharge circuit model, (b) HBM ESD current discharge circuit model [44], (c) IEC 61000-4-2 ESD current discharge circuit model [44]

4.2.2.2.1 Human Body Model

The HBM circuit model shown in Figure 4.4(b) is a fourth-order lumped element model [47], which accounts for the dynamic behaviour introduced by the parasitic components of the test equipment and test board. The analytical solution for the discharge current was difficult to obtain and significant deviations were encountered owing to the complexity of the circuit model. Amerasekera and Verweij reviewed the model and calculated the discharge current of the HBM circuit model neglecting the parasitic capacitances C_S and C_L [47]. The discharge current was calculated as:

$$i_{esd}(t) = V_{esd} C_{HB} \left(\frac{\omega_0^2}{\sqrt{\alpha_{HB}^2 + \omega_0^2}} \right) e^{-\alpha_{HB} t} \sinh\left(t\sqrt{\alpha_{HB}^2 + \omega_0^2} \right) \tag{4.2}$$

with the damping coefficient $\alpha_{HB} = \frac{R_{HB}+R_L}{2L_{HB}}$ and the natural frequency $\omega_o^2 = \frac{1}{L_{HB}C_{HB}}$ given that $\alpha_{HB} > \omega_0$, where C_{HB}, R_{HB} and V_{esd} are the human body parameters (capacitance (F), resistance (Ω), and the initial voltage of the body charge (V), respectively), L_{HB} is the parasitic inductance (H) included to provide the desired rise time, R_L is the load resistance (Ω) and t is the time (s). The solution provided in Eq. (4.2) is still not satisfactory, since it does not account for the influence of the parasitic capacitances [47]. This led to the development of a generalised expression for the HBM fourth-order lumped element model discharge current, which allows analytical fitting to be performed on data obtained experimentally and further extracts parasitic elements of the tester used [47]:

$$i_{esd}(t) = A_1 e^{-\frac{t}{\tau_{esd_1}}} + A_2 e^{-\frac{t}{\tau_{esd_2}}} + A_3 \cos(\omega_{esd} t - \varphi_{esd})\, e^{-\frac{t}{\tau_{esd_3}}} \tag{4.3}$$

where t is the time, A_1, A_2 and A_3 are amplitudes, τ_{esd_1}, τ_{esd_2} and τ_{esd_3} are the time constants, ω_{HB} is the natural frequency, and φ_{esd} is the phase. Maloney [48] also developed an analytical method for the fourth-order lumped element model using the LT technique and extracted parasitic elements of a tester.

4.2.2.2.2 IEC 61000-4-2

Figure 4.4(c) presents an equivalent circuit model of an ESD gun, which is used to simulate the IEC 61000-4-2 ESD standard. The Heildler's function describes the idealised current waveform precisely [4][49]:

$$i_{IEC}(t) = \frac{i_{IEC_1}}{k_1} \frac{\left(\frac{t}{\tau_{IEC_1}}\right)^{n_{IEC}}}{1+\left(\frac{t}{\tau_{IEC_1}}\right)^{n_{IEC}}} e^{\frac{t}{\tau_{IEC_2}}} + \frac{i_{IEC_2}}{k_2} \frac{\left(\frac{t}{\tau_{IEC_3}}\right)^{n_{IEC}}}{1+\left(\frac{t}{\tau_{IEC_3}}\right)^{n_{IEC}}} e^{\frac{t}{\tau_{IEC_4}}} \quad (4.4)$$

where

- t is the time (s),
- $i_{IEC_1} = 16.6$ A and $i_{IEC_2} = 9.3$ A are the currents corresponding to the second IEC61000-4-2 standard test level with a +4 kV ESD,
- $k_1 = e^{-\frac{\tau_{IEC_1}}{\tau_{IEC_2}}\left(\frac{n_{IEC}\tau_{IEC_2}}{\tau_{IEC_1}}\right)^{\frac{1}{n_{IEC}}}}$ and $k_2 = e^{-\frac{\tau_{IEC_3}}{\tau_{IEC_4}}\left(\frac{n_{IEC}\tau_{IEC_4}}{\tau_{IEC_3}}\right)^{\frac{1}{n_{IEC}}}}$ are the correction factors of the amplitude,
- $\tau_{IEC_1} = 1.1$ ns, $\tau_{IEC_2} = 2$ ns, $\tau_{IEC_3} = 12$ ns and $\tau_{IEC_4} = 37$ ns are the time constants, and
- $n_{IEC} = 1.8$.

4.3 Transient Overloads in the AC-DC Transfer Measurement System

ETOs could be coupled into the AC-DC transfer measurement system through several methods. Figure 4.5 presents the possible ETO stress propagation paths in the AC-DC transfer measurement system. Every HI (positive) connector provides a potential path for ESD-induced transient overload stress, whereas the LO (negative) connectors only divert the stress to the ground since they are connected to earth.

- The switching mechanism of the electromagnetic relay used to toggle between the AC and DC input quantities during the measurement process has the potential of generating switching ETO. When the switch is connected to the AC output of the programmable source, the frequency-dependent reactance of the load becomes significant; therefore, the AC source is more likely to produce ETOs than the DC source. The measurement system is also capable of generating ETOs as a result of internal events such as malfunctioning connections, arcs, and so on. The stress can propagate into the load, comprising the REF and UUT connected through a split-type T-adapter, which ensures the symmetry of the signal observed at both units.
- Laboratory personnel, whose body and/or clothes have accumulated electrostatic charges by either triboelectric charging or electrostatic charge induction, could

discharge onto the transfer measurement standard or the transfer measurement system by handling equipment before discharging all the accumulated electrostatic charges. Frequent handling of connecting cables also creates a chance of charging the cable and connecting a component or system to this cable will then initiate a discharge. ESD-induced ETO stresses usually enter the system through the connection points and the stress propagation path depends on the point of discharge; however, it is most likely that the bulk of the stress energy will take the path with low impedance. If the discharge is onto a TS that is isolated from the system, the stress will propagate through the component to its grounding network.

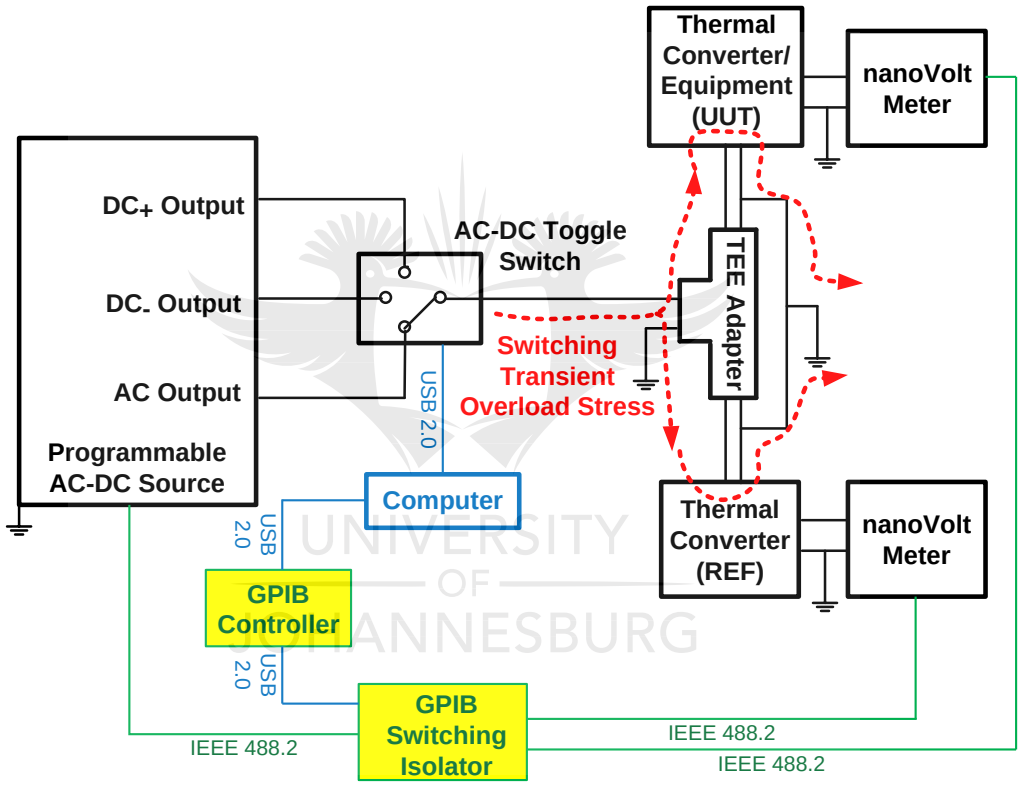

Figure 4.5: Transient overload stress propagation in the automated AC-DC voltage transfer measurement system

4.4 Conclusions

In this chapter, a literature review about ETOs was presented. Switching- and ESD-induced ETOs were also discussed in detail. The standards and waveforms characterising each ETO event were further outlined. Lastly, ETOs and their propagation paths observed in the AC-DC transfer measurement system at NMISA were characterised.

CHAPTER 5: TRANSIENT OVERLOAD PROTECTION DEVICES

5.1 Introduction

ETOs have been studied and characterised for many decades, therefore the design engineers are familiar with this class of EMC and often compensate for them in their designs. Most electronic devices, including electrical systems and appliances used in households, have internal TOPDs or circuits embedded; however, in some cases, these protection measures do not offer enough protection. In such cases, the addition of external protection measures at the input circuitry of the device being protected is essential. Various devices and techniques are readily available as protection solutions. The *p-n* junction semiconductor properties of TVSs make them the most advanced and suitable devices for this application [5].

The clamp-type TOPDs used in this work are well suited for the application of this study, since they have a faster response time and better energy-handling capability than their alternatives. Protection against ESD-induced ETOs can be achieved by controlling the working environment or implementing antistatic workstations; however, in cases where ESD can be avoided by using a ground strap or by discharging before handling the electronic equipment [50], human beings tend to forget. Therefore, it is desirable to implement additional protection measures using TVS(s). The standard 1.2/50 µs open-circuit voltage, 8/20 µs short-circuit current, 10/1000 µs long exposure, and the HBM/IEC 61000-4-2 testing waveforms, characterised in Chapter 4, are the most commonly used standards for the determination of TOPDs' robustness against ETOs.

This chapter starts by describing the properties of *p-n* junction semiconductor TVSs and their application as TOPDs. The physical and electrical properties of the TVS diode, Zener diode, and the MOV are then presented. Lastly, protection techniques using TVSs are discussed.

5.2 *P-N* Junction

Semiconductor devices are characterised by at least one junction between their p-type and n-type materials, called the *p-n* junction, which is fabricated using several semiconductor fabrication technologies such as photolithography, ion implantation and other thermal methods [5]. Figure 5.1 presents the electrical characteristics of a single *p-n* junction semiconductor device under both forward and reverse bias operation. Under reverse bias, the width of the *p-n* junction widens, which means that the potential barrier also increases. An electromotive force

needs to be applied to create an electric field sufficient to break the potential barrier and initiate charge tunnelling in the depletion region of the *p-n* junction. However, a small amount of charge transfer is observed because of the temperature dependencies of the charge generation in the junction. Therefore, under reverse bias, the junction presents high impedance (high potential barrier), which results in an almost constant small current conduction, called saturation or leakage current, until a certain breakdown voltage is reached. Once the breakdown voltage is reached (potential barrier crossed), the junction presents low impedance, which results in a dramatic current increase with an almost constant voltage, called the clamping voltage. Therefore, these electrical characteristics of the *p-n* junction make it suitable for application as TOPD. The total current flowing through the *p-n* junction is expressed as [51]:

$$I = I_{leak}\left(e^{\frac{V_{app}}{n_m V_{th}}} - 1\right) \tag{5.1}$$

where I_{leak} is the reverse leakage current, V_{app} is the biasing voltage applied to the junction, V_{th} is the thermal voltage corresponding to 26 mV at room temperature, and n_m is the material constant.

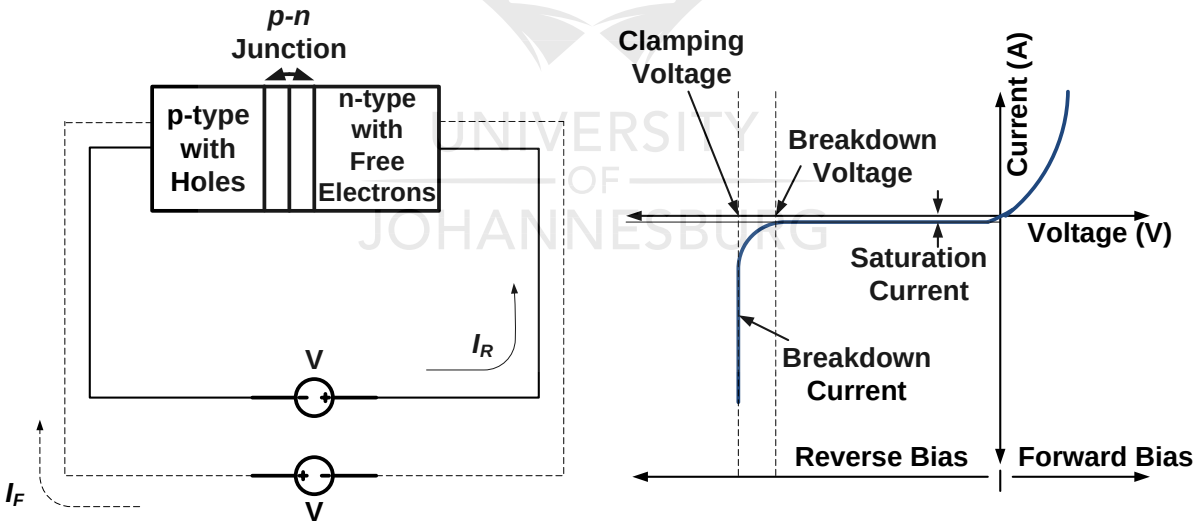

Figure 5.1: Electrical characteristic curve of a biased *p-n* junction semiconductor

The conduction point of a *p-n* junction under bias is determined by either the Zener effect or avalanche multiplication [52]. The former is observed in heavily doped *p-n* junctions where only a small amount of biasing voltage is required to generate an electric field to cause tunnelling, since the junction width is narrow, whereas the latter is observed on lightly doped *p-n* junctions owing to charge multiplication caused by collision ionisation.

5.3 Transient Voltage Suppressor Devices

Clamp-type TVSs are a class of TOPDs with nonlinear impedance characteristics [53]. At a voltage level below the maximum permissible input, the TVS is found to be in a high-impedance mode and it is ideally not conducting. However, since the TVS is not ideal, a small amount of current (called the leakage current, corresponding to a certain leakage voltage) is conducted through the TVS. At a voltage level above the maximum permissible input of the protected circuit, the TVS is found to be in low-impedance mode and starts to conduct. The voltage at which a TVS starts to conduct is called the breakdown voltage. A high-current build-up through the TVS is observed and only a small amount, equal to the maximum permissible input of the protected load, is conducted to the load. The voltage across the TVS, called the clamping voltage, stays relatively constant and applies to the load. Figure 5.2 presents a simplified protection mechanism of a clamp-type TVS device. Most of the ETO current is diverted away from the protected load to the ground through the TVS and the voltage is clamped to a safer level.

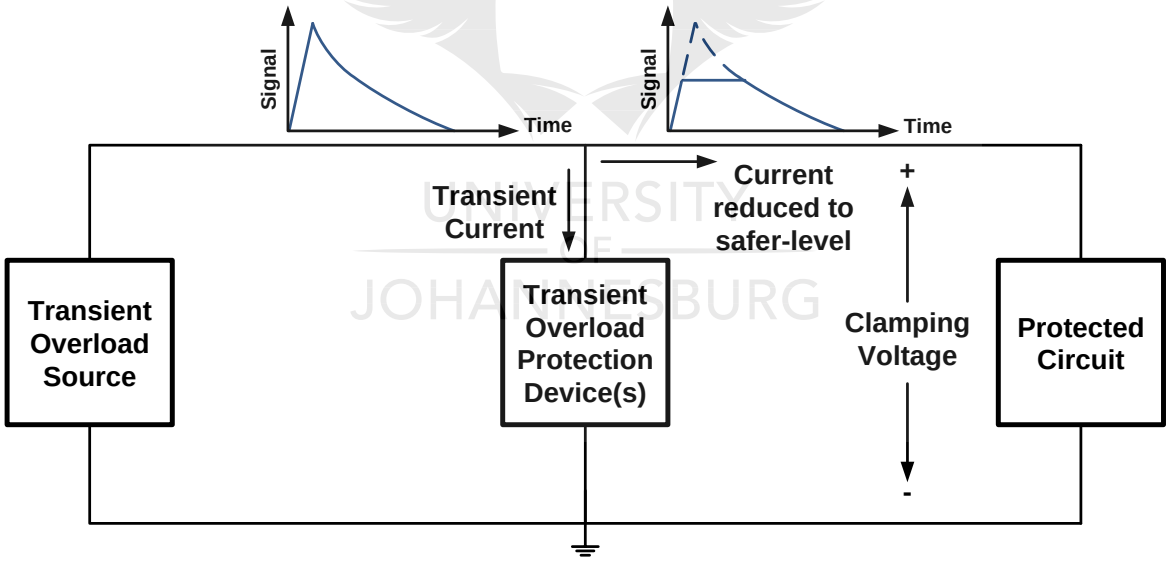

Figure 5.2: Simplified schematic diagram of a transient voltage suppression protection measure

The most commonly used TVS devices, because of their superior response, are the clamp-type TVSs such as the TVS diode, Zener diode, and the MOV.

5.3.1 Transient Voltage Suppressor Diode

A TVS diode is a solid-state single *p-n* junction voltage clamping device used to protect electronic circuits from ETOs, especially ESD-induced ETOs [54]. The TVS diode is characterised by lightly doped *p-n* materials and a wide *p-n* junction, which allows it to conduct more transient current and absorb more transient energy, better than the Zener diode, but not better than the MOV. However, the width of the junction presents a limitation in the conduction mechanism: the avalanche multiplication effect is observed at a higher clamping voltage that results in slower response time compared to the Zener diode. The TVS diode is manufactured as either unidirectional or bidirectional (for protection against ETOs of both polarities) and also as axial leaded or surface-mount packages [55].

Figure 5.3 presents the electrical current-voltage (I-V) characteristics of a unidirectional TVS diode. The diode offers the desirable voltage-clamping characteristics when operated in reverse bias mode and its I-V characteristics are similar to those of a Zener diode [56]. Figure 5.4 presents the equivalent circuit model representing the unidirectional TVS diode in all regions of operation. Three regions of operation are observed and accounted for in the reverse bias TVS diode macro-model:

1) Leakage-current region, which occurs before the diode breakdown or the conducting voltage point is reached. This region is characterised by small leakage current I_L (shown in Figure 5.4), which could be attributed to the temperature dependence of the *p-n* junction, and modelled by a series combination of the diode inductance L_{TVS} and a high-value resistor R_L.
2) Breakdown region, which is observed after the breakdown voltage is reached. This region is characterised by a drastic breakdown current increase through the TVS diode *p-n* junction and a nearly constant voltage which is called the clamping voltage and expressed as [57]:

$$V_C = V_{BR} + V_{D_{BR}} + I_{PP}R_Z + L_{TVS}\frac{dI_{PP}}{dt} \tag{5.2}$$

where V_{BR} is the breakdown voltage (V), $V_{D_{BR}}$ is the voltage of the breakdown avalanche diode (D_{BR}, typically 0.7 V), I_{PP} is the maximum reverse peak pulse current (A), R_Z is the low-value dynamic resistance (Ω) of the diode breakdown and L_{TVS} is the inductance (H) of the diode. Figure 5.4 presents the modelling network of the TVS diode in this region.

I_{BR} is the current through the TVS diode when conducting in the reverse-bias breakdown region.

3) The high-current region, which occurs when the maximum permissible ratings of the diode are exceeded. In this region, the diode is most likely to be destroyed and becomes a conducting wire (short circuit fail mode).

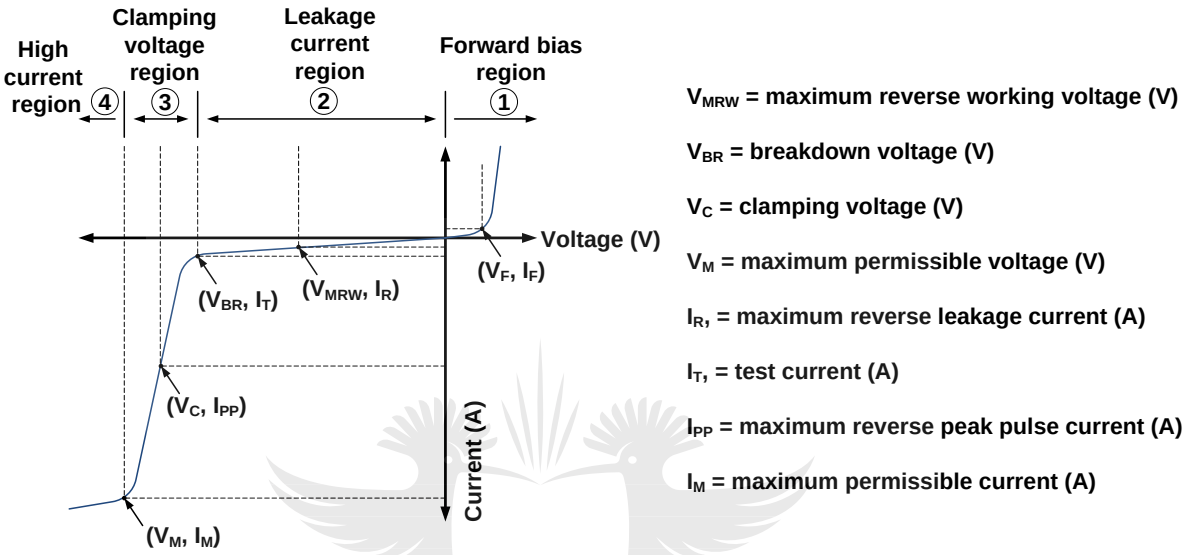

Figure 5.3: I-V characteristics of the TVS diode

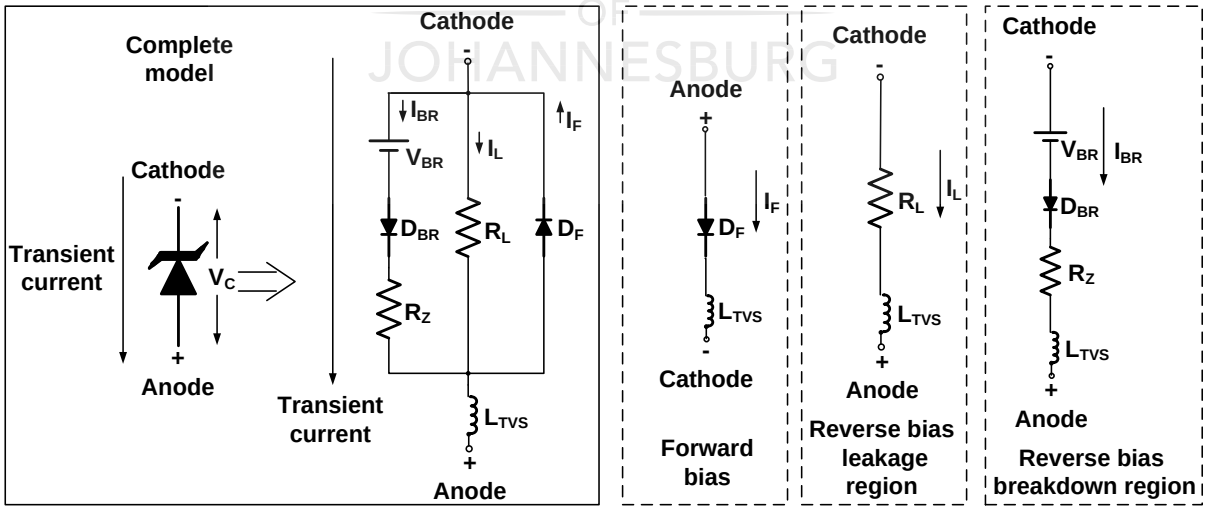

Figure 5.4: Equivalent electrical macro-model of a unidirectional TVS diode

5.3.2 Zener Diode

A Zener diode is a solid-state single *p-n* junction device initially developed for voltage regulation [58]; however, because of its ability to clamp transient voltages when operated in reverse-bias mode, it is rather used as a TOPD in many applications where ETO protection is required. The *p-n* materials of the Zener diode are heavily doped; thus, the width of the junction is narrow, which allows charges to tunnel easily between the *p-n* junction sides. This means that the Zener diode turns on much faster and therefore has a lower clamping voltage compared to the TVS diode and the MOV. However, one limitation associated with its performance is that the narrow *p-n* junction can only allow a small amount of transient current through before it overheats. This makes its energy absorption capability lower compared to the TVS diode and the MOV. The I-V characteristics of a Zener diode are presented in Figure 5.5. Three regions of operation are observed in the reverse bias mode as presented by the macro-model (shown in Figure 5.6):

1) Leakage-current region, before the breakdown voltage. This region is modelled by a high-value resistor R_L, where I_L is the leakage current (A).
2) Breakdown-region, characterised by a rapid current increase and a nearly constant voltage called the clamping voltage V_C, which can be expressed as

$$V_C = V_Z + V_{D_{BR}} + I_{ZD}R_d \tag{5.3}$$

where V_Z is the Zener voltage (V) (measured at test current I_{ZD} (A)), V_D is the forward voltage of an avalanche diode (typically 0.7 V) and R_d is the dynamic resistance (Ω) of the Zener diode. The modelling network is presented in Figure 5.6, where I_{BR} is the breakdown current.

3) The high-current region, which is modelled by the R_M and I_M network of the Zener diode macro-model in Figure 5.6. Similar to the TVS diode, in this region, the diode is most likely to be destroyed and to become a conducting wire (short-circuit fail mode).

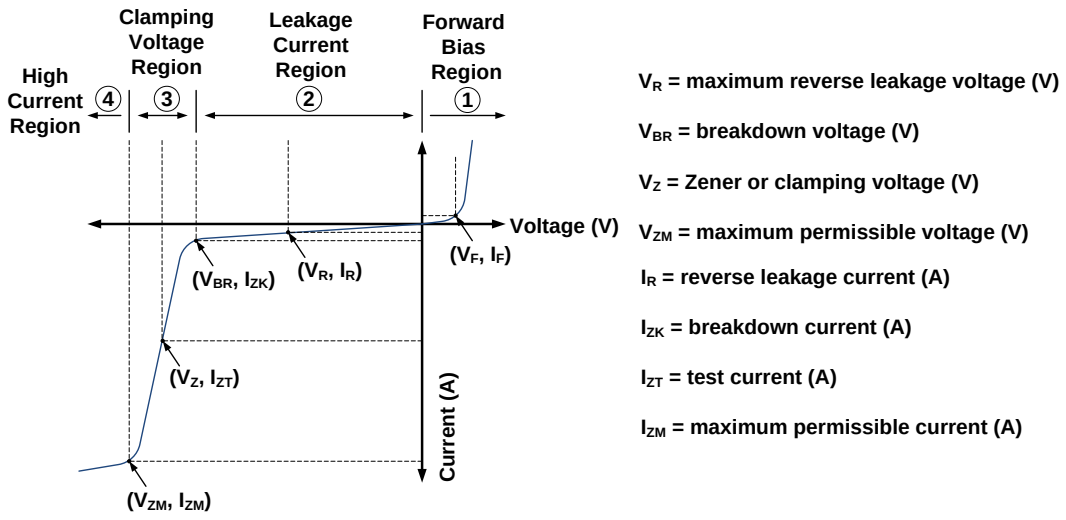

Figure 5.5: I-V characteristics of a Zener diode

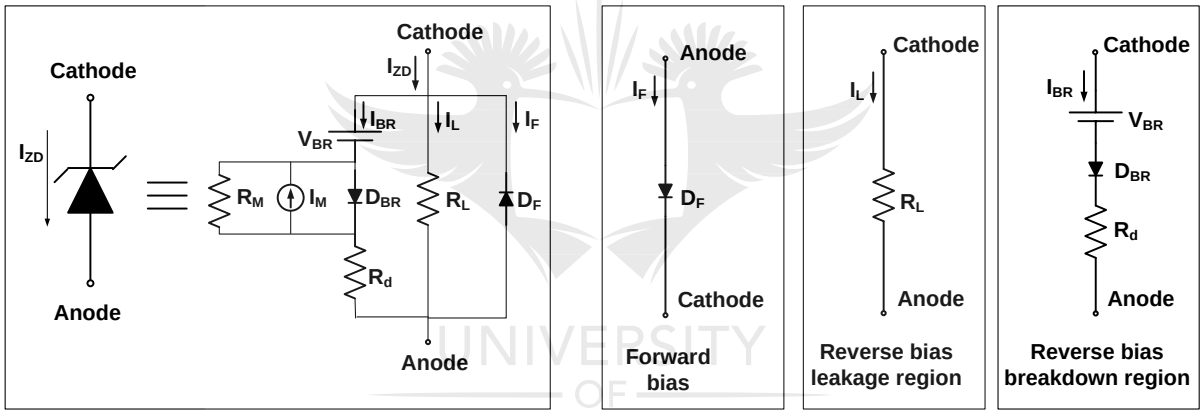

Figure 5.6: Zener diode SPICE macro-model

5.3.3 Metal-oxide Varistor

A MOV, also referred as to Zinc-oxide varistor or voltage-controlled resistor, is a multi *p-n* junction TOPD with nonlinear voltage-current (V-I) characteristics, similar to a back-to-back Zener diode [55]. It has a high energy absorption capability, attributed to multiple *p-n* junctions distributed throughout the device, compared to the TVS diode and the Zener diode. However, one limitation attributed to its performance is that high bias voltages must be applied to break the potential barriers in each of the *p-n* junctions before the device can fully conduct transient current. This results in a higher clamping voltage, and thus a slower response. Furthermore, the device has higher thermally generated leakage currents [59], and this is also attributed to multiple junctions.

The device is also defined for three regions of operation, as shown in the voltage-current (V-I) characteristics of MOV in Figure 5.7(a). The equivalent electrical model of the operation of the MOV is presented in Figure 5.7(b), with the complete circuit model, and the simplified circuit model for each region of operation [60]. The model parameters are as follows: L_{MOV} is the inductance of the varistor leads, C_{MOV} is the capacitance between the two terminals of the varistor, R_{OFF} is a high resistance used to model the MOV in the leakage current region, R_{MOV} is the nonlinear MOV resistance used to model the MOV in the normal operating region and R_{ON} is a low bulk resistance used to model the MOV in a high-current or upturn region.

1) The leakage-current region, which is characterised by high impedance and small temperature-dependent leakage current, is observed when the MOV is supposedly in the nonconducting state.
2) The normal MOV operation region, which is characterised by a nonlinear resistance R_{MOV}, is defined by the power law:

$$I_{MOV} = k \times V_{MOV}^{\alpha_{MOV}} \tag{5.4}$$

where I_{MOV} is the current through the device, k is the device constant, V_{MOV} is the voltage across the device (V) and $\alpha_{MOV} = \frac{\log\left(\frac{I_2}{I_1}\right)}{\log\left(\frac{V_2}{V_1}\right)}$ is the nonlinearity degree of conduction.

This nonlinear resistance is also defined using the interpolation formula, which accounts for the transition regions [61]:

$$\log(V_{MOV}) = B_1 + B_2 \log(I_{MOV}) + B_3 e^{-\log(I_{MOV})} + B_4 e^{\log(I_{MOV})} \tag{5.5}$$

where I_{MOV} is the current (A) through the device, V_{MOV} is the voltage (V) across the device and the interpolation parameters B_1 through B_4 are specified by the manufacturer for each MOV type.

3) The upturn or high-current region occurs when the MOV ratings are exceeded, thus, the device is most likely a conducting wire.

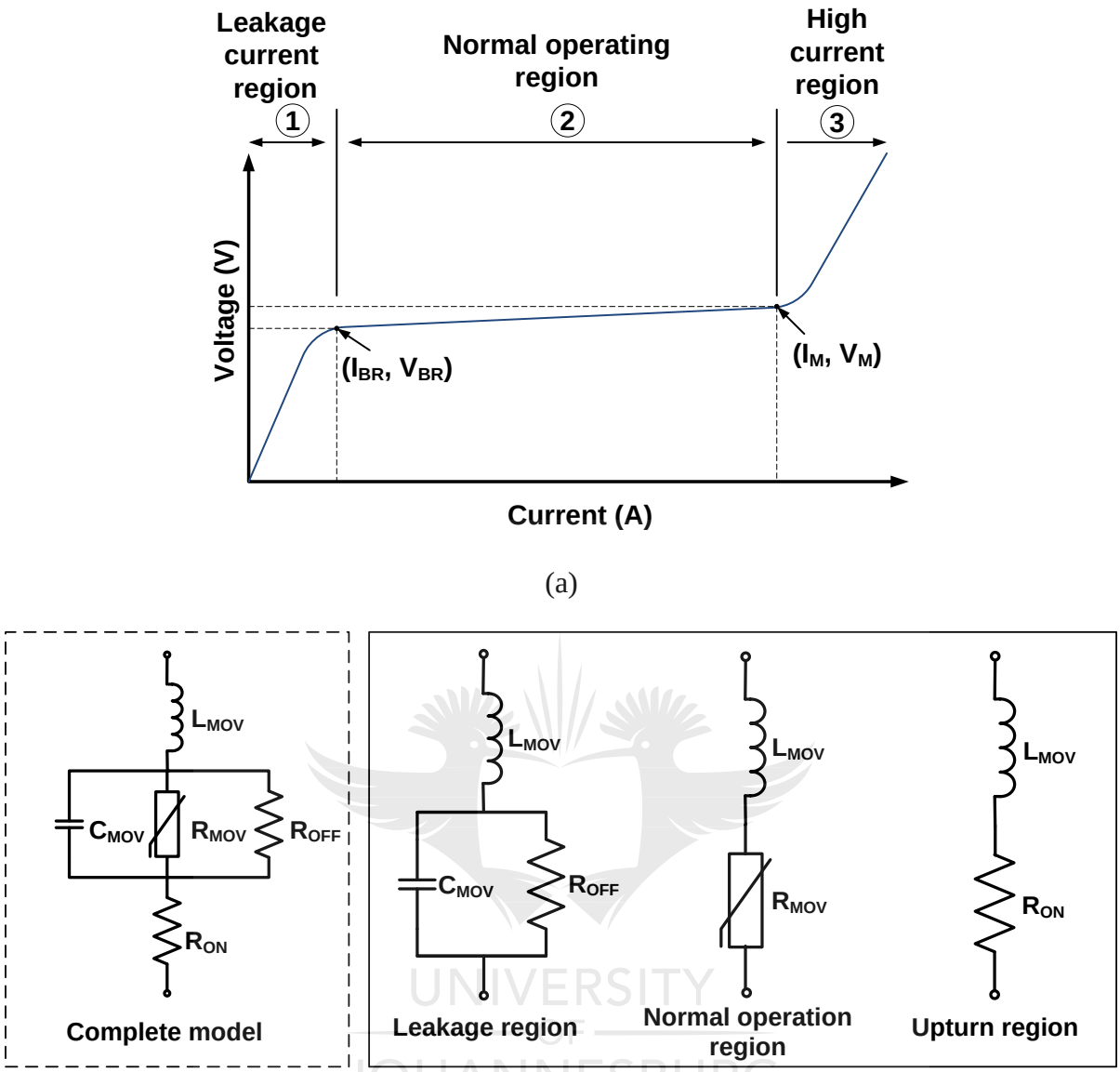

Figure 5.7: (a) V-I characteristics of MOV (must be on a log-log scale), (b) Equivalent electrical circuit model of MOV

5.4 Protection Strategies

The one limitation presented by all the TVSs is that when used individually, either a fast response or high energy absorption is achieved, but not both. However, a combination of these devices to achieve both functions is attractive [56][62]. Implementation of multi-stage TOPM, as shown in Figure 5.8, could offer effective protection against ETOs [1][63][64]. A MOV is implemented in the first stage, because of its high energy absorption capability, then followed by back-to-back Zener diodes, since these have a faster response time. A bidirectional TVS

diode with an array of steering diodes is implemented in the last stage of the TOPM to help the Zener diodes with the absorption of the transient energy before the MOV turns on. This technique, compared to individual implementation, theoretically meets the requirements for an effective ETO protection design. The transient energy is distributed across the TOPDs with the first stage TOPD absorbing most of the transient energy. This transient energy distribution ensures that the protection devices also protect one another against overheating as a result of large and long transient current exposure.

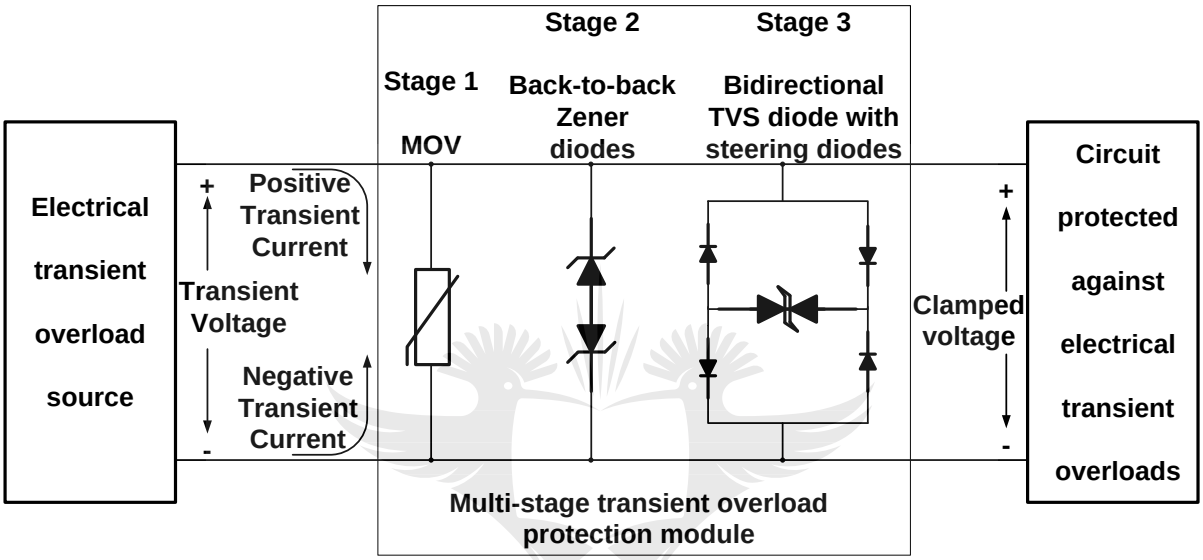

Figure 5.8: Typical multi-stage transient overload protection module

In reality, a device with a fast response and low energy absorption capacity tends to turn on and be exposed to higher energy for a duration long enough to drive it to overheating before a device with a slow response and higher energy absorption capability turns on; therefore, selection of the TOPD must be done thoroughly and additional current limiting devices such as a fuse or resistor may be added in series with the TOPD. Furthermore, this technique tends to have an impact on the signal attenuation if the protection is applied in communication lines [63]. However, Casey suggested that this effect is caused by the voltage dependence of the protection device capacitance and proposed a method of applying a bias voltage to the protection device to make the capacitance of the protection device less dependent on the applied voltage [65].

5.5 Conclusions

In this chapter, the properties of the *p*-*n* junction semiconductor TVSs and their application as TOPD were presented. The impedance characteristics and electrical properties of the TVS diode, Zener diode, and the MOV were then discussed. Lastly, protection techniques using TVSs and possible advantages and limitations of implementing these protection techniques were discussed.

CHAPTER 6: RESEARCH METHOD

6.1 Introduction

Mathematical and simulation analysis and experimental analysis were carried out to determine the response of a 5 mA nominal current rated UHF-pattern SJTC to switching- and ESD-induced ETOs (in accordance with the IEC 61000-4-5 and IEC 61000-4-2 standards, respectively). Analyses were carried in the presence and absence of a protection device implemented between the source of ETOs and the SJTCs.

This chapter presents the method used for the analysis of the response of the SJTC to ETOs when the protection measures are not implemented and when they are implemented.

6.2 Mathematical and Simulation Modelling Method

A sine wave source with 500 kHz frequency was used to supply the SJTC HE with the specified operating signal through a $R_L = 1\ \Omega$ wire. The ETO sources (IEC 61000-4-5 switching and IEC 61000-4-2 ESD) were coupled onto the line to apply a transient signal to the HE input. The response of the UHF-pattern SJTC was determined for two cases:

Case 1: No TOPD was implemented across the input circuit of the SJTC, as presented in Figure 6.1.

Case 2: This was similar to *Case 1*, but with the TOPD(s) implemented as a shunt across the SJTC input circuit, as shown in Figure 6.2. In this case, each of the TOPDs was implemented individually to determine its performance and the effect of implementing an individual protection measure, and after that different TOPDs were integrated into a multi-stage circuit to determine its performance and the effect of implementing a hybrid protection measure.

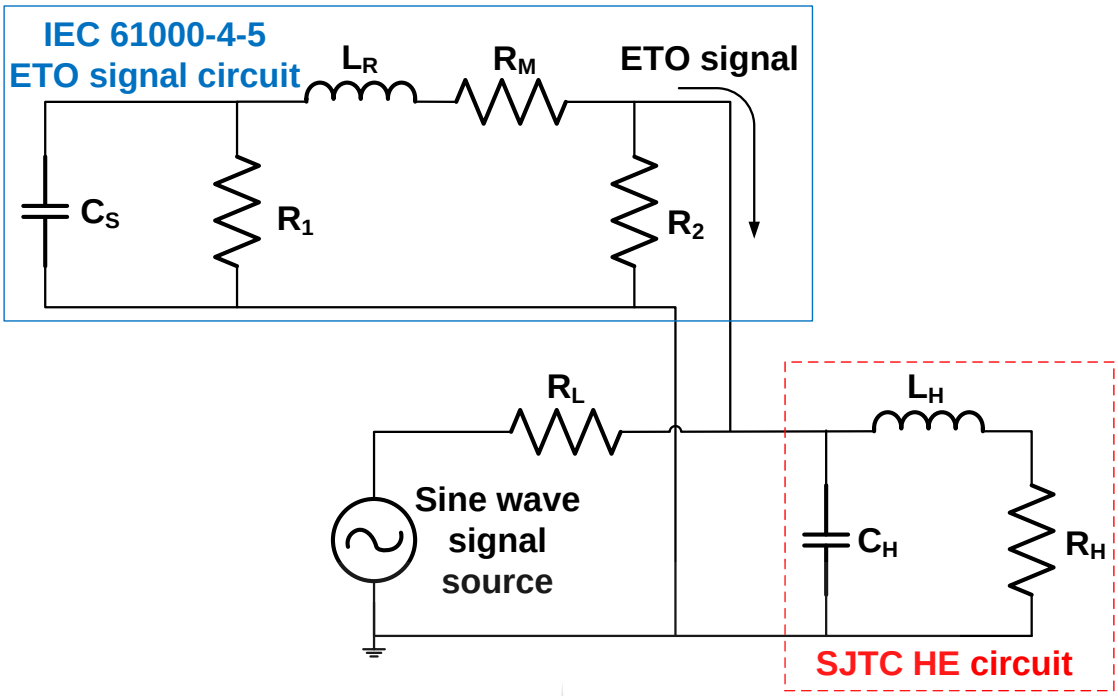

(a)

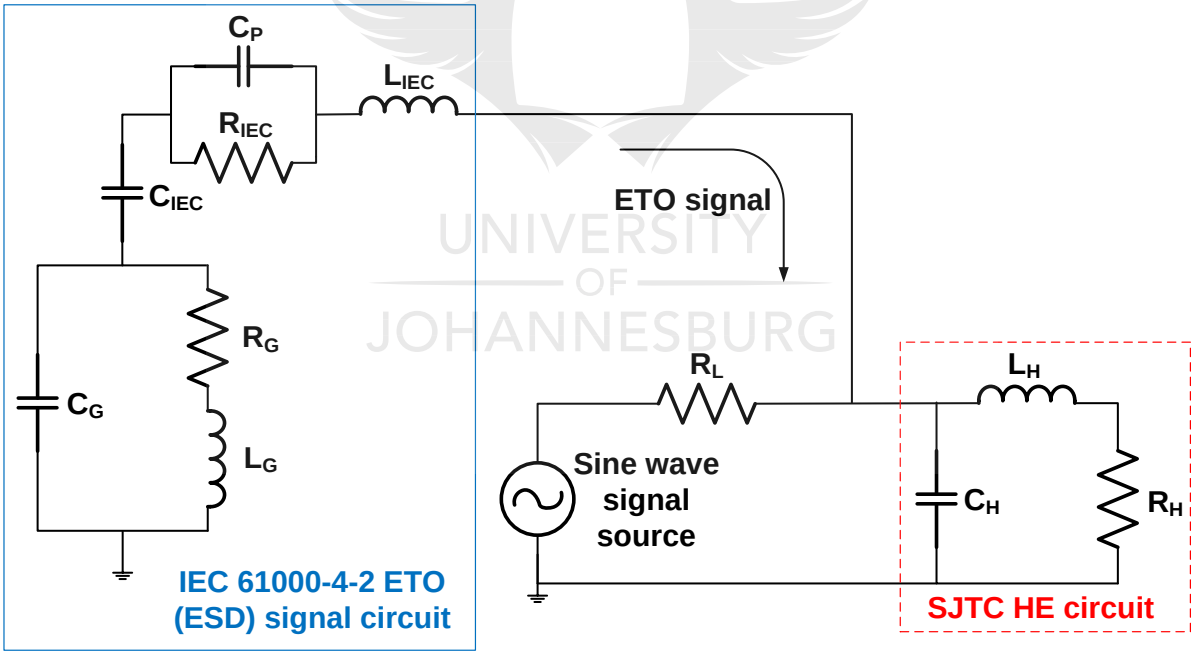

(b)

Figure 6.1: *Case 1* model configuration: (a) IEC 61000-4-5 standard ETO coupled into a line, and (b) IEC 61000-4-2 ESD standard ETO coupled into a line

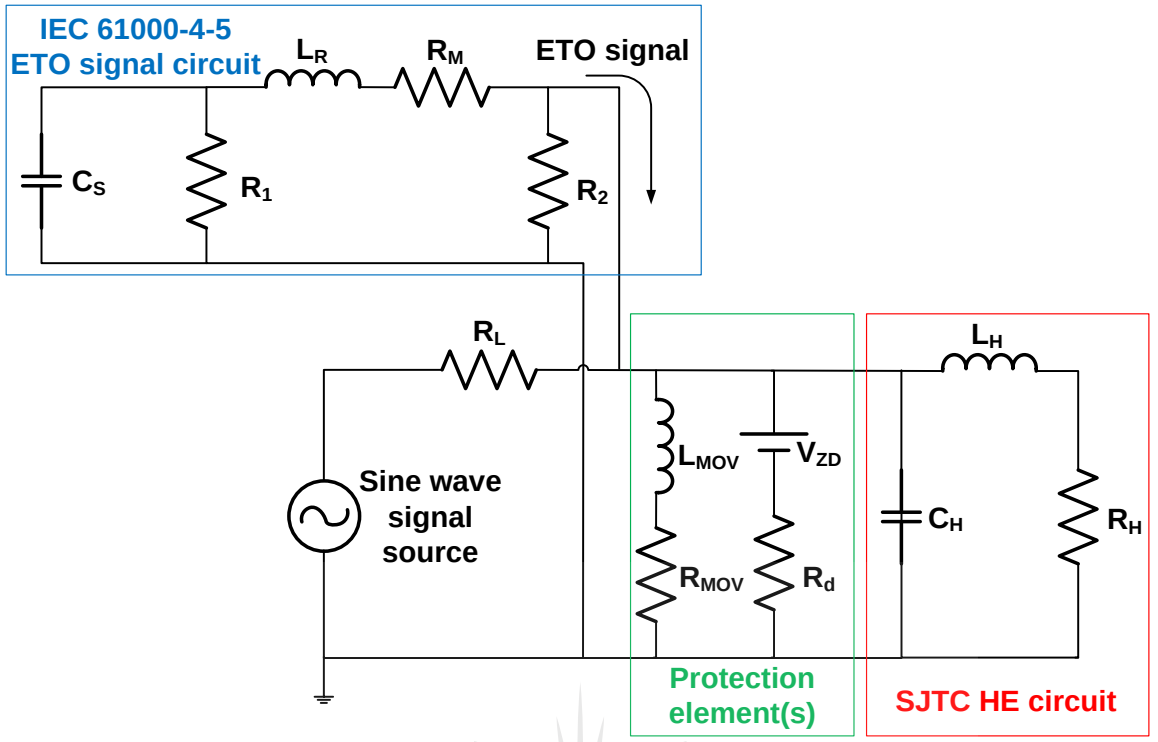

(a)

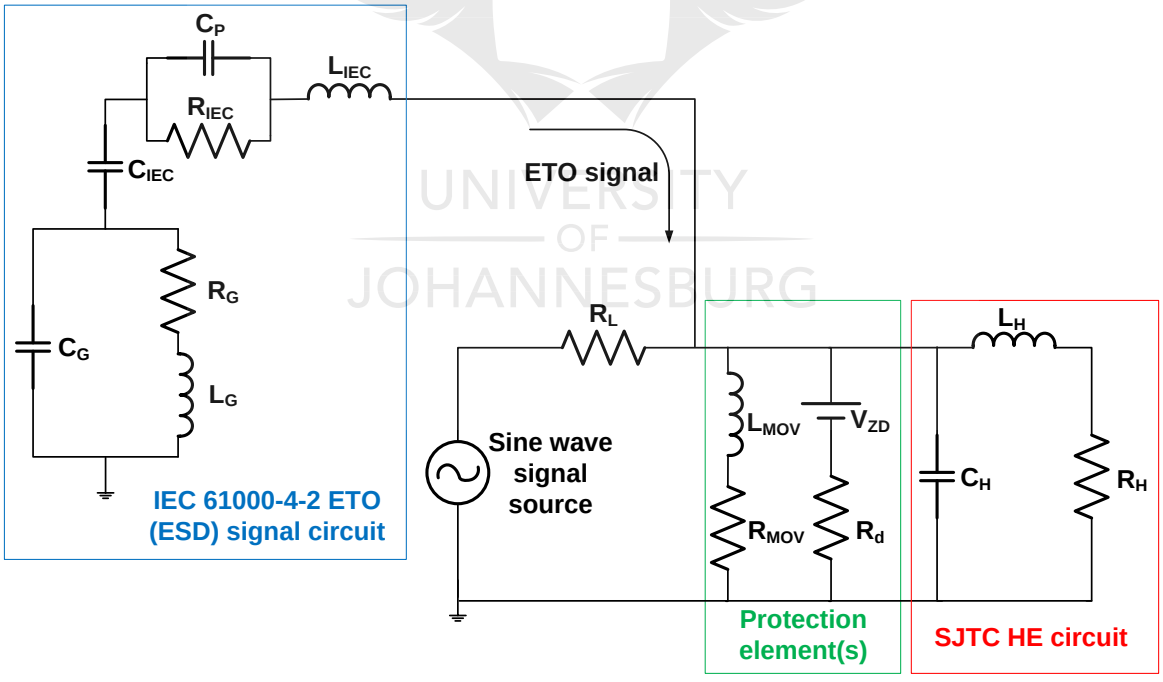

(b)

Figure 6.2: *Case 2* model configuration: (a) IEC 61000-4-5 standard ETO coupled into a line with protection, and (b) IEC 61000-4-2 ESD standard ETO coupled into a line with protection

6.2.1 Modelling Networks

6.2.1.1 Switching- and ESD-induced Transient Overload Modelling Networks

The signal waveforms produced by simulating equivalent circuit models of the IEC 61000-4-5 and IEC 61000-4-2 standards were validated using the mathematical models. Since the model parameters are dependent on the manufacturer's specifications of the ETO test equipment, the parameters of the equivalent circuit models of the switching ETOs and ESD from a charged member of the laboratory personnel were tuned to reproduce the waveforms that meet the requirements specified by their respective standards. In both models, prior to the discharge (at the instance $t < 0$ s), the respective energy-storing capacitors were assumed to have been charged to the desired test voltage levels and were discharged on to the tested circuit models at the instant when $t = 0$ s.

The standard modelling networks were also described using the LT technique by converting them into a complex frequency ($s = j\omega$) domain, and then converting the solutions for current and voltage into the time domain using the inverse Laplace transform (ILT) technique. The modelling networks were also implemented in Cadence Capture and simulated in Cadence PSpice to verify the solutions implemented using LT mathematical analysis.

6.2.1.1.1 IEC 61000-4-5 Standard Model

The equivalent electrical circuit model of the IEC 61000-4-5 standard given in Figure 6.3(a) was simplified to ease the mathematical analysis. Figure 6.3(b) presents its transformed network, which was used for mathematical analysis. The model parameters are presented in Table 6.1. The initial conditions for the current through the inductor and the voltage across capacitors are: $i_{L_R}(0) = 0$ and $v_{C_S}(0) = V_i = 530$ V.

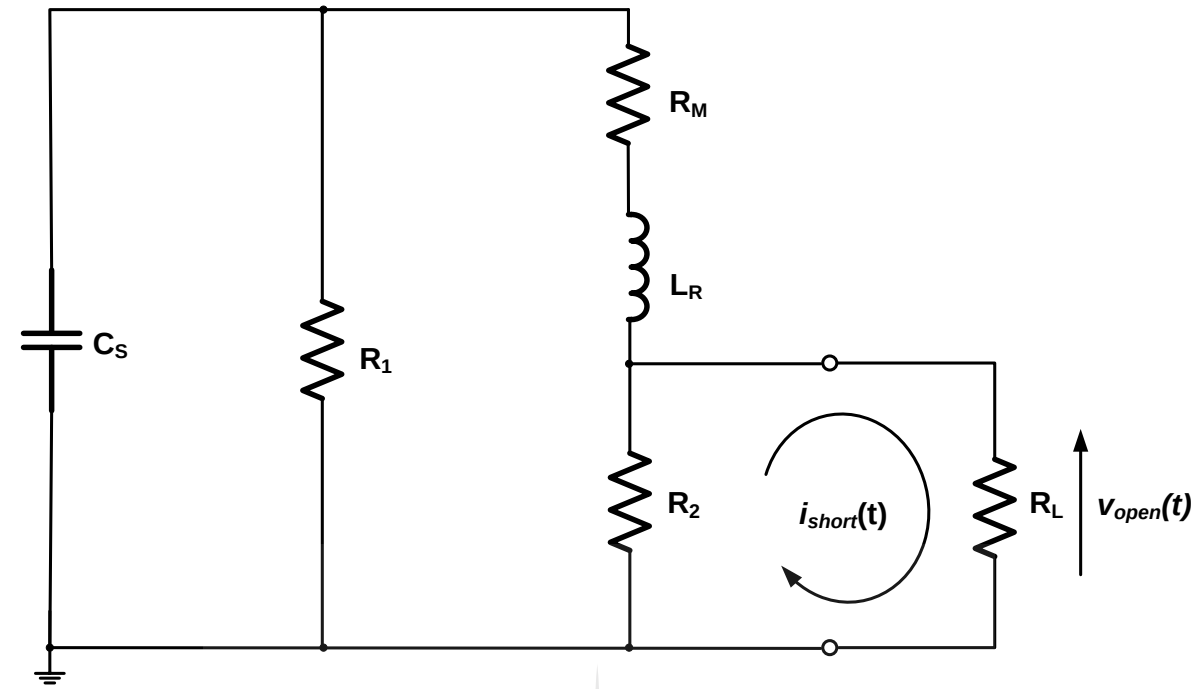

(a)

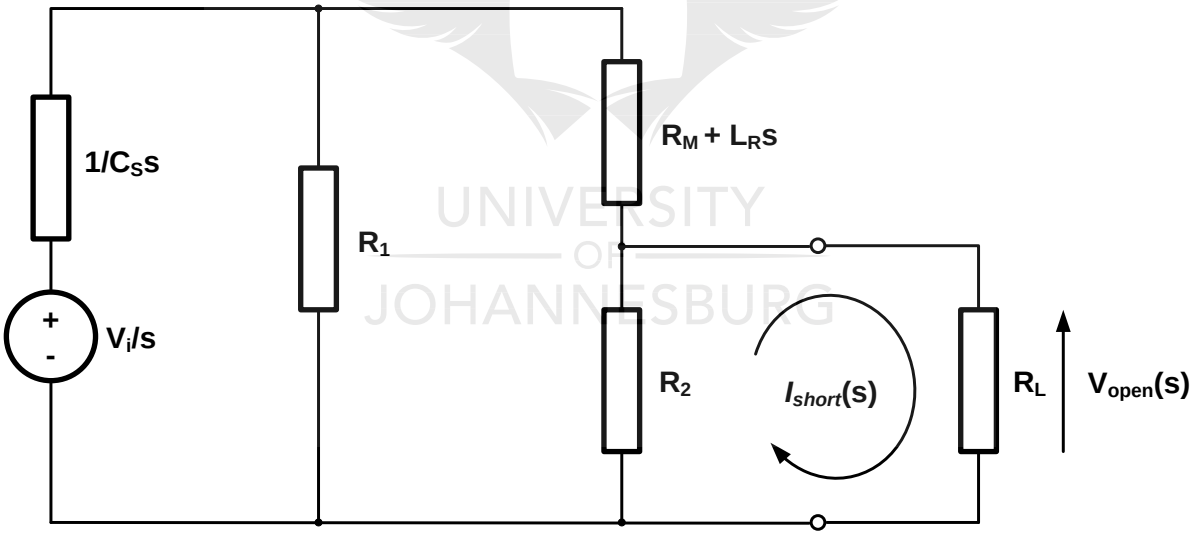

(b)

Figure 6.3: IEC 61000-4-5 standard modelling network: (a) standard circuit model, and (b) Laplace transformed circuit model

Table 6.1: Values of the IEC 61000-4-5 standard circuit model parameters

Model Parameter	Value
C_S	8 µF
L_R	7.2 µH
R_1	25 Ω
R_2	12 Ω
R_M	1.11 Ω
R_L	1 mΩ for short-circuit current measurements 10 MΩ for open-circuit voltage measurements

6.2.1.1.2 IEC 61000-4-2 Standard Model

Similar to the IEC 61000-4-5 standard, the equivalent electrical circuit model of the ESD induced ETO presented by the IEC 61000-4-2 standard given in Figure 6.4(a) was adopted from the literature and its transformed network is presented in Figure 6.4(b), which was used for mathematical analysis. The impedances (Ω) are:

$$Z_G(s) = \frac{\frac{1}{C_G s}(R_G + L_G s)}{\frac{1}{C_G s} + R_G + L_G s} \tag{6.1}$$

$$Z_{IEC}(s) = \frac{1}{C_{IEC} s} + \frac{\frac{1}{C_{ps}}(R_{IEC})}{\frac{1}{C_{ps} s} + R_{IEC}} + L_{IEC} s \tag{6.2}$$

$$Z_L(s) = R_L \tag{6.3}$$

The initial conditions for the current through the inductor and the voltage across capacitors are presented in Table 6.2. The model parameters are presented in Table 6.3.

Table 6.2: Initial conditions for the current through the inductor and the voltage across capacitors in the IEC 61000-4-2 standard ESD modelling network

Parameter	Value
$i_{L_G}(0) = i_{L_{IEC}}(0)$	0
$v_{C_G}(0) = v_{C_S}(0)$	0
$v_{C_{IEC}}(0) = V_i$	8 kV

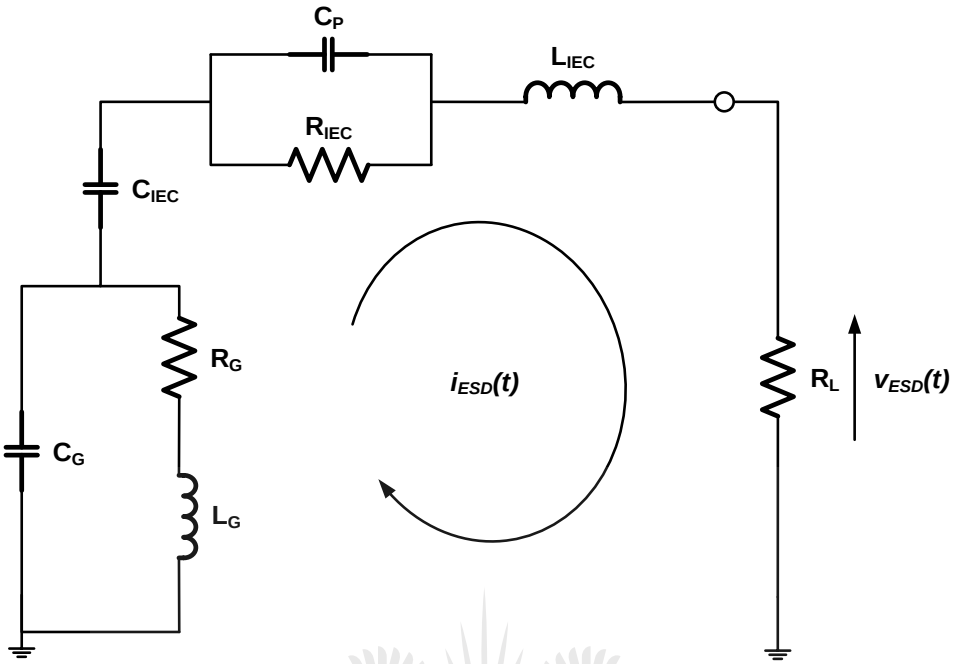

(a)

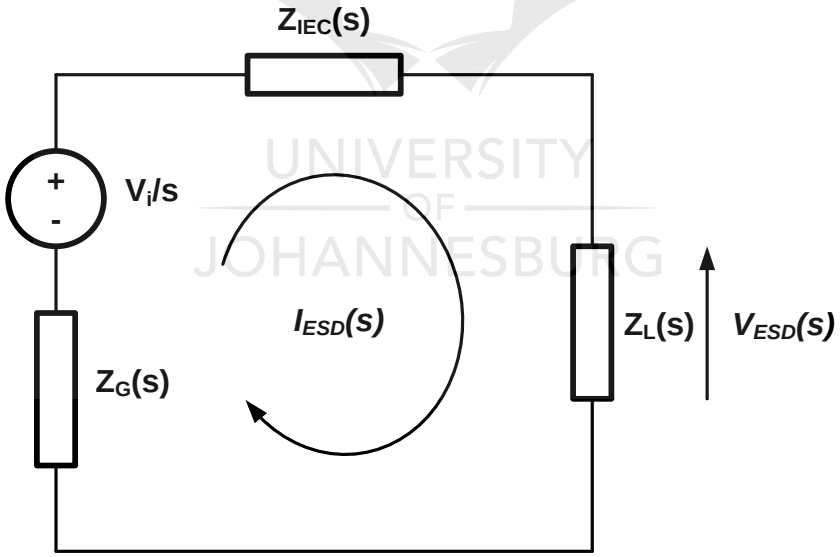

(b)

Figure 6.4: IEC 61000-4-2 standard ESD modelling network: (a) standard circuit model, and (b) Laplace transformed circuit model

Table 6.3: Values of the IEC 61000-4-2 standard circuit model parameters

Model Parameter	Value
R_{IEC}	330 Ω
R_G	40 Ω
R_L	2 Ω, for short circuit current measurements
L_{IEC}	0.16 µH
L_G	1.6 µH
C_{IEC}	150 pF
C_G	18 pF
C_P	2 pF

6.2.1.2 SJTC Modelling Network

As seen in Chapter 3, where the UHF-pattern SJTC was modelled for thermal response, no special care was needed for the SJTC output circuit (consisting of the thermocouple and output lead wires). The HE was modelled using an equivalent electrical circuit model presented by a parallel combination of heater stray capacitance and a stray inductance in series with heater energy dissipating resistance [66][67][68][69]. It was established that at low frequencies, the reactance of the HE stray components does not influence the AC-DC difference measurements of the SJTC, and only at high frequencies does the stray reactance influence the AC-DC difference measurements. This behaviour is similar to that of a non-ideal wire-wound resistor [70]; therefore, the HE of a UHF-pattern SJTC is suitable for modelling like a real resistor, represented by the simplified equivalent circuit model in Figures 6.1 and 6.2.

The conductive input lead wires could be modelled as a transmission line, represented by distributed electrical parameters (series resistance and inductance of the wire, and shunt capacitance and conductance between line and ground wires) per unit length. However, they can be regarded as a lossless transmission line, since they are of a shorter length. In the AC-DC transfer measurements, Joule heating occurs almost entirely in the HE only [34]; thus, the power dissipation on the conductive wires can be ignored. However, since the sources of ETOs used in this work are signals with high frequency, the inductance of the wires could contribute to signal attenuation. For the purpose of this work, the effect of the properties of the lead wires

on the ETO signals was assumed to be negligible. The electrical parameters of the SJTC test unit studied in this work are presented in Table 6.4.

Table 6.4: Electrical parameters of the UHF-pattern SJTC units used in this study [71]

Unit	Heater Resistance (Ω)	Capacitance (pF)	Self-Inductance (nH)
5 mA	90 ± 9	0.3	26.0

6.2.1.3 Modelling Networks of TVS Devices

The mathematical analysis of TVS devices using the LT technique is difficult [55]. This is due to the nonlinearity of their impedance characteristics, which are represented by high-order power law relationships. Therefore, the TVS devices were linearised by representing them with equivalent electrical circuit models, and only after that were they implemented for simulation analysis. The sources of ETOs used in this work have short rise times and high magnitudes of voltage peaks, which are above the breakdown voltages of the TVS devices used in this work. Therefore, the TVS devices were modelled in their "on" states. ETOs of positive polarities were assumed; therefore, unidirectional TVS device models were considered.

6.2.1.3.1 Zener Diode

For the purpose of simplicity of the mathematical analysis, the AC equivalent circuit model of the Zener diode was used [72]. The model (Figure 6.2) consist of a combination of the voltage source V_{ZD}, which represents the breakdown voltage, and a series resistor R_d, representing the dynamic resistance of the diodes when they are in the low-impedance or high-current conduction mode.

The 1N4728A Zener diode was adopted for this work. Its electrical specifications are presented in Appendix D.1. The parameters V_{ZD} and R_d are also specified in the datasheet.

6.2.1.3.2 Metal-oxide Varistor

The model of the MOV in the normal operating region, shown in Figure 6.2, was used in this work, where L_{MOV} and R_{MOV} are the varistor inductance and resistance, respectively. The 20D180K MOV was adopted for this work. Appendix D.2 presents the electrical and dimensional specifications of the MOV. The MOV inductance was calculated as 29.4 nH using Eq. (6.4):

$$L_{MOV} = \frac{\mu_0}{\pi} l_{MOV} \text{In}\left(\frac{2w_{MOV} - r_{MOV}}{r_{MOV}}\right) \quad (6.4)$$

where μ_0 is the vacuum permeability ($4\pi \times 10^{-7}$ H/m), l_{MOV}, r_{MOV} and w_{MOV} are the varistor parameters (length of the MOV lead wires, the radius of the MOV lead wires and the width between the centres of the cross-sectional areas of the parallel MOV lead wires, respectively). The resistance of the MOV, R_{MOV} in Figure 6.2, was calculated as 1.95 Ω using Eq. (6.5):

$$R_{MOV} = \frac{V_c}{I_p} \quad (6.5)$$

where $V_c = 39$ V and $I_p = 20$ A are the clamping voltage and peak current, respectively, obtained from the MOV datasheet (Appendix D.2).

6.3 Experimental Measurement-modelling Method

Equipment:

- Keysight 33600A Series Waveform Generator
- Keysight MSOS054A Mixed Signal Oscilloscope
- Fluke 5500A Calibrator
- Agilent E4980A Precision LCR Meter
- Fluke 8508A-01 Reference Multimeter
- Breadboard
- 5 mA nominal current rated UHF-pattern SJTC
- TVS devices: Zener diode and MOV
- Resistors, capacitor and inductors:

Several experiments were performed in this work:

6.3.1 Experiment 1: Establishing the Electrical Characteristics of the TVS Devices

In this experiment, the aim was to establish the protection capabilities of the commercially available Zener diode and MOV. This was achieved by determining and establishing their electrical characteristics.

The measurements were performed at room temperature using the measurement setup presented in Figure 6.5, where the test device represented either the Zener diode or MOV. A

DC voltage signal of positive polarity was injected from the calibrator voltage output into the test device through a 1 kΩ power resistor and a digital multimeter, which was monitoring the current through the test circuit, whereas an oscilloscope was used to monitor the voltage across the test device.

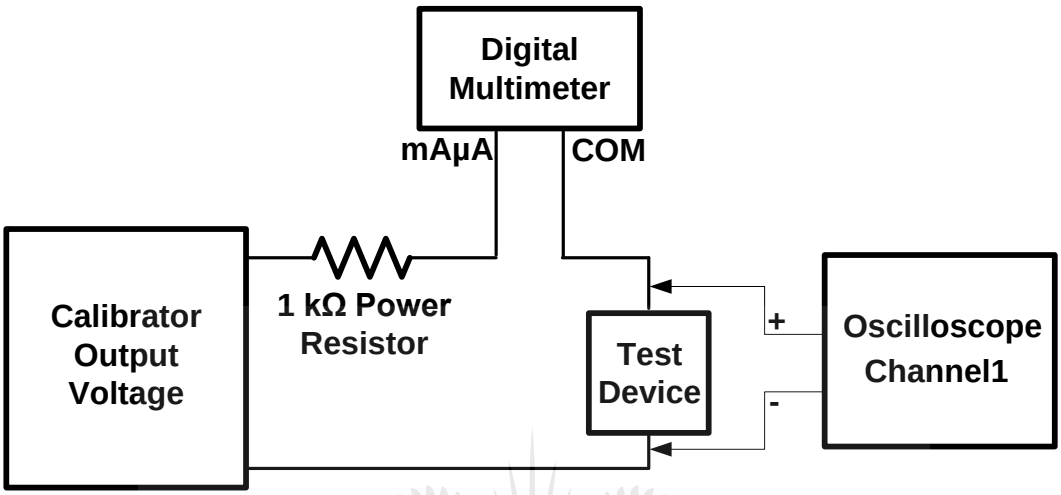

Figure 6.5: Experiment 1 setup

6.3.2 Experiment 2: Extraction of the RLC Components of the 5 mA UHF-pattern SJTC Input Circuit

In Experiment 1, it was established that the Zener diode offers a lower clamping voltage level than the MOV, which is approximately 2.4 V nominal voltage level. However, compared to the nominal ratings of the SJTC unit used in this work, this clamping voltage level is high and could damage or destroy its HE. Thus, alternative methods would be either to develop the protection circuit further or build the equivalent circuit representing the dynamic performance of the SJTC HE; the latter was considered.

Therefore, the aim of this experiment was to develop the equivalent circuit of the SJTC. First, a high-accuracy reference multimeter was used to measure the DC resistance of the SJTC units used in this work. Then a precision LCR meter was used to measure the impedance of the SJTC unit at different frequency points, ranging from 10 kHz to 2 MHz. The results obtained for impedance were then fitted to extract the capacitance and inductance parameter values of the SJTCs.

To verify the correctness of the extracted values, a circuit was built, as shown in Figure 6.6, using components with parameter values presented in Table 6.5. The calibrator voltage output was set to 1.125 V.

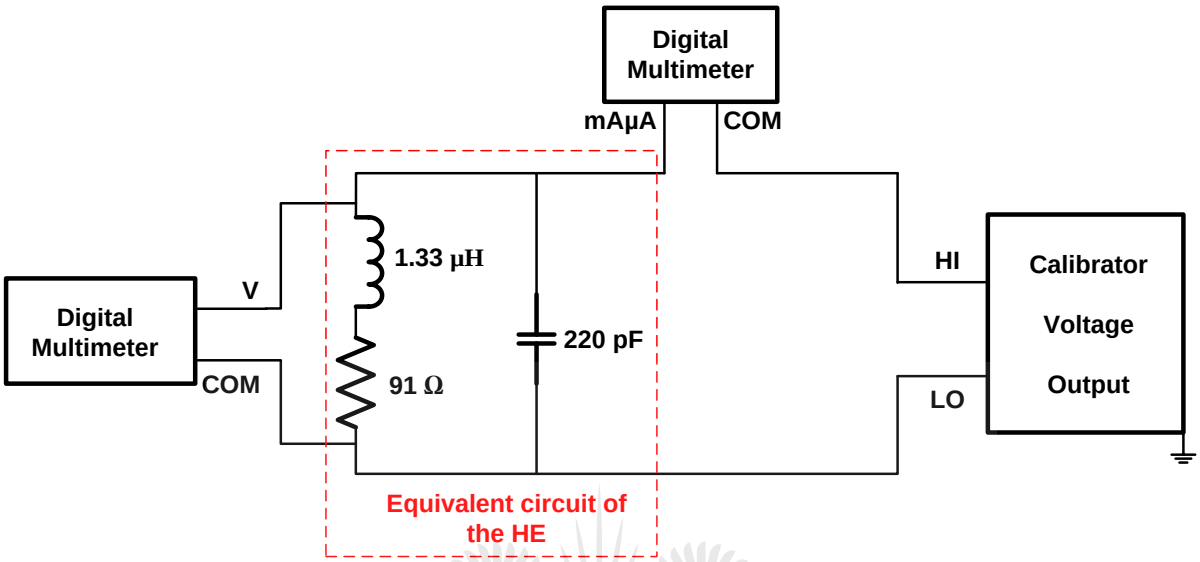

Figure 6.6: Validation of the equivalent circuit of the **5** mA SJTC HE

Table 6.5: Synthesised/modelled parameter values of the SJTC used in this work

SJTC HE Parameter	Modelled
Resistance (Ω)	91
Inductance (μH)	1.33 (1 μH and 0.33 μH inductors in series)
Capacitance (pF)	220

6.3.3 Experiment 3: Creating the Switching ETO Voltage Signal

The PSpice simulation waveform of the IEC 61000-4-5 switching voltage waveform was exported into a USB memory stick as a .csv file and edited using Microsoft Excel. The time column was changed to Number of Points and the voltage points were downscaled to meet the maximum voltage peak requirements specified by the waveform generator. The voltage waveform (.csv) was then saved into the waveform generator using a USB memory stick. The output of the waveform generator was directly coupled with the oscilloscope to capture the signal output.

6.3.4 Experiment 4: Determining the Response of the SJTC HE to the Switching ETO Voltage Signal in the Absence and Presence of TVS Device(s)

To determine the response of the 5 mA SJTC HE equivalent circuit to the absence and presence of the protection device(s), an ETO signal was injected into a line, as shown in Figure 6.7. A diode in forward bias was connected in series with the waveform generator to block the positive half of the calibrator output signal from entering the waveform generator. Since the calibrator is embedded with an overload switching relay, no avalanche diode was connected in series with the calibrator. The output of the calibrator was set to a sine-wave of 0.45 V maximum, which is the nominal voltage rating of the 5 mA SJTC, and the waveform generator output signal was set to a burst with 5 Vpp amplitude.

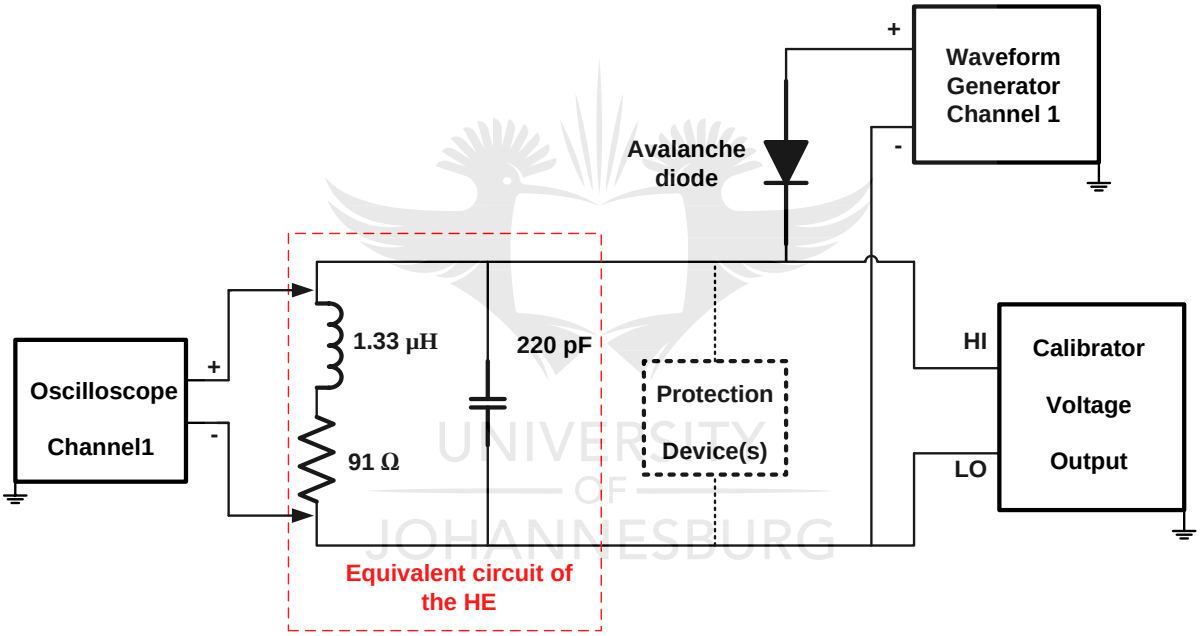

Figure 6.7: Network configuration used for experimental analysis of the response of the HE

6.4 Conclusions

In this chapter, the method used for the analysis of the response of the UHF-pattern SJTCs was presented. The equivalent electrical circuit models representing the ETO source, TOPDs, and the input circuit of the SJTC were also presented. Lastly, the experimental measurement setups and procedures used for the analysis of this work were outlined. The method developed in this work would help determine the response of the protection circuit to ETOs, and how it influence the performance of the AC-DC transfer measurement system. Consequently, this would also address the rationale for this research.

CHAPTER 7: RESEARCH FINDINGS AND DISCUSSION

7.1 Introduction

The SJTC unit used in this work can allow a maximum of 250% of the nominal input to be applied to the HE. That is, a 90 Ω SJTC unit with nominal current and voltage of 5 mA and 0.45 V, respectively, can allow a maximum input current of 12.5 mA or a maximum input voltage of 1.125 V, thus a maximum power dissipation of 14.06 mW. This maximum power dissipation magnitude of the HE is relatively close to 14.25 mW calculated in Section 3.3. If an input greater than these values is applied to the HE, the HE is expected to be damaged or destroyed.

In Chapter 6 the methods used to determine the response of the SJTC with and without a protection device against ETOs were discussed. The mathematical analysis of the standard waveforms and the simulation results of the circuit model with and without ETO protection are presented and discussed in Section 7.2. The results obtained are presented and discussed in this chapter.

7.2 Simulation Results and Discussion

7.2.1 IEC 61000-4-5 Standard

The results for the short-circuit current and open-circuit voltage (generated by IEC 61000-4-5 standard combination wave generator circuit (Figure 6.3)) are presented in Figure 7.1(a) and (b), respectively. The open- and short-circuit simulation results give the magnitudes of the voltage and current, respectively, which could be expected by the input circuit of any load directly coupled to the IEC 61000-4-5 standard combination wave generator circuit. Each figure plots a set of PSpice simulation model and mathematical model (development of equations presented in Appendix C.1) waveforms for numerical validation purposes. Equations (7.1) and (7.2) present the time domain expressions for the mathematical models of current $i_{short}(t)$ and voltage $v_{open}(t)$ waveforms, respectively:

$$i_{short}(t) = A_1 e^{\alpha_1 t} - (A_2 \cos(\omega_1 t) - A_3 \sin(\omega_1 t)) e^{\alpha_2 t} \tag{7.1}$$

$$v_{open}(t) = A_4 e^{\alpha_3 t} - (A_5 \cosh(\omega_2 t) - A_6 \sinh(\omega_2 t)) e^{\alpha_4 t}. \tag{7.2}$$

The model parameters are presented in Table 7.1, and t is the time (s).

Table 7.1: Model parameters of Eqs. (7.1) and (7.2)

Parameter	Value	Parameter	Value
A_1	1.2×10^{-17} A	α_1	-1.5×10^{5} s^{-1}
A_2	1.2×10^{-17} A	α_2	-8.0×10^{4} s^{-1}
A_3	6.8×10^{2} A	α_3	-1.8×10^{6} s^{-1}
A_4	1.4×10^{-15} V	α_4	-9.1×10^{5} s^{-1}
A_5	1.4×10^{-15} V	ω_1	1.1×10^{5} rad/s
A_6	9.8×10^{2} V	ω_2	9.0×10^{5} rad/s

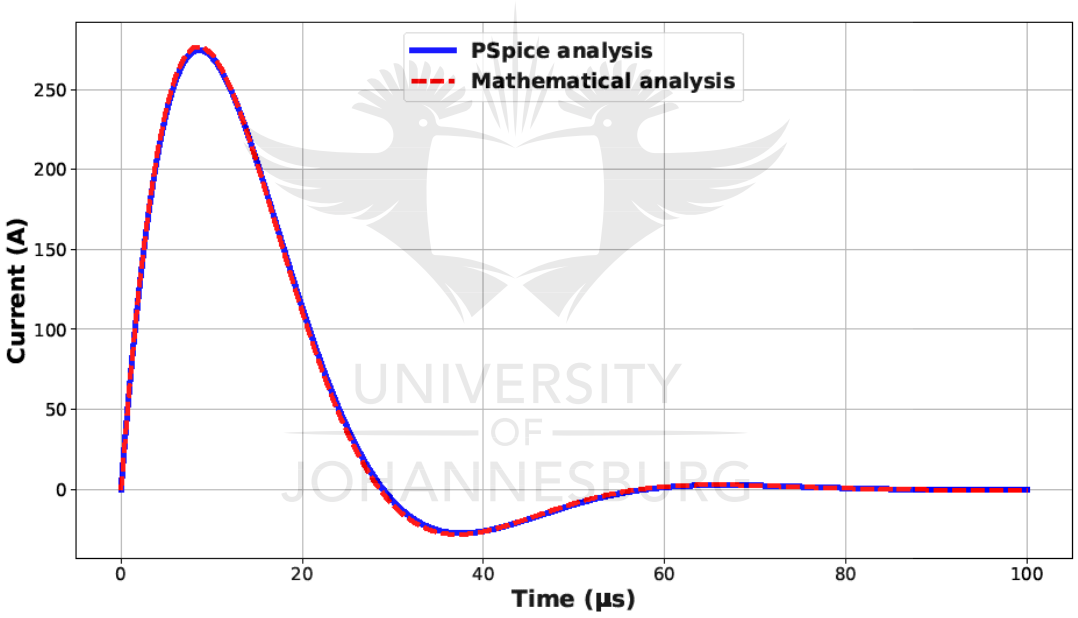

(a)

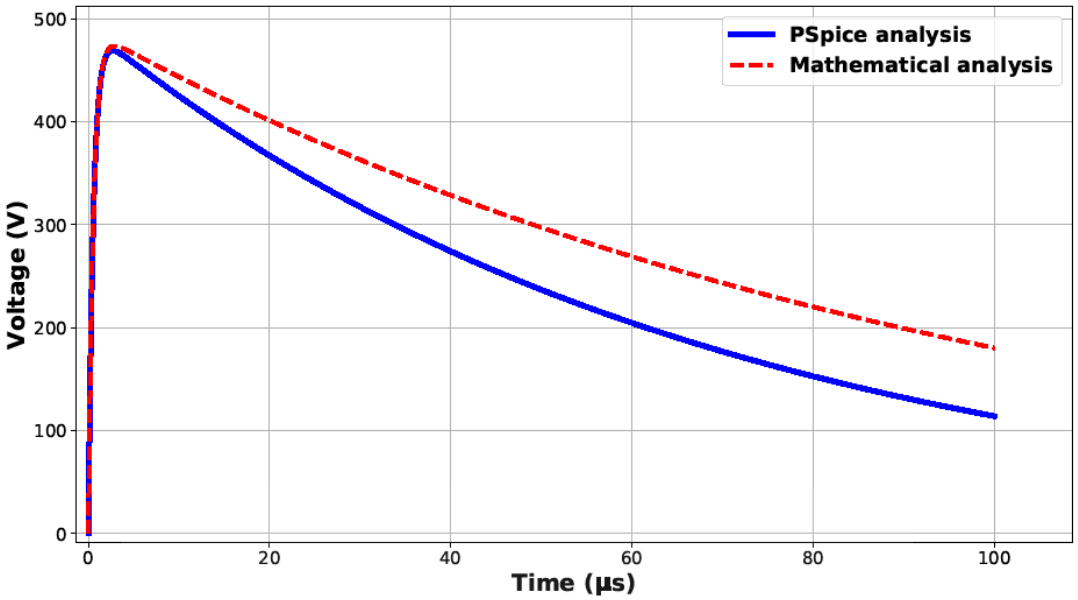

(b)

Figure 7.1: IEC 61000-4-5 standard switching ETO waveforms: (a) short-circuit current, and (b) open-circuit voltage

Tables 7.2 and 7.3 present the measured parameters of the IEC 61000-4-5 standard short-circuit current and open-circuit voltage waveforms, which were obtained from PSpice simulation profiles. These parameters are comparable to the ones provided by the standard, and it can be deduced from the measurements that the IEC 61000-4-5 standard combination wave generator circuit (with the chosen parameters) used in this work satisfies the requirements set by the standard. However, a deviation is observed in the open-circuit voltage waveforms. The waveforms follow a similar trend of reaching the maximum voltage magnitude and decaying; however, the PSpice and mathematical analysis waveforms do not overlap each other.

Table 7.2: IEC 61000-4-5 standard short-circuit current waveform measured parameters

Parameter	Standard	Measured
Rise time (µs)	8 ± 1.6	6.50
Half duration (µs)	20 ± 4	18.7
Peak magnitude (A)	250	275
% Undershoot	30%	10%

Table 7.3: IEC 61000-4-5 standard open-circuit voltage waveform measured parameters

Parameter	Standard	Measured
Rise time (µs)	1.2 ± 0.36	1.60
Half duration (µs)	50 ± 10	50.8
Peak magnitude (V)	500	469

7.2.1.1 *Case 1* Mathematical Analysis and Simulation Results

The PSpice simulation results of the response of the HE to the switching ETO in accordance with the IEC 61000-4-5 standard are presented in Figure 7.2, which presents the current, voltage and power dissipation of the HE of the 5 mA nominal current rated UHF-pattern SJTC. Additional axes are included in Figure 7.2(c) to magnify a portion of the waveform. The red dashed lines on these plots indicate the maximum operating margins of the SJTC HE in question. Table 7.4 presents the peak values, which were measured in their PSpice simulation profiles.

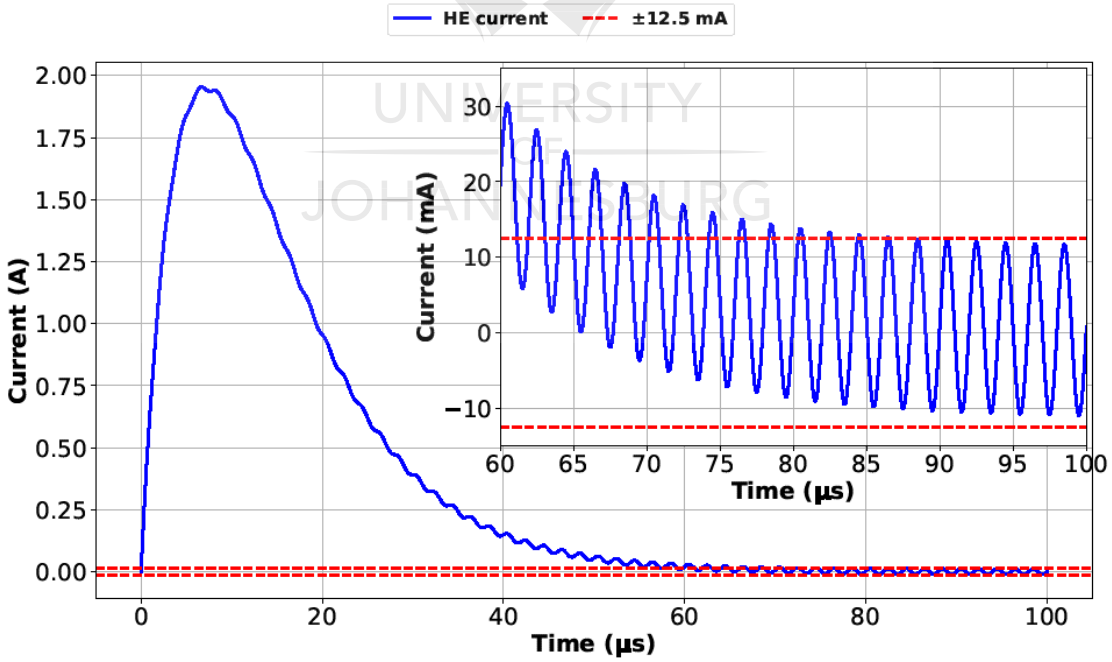

(a)

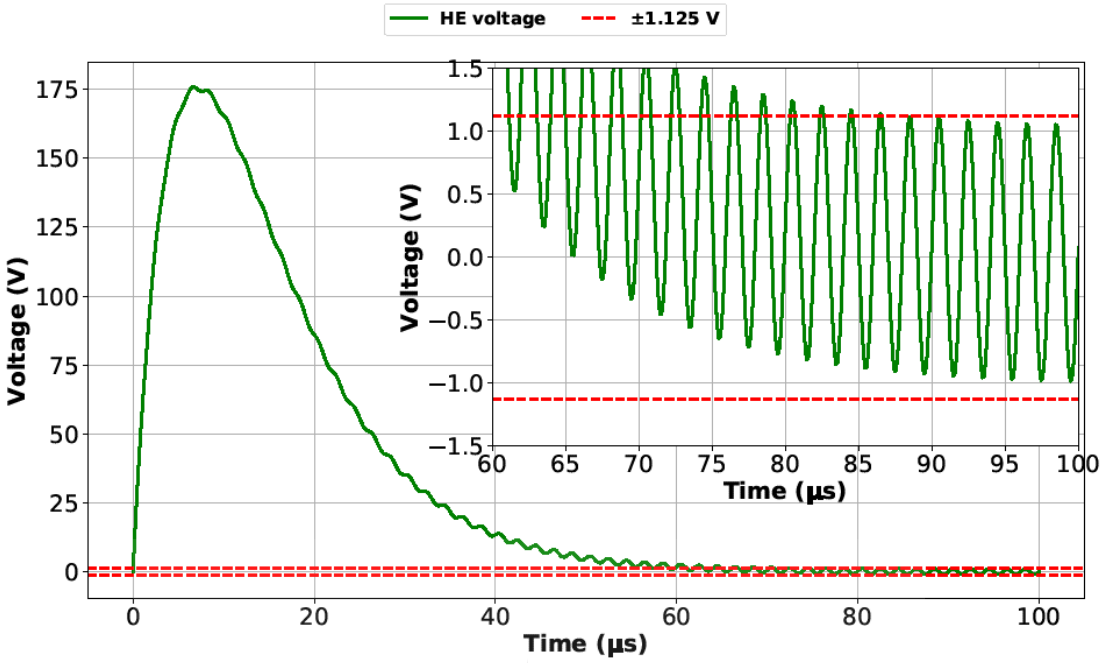

(b)

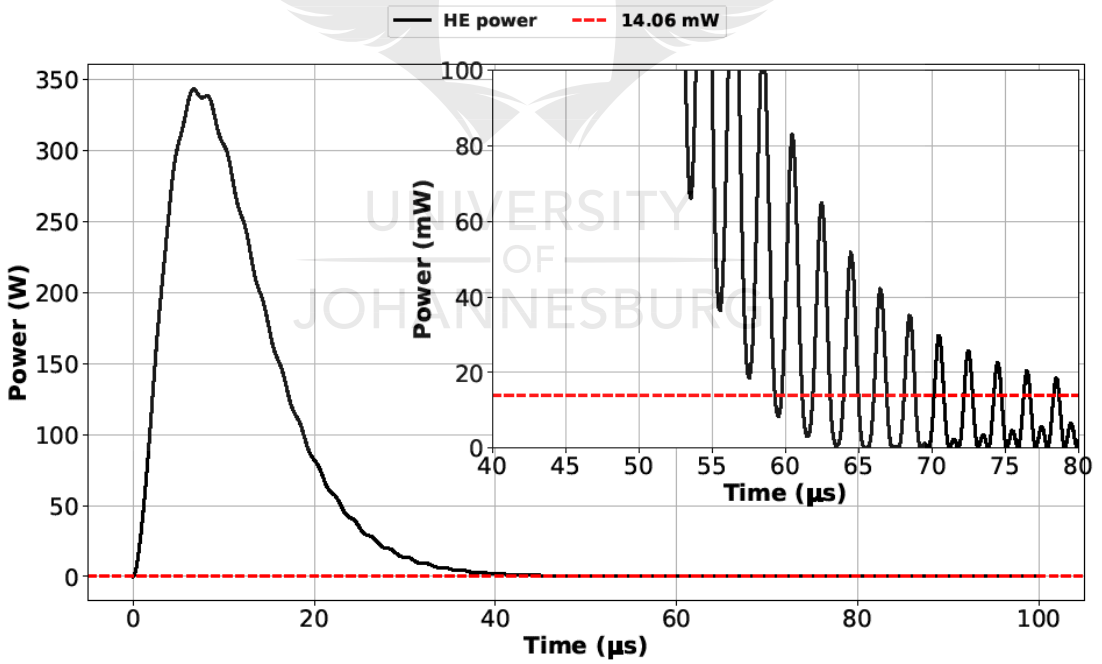

(c)

Figure 7.2: IEC 61000-4-5 ETO: (a) current through the HE, (b) voltage across the HE, and (c) power dissipated by the HE

Table 7.4: Maximum electrical parameter values measured on the HE

Measured on	Max Current (A)	Max Voltage (V)	Max power (W)
5 mA SJTC	1.954	175.8	345.0

7.2.1.2 *Case 2* Simulation Results

Figure 7.3 presents the response of the HE and the protection element when each of the TVS devices was implemented individually and simultaneously in a multi-stage protection element, as discussed in Chapter 6. Additional axes are included to magnify the portions of the waveforms. The red dashed lines on Figure 7.3(a), (c) and (d) indicate the maximum operating margins of the SJTC HE in question. The maximum waveform parameters of the response of the HE and the protection elements when the Zener diode, MOV and the multi-stage protection element were implemented in accordance with *Case 2* are presented in Tables 7.5 and 7.6.

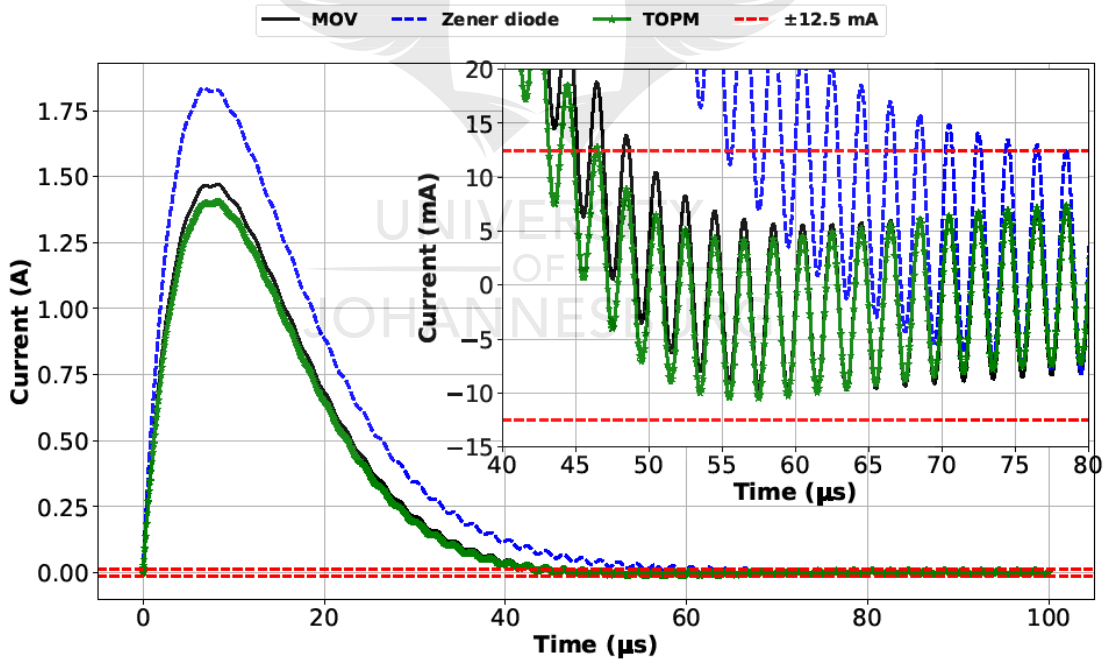

(a)

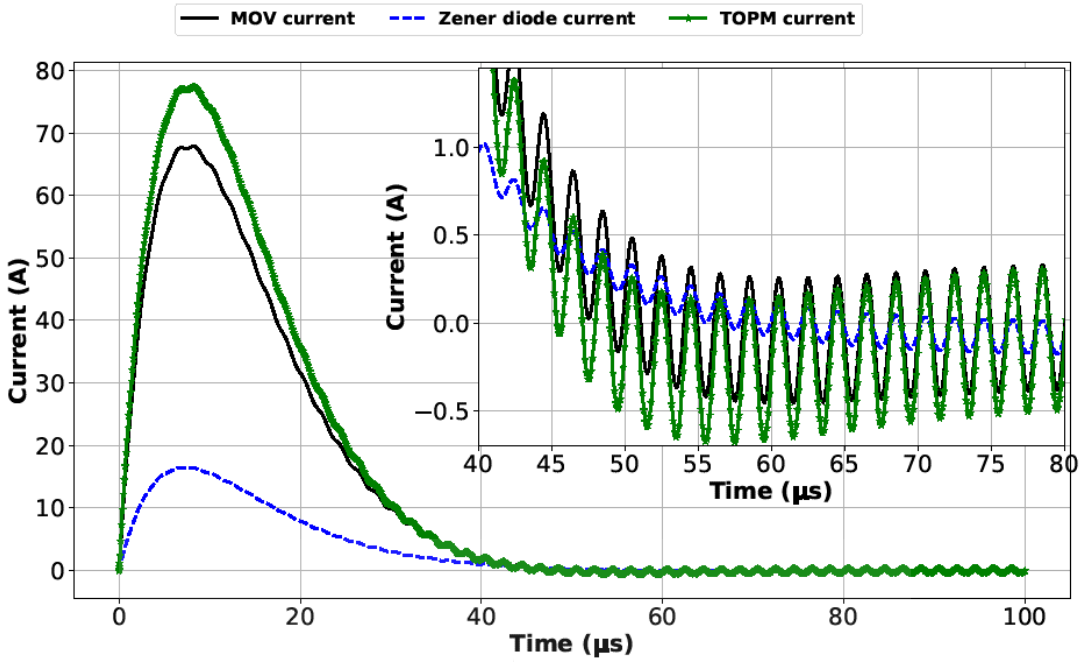

(b)

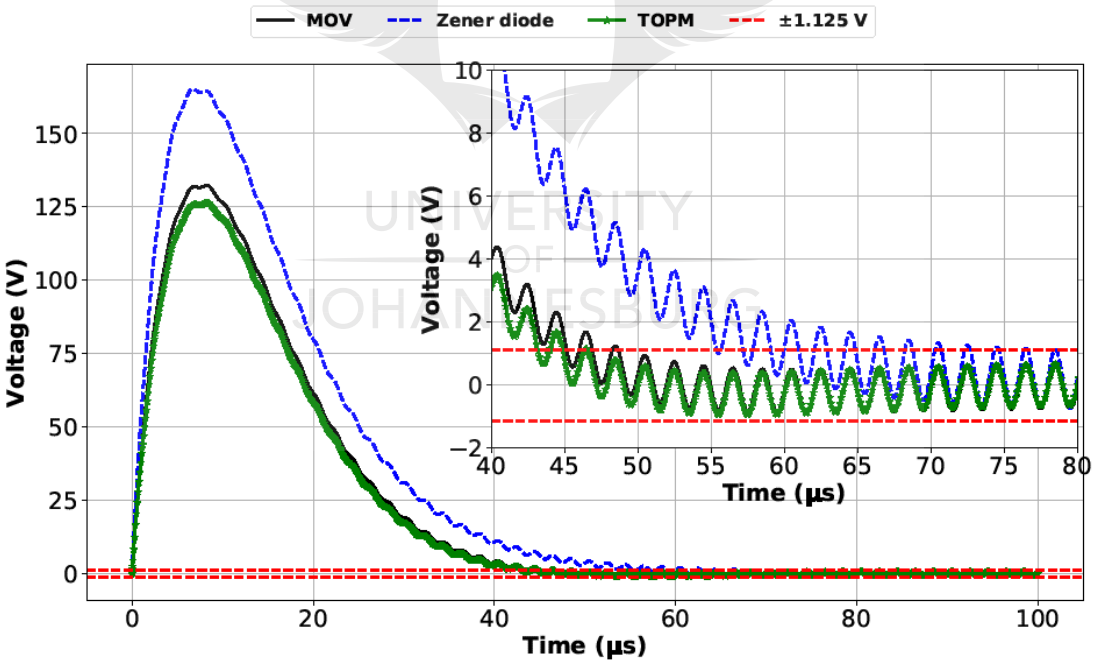

(c)

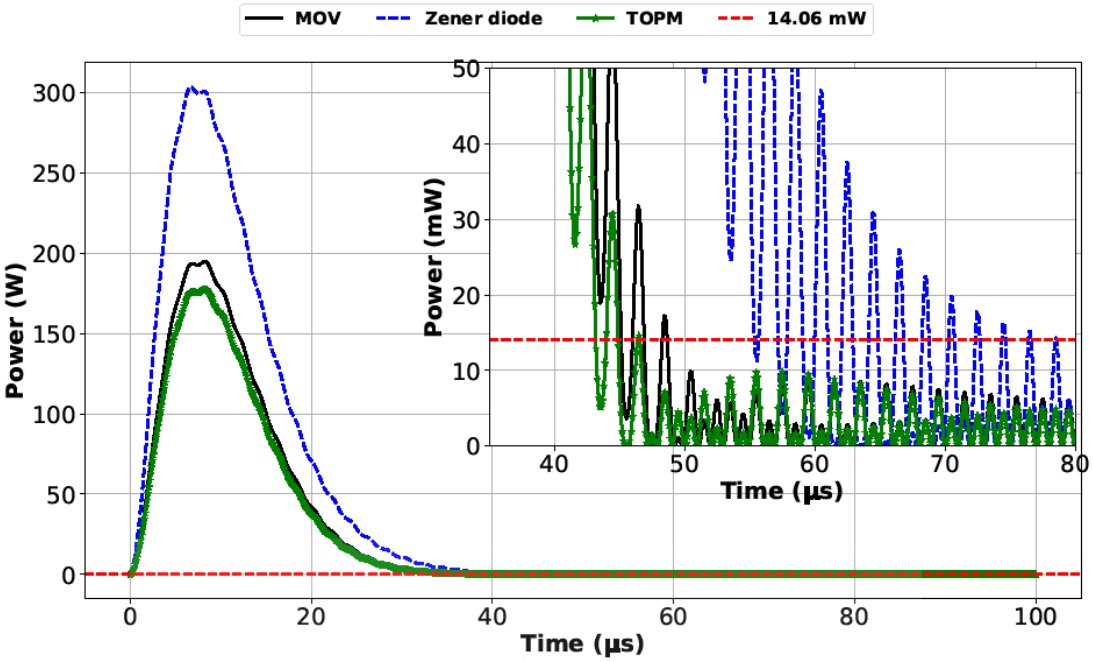

(d)

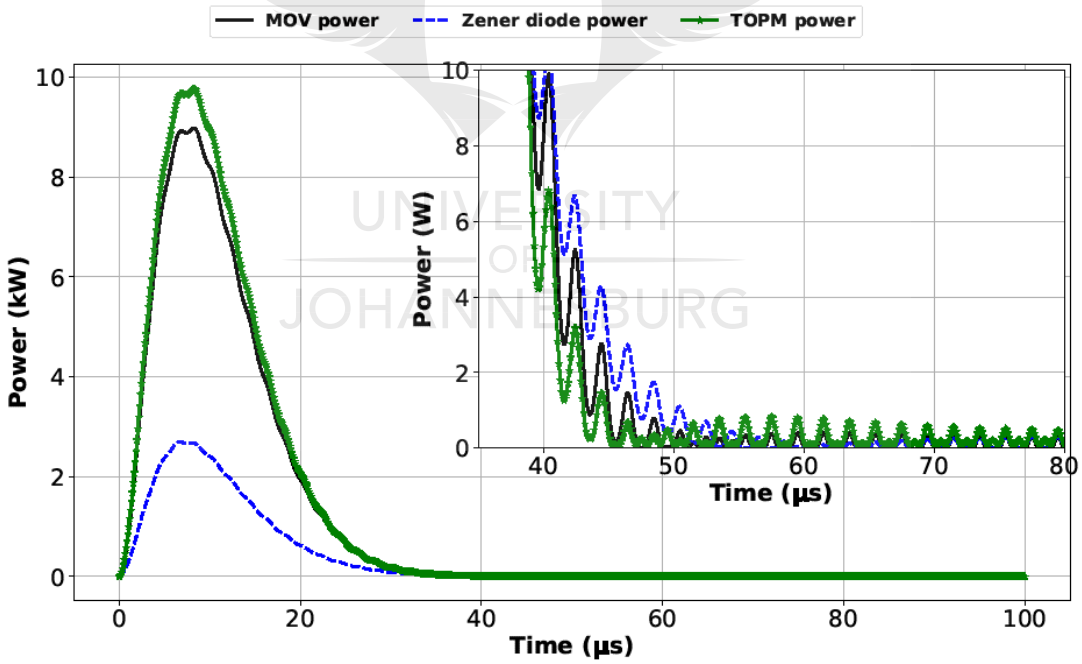

(e)

Figure 7.3: IEC 61000-4-5 ETO: (a) current through the HE, (b) current through the protection elements, (c) voltage across the HE, (d) power dissipated by the HE, and (e) power dissipated by the protection elements

Table 7.5: Comparison of the maximum electrical parameter values measured on the HE

Protection device used	Max Current (A)	Max Voltage (V)	Max power (W)
Zener diode	1.836	165.2	303.3
MOV	1.471	132.6	194.6
TOPM	1.404	126.4	178.0

Table 7.6: Comparison of the maximum electrical parameter values measured on the protection elements

Protection device used	Max Current (A)	Max Voltage (V)	Max power (kW)
Zener diode	16.42	165.2	2.697
MOV	67.87	132.6	8.981
TOPM	77.36	126.4	9.770

7.2.2 IEC 61000-4-2 ESD Standard

The results for the ESD current generated by the IEC 61000-4-2 ESD standard (circuit model presented in Figure 6.4) are presented in Figure 7.4. The figure contains a set of PSpice simulation model and mathematical model waveforms for verification purposes. Equation (7.3) presents the time domain expression for the mathematical model of the IEC 61000-4-2 ESD current $i_{ESD}(t)$ waveform:

$$i_{ESD}(t) = \left(B_1 cos(\omega_3 t) + B_2 sin(\omega_3 t)\right)e^{\alpha_8 t} - \left(B_3 cos(\omega_4 t) + B_4 sin(\omega_4 t)\right)e^{\alpha_9 t} + B_5 e^{\alpha_{10} t}. \quad (7.3)$$

The model parameters are presented in Table 7.7, and t is the time (s).

Table 7.7: Model parameters of Eq. (7.3)

Parameter	Value (A)	Parameter	Value
B_1	-22	α_8	-6.7×10^8 s^{-1}
B_2	23	α_9	-9.3×10^7 s^{-1}
B_3	4.0	α_{10}	-1.9×10^7 s^{-1}
B_4	24	ω_3	1.7×10^9 rad/s
B_5	26	ω_4	1.6×10^8 rad/s

Table 7.8 presents the measured parameters of the IEC 61000-4-2 ESD standard current waveform, which were obtained from the PSpice simulation profile. These parameters are comparable to the ones provided by the standard and it can be deduced from the measurements that the IEC 61000-4-2 standard ESD generator circuit (with the chosen parameters) used in this work satisfies the requirements set by the standard.

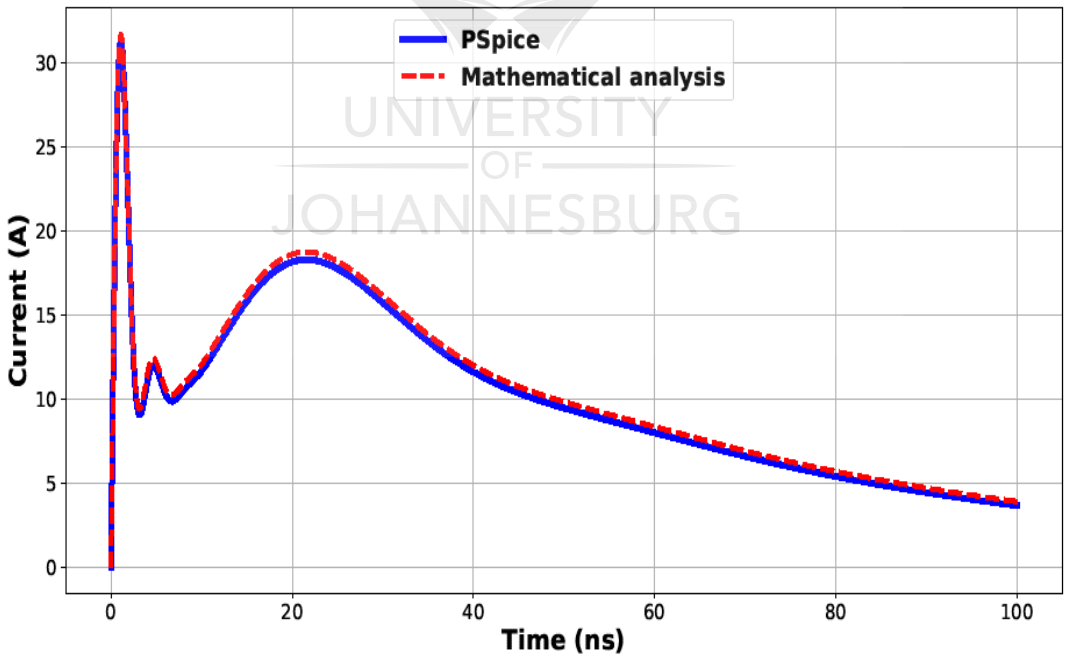

Figure 7.4: IEC 61000-4-2 ESD standard waveforms

Table 7.8: IEC 61000-4-2 ESD standard current waveforms measured parameters

Measured parameter	Standard	Measured
Rise time (ns)	0.7 - 1	0.7
Peak current magnitude (A)	30 $\pm$ 3	31.3
Current magnitude at 30 ns (A)	16 $\pm$ 1.6	15.7
Current magnitude at 60 ns (A)	8 $\pm$ 2.4	7.99

7.2.2.1 *Case 1* Mathematical Analysis and Simulation Results

Similar to Section 7.2.1, the PSpice simulation results of the HE response to the ESD-induced ETO, in accordance with the IEC 61000-4-2 ESD standard, are presented in Figure 7.5. Additional axes are included to magnify the part of the waveforms. The red dashed lines on these plots indicate the maximum operating margins of the SJTC HE in question. Table 7.9 presents the parameters of the waveforms representing the response of the HE.

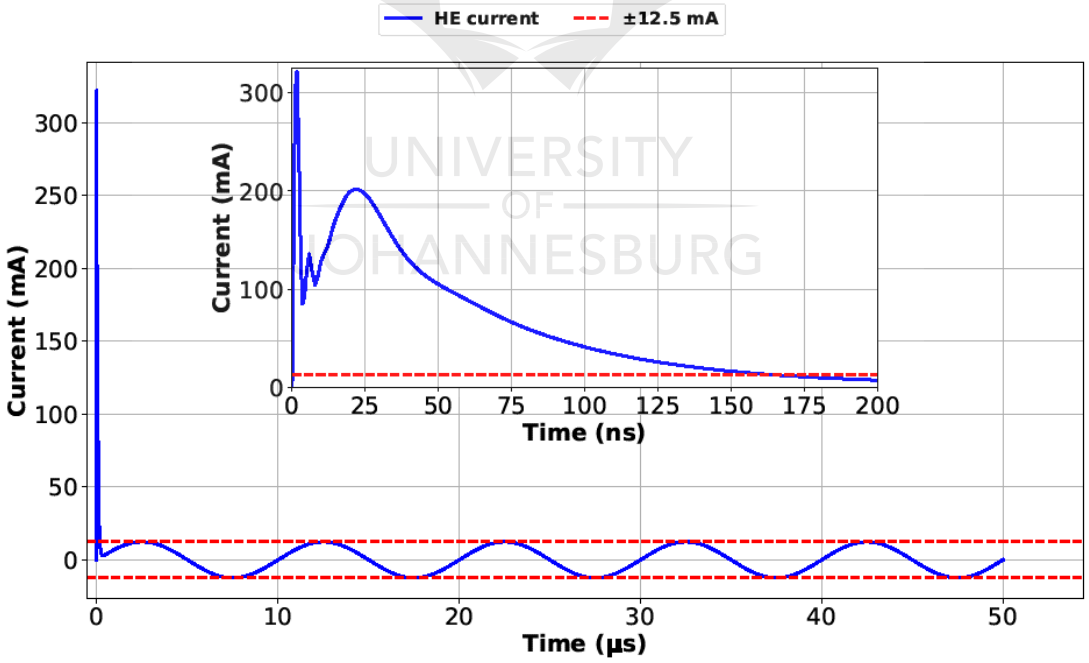

(a)

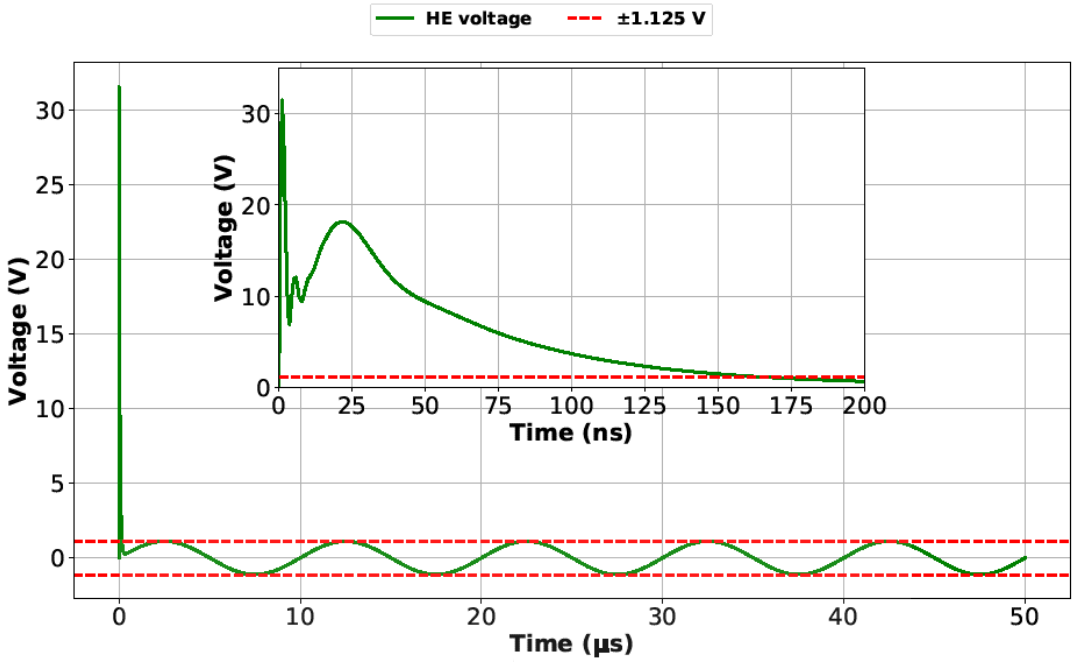

(b)

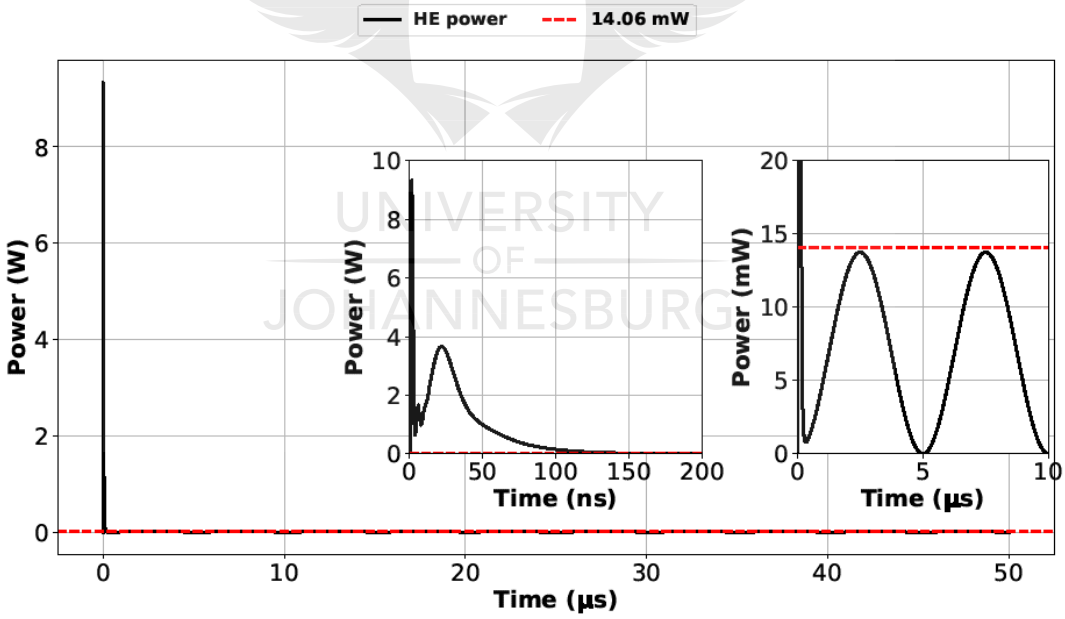

(c)

Figure 7.5: IEC 61000-4-2 ETO: (a) current through the HE, (b) voltage across the HE, and (c) power dissipated by the HE

Table 7.9: Maximum electrical parameter values measured on the HE

Measured on	Max Current (A)	Max Voltage (V)	Max power (W)
5 mA SJTC	0.3275	31.52	9.340

7.2.2.2 *Case 2* Simulation Results

Similar to Section 7.2.1.2, Figure 7.6 shows the response of the HE and the protection element when each of the TVS devices was implemented individually and simultaneously in a multi-stage protection element, as discussed in Chapter 6. Additional axes are included to magnify the part of the waveforms. The red dashed lines in Figure 7.6(a), (c) and (d) indicate the maximum operating margins of the SJTC HE in question. The parameters of the response of the HE and the protection element when the Zener diode, MOV and the multi-stage protection element were implemented in accordance with *Case 2*, which were measured in their PSpice simulation profiles, are presented in Tables 7.10 and 7.11.

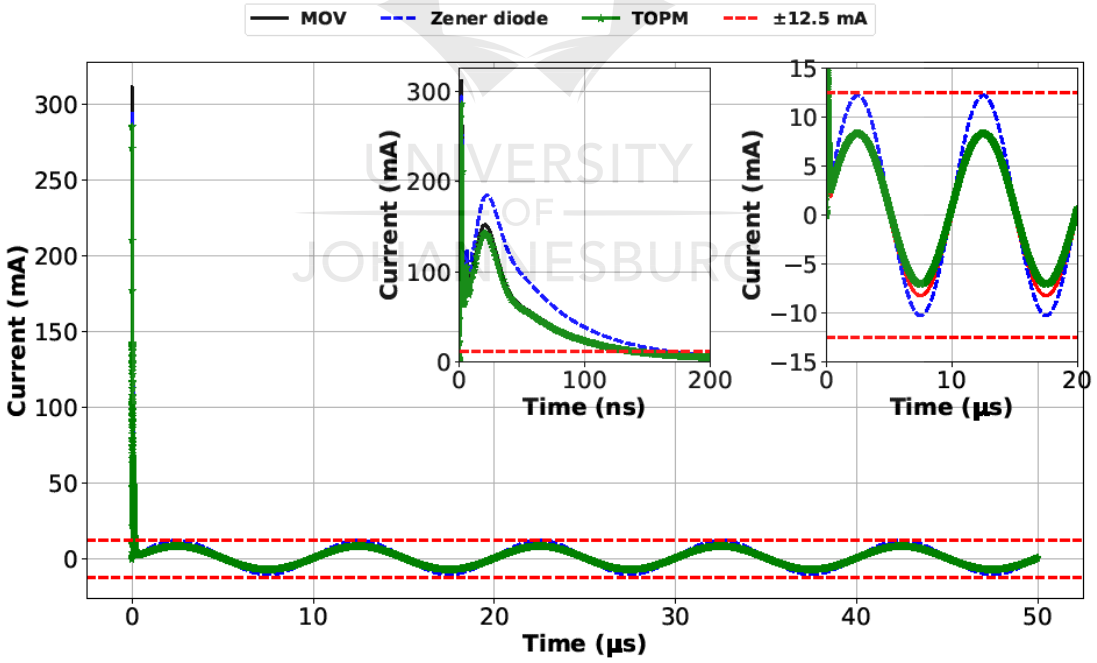

(a)

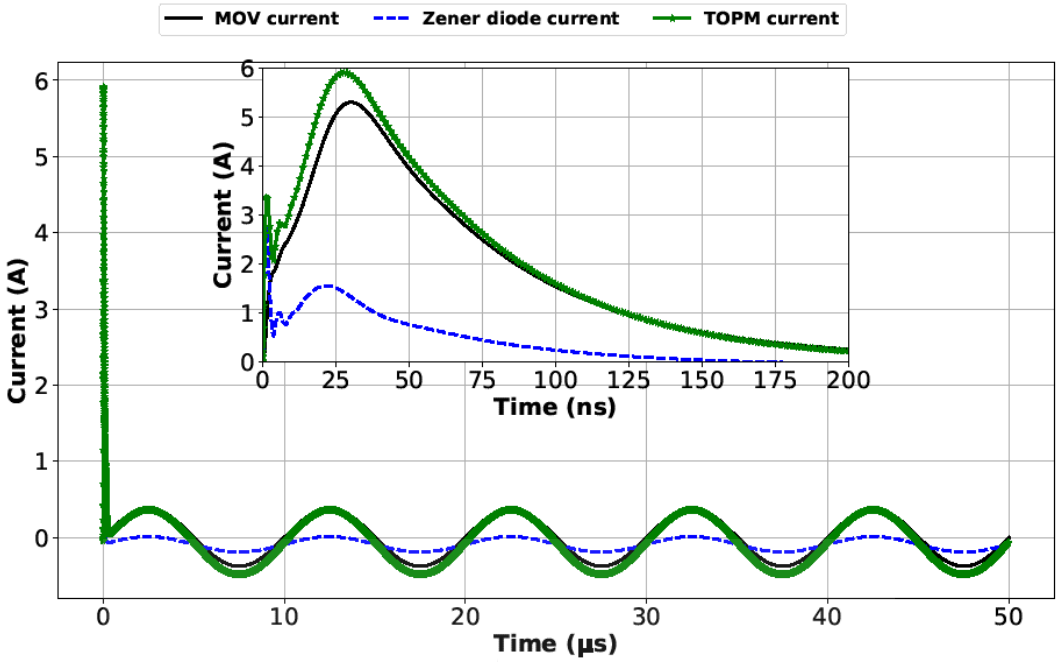

(b)

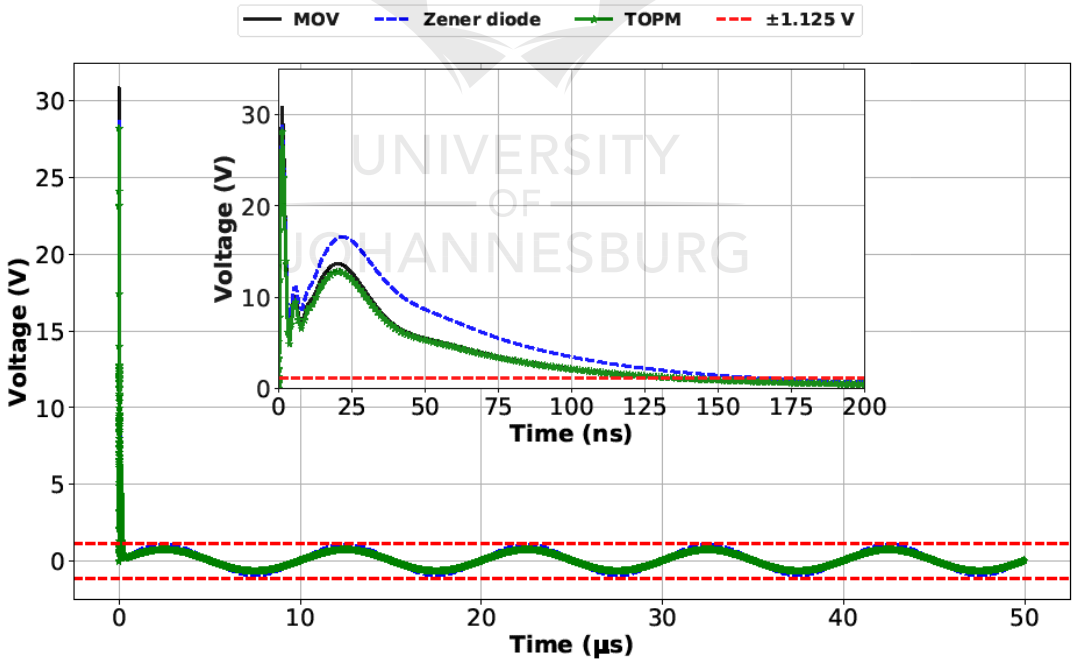

(c)

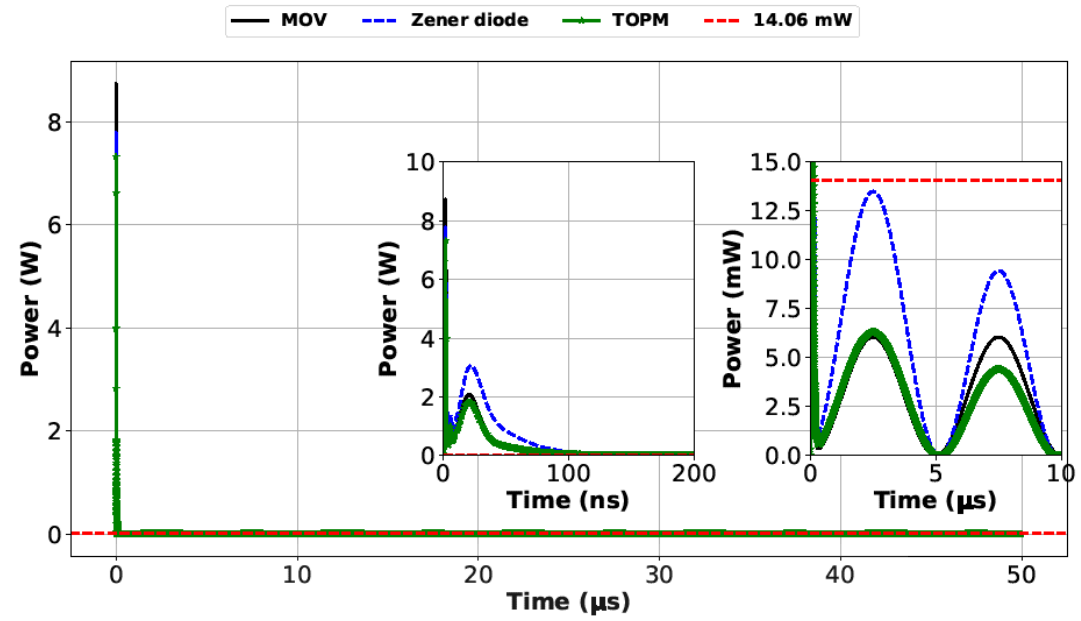

(d)

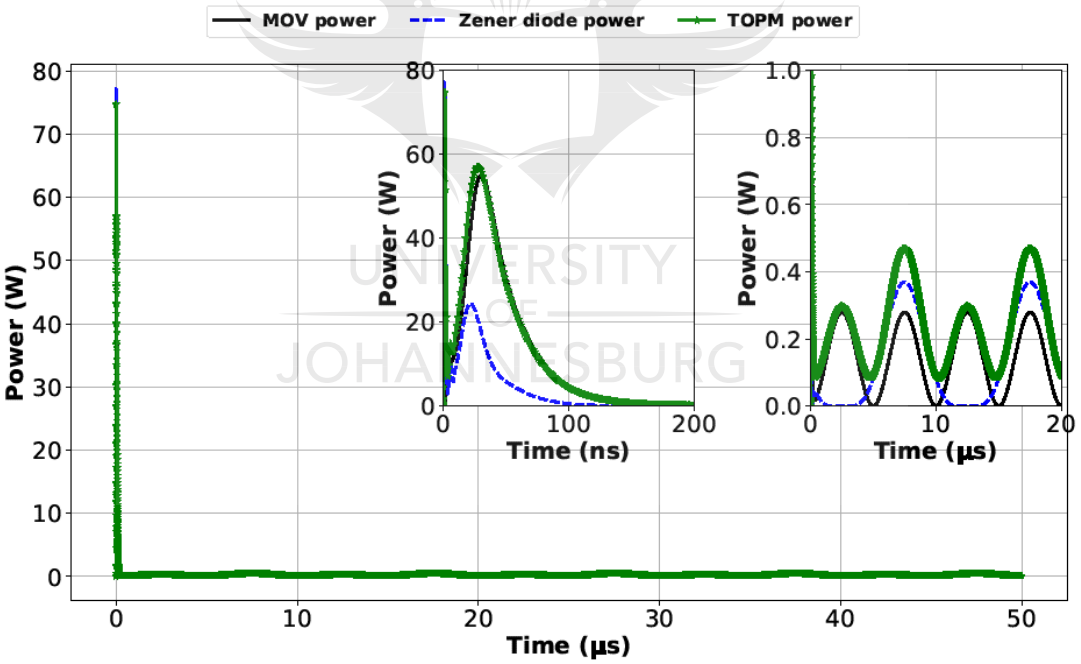

(e)

Figure 7.6: IEC 61000-4-2 ETO: (a) current through the HE, (b) current through the protection elements, (c) voltage across the HE, (d) power dissipated by the HE, and (e) power dissipated by the protection elements

Table 7.10: Comparison of the maximum electrical parameter values measured on the HE

Protection device used	Max Current (A)	Max Voltage (V)	Max power (W)
Zener diode	0.2941	28.78	7.783
MOV	0.3115	30.81	8.735
TOPM	0.2853	28.19	7.324

Table 7.11: Comparison of the maximum electrical parameter values measured on the protection elements

Protection device used	Max Current (A)	Max Voltage (V)	Max power (W)
Zener diode	2.778	28.78	77.15
MOV	5.309	30.81	54.95
TOPM	5.913	28.19	74.74

7.2.3 Discussion of Results

In order to determine the response of a 5 mA nominal current rated UHF-pattern SJTC to ETOs (in accordance with the IEC 61000-4-5 switching and IEC 61000-4-2 ESD standards) with and without the TOPD(s) implemented, mathematical models for the standard ETO models and simulation models were developed. Pspice simulation results for *Case 1* and *Case 2* are discussed in Sections 7.2.3.1 and 7.2.3.2, respectively.

7.2.3.1 Discussion of *Case 1* Simulation Results

From the results obtained, which are presented in Figures 7.2 (for the switch-induced ETO) and 7.5 (for the ESD-induced ETO), it is evident that the current, voltage and power dissipated by the HE reach high values, as can be seen in Tables 7.4 (for the switch-induced ETO) and 7.9 (for the ESD-induced ETO). The magnitudes of these measured electrical parameters are higher than the expected safe operating or permissible input margins of a 5 mA nominal current rated UHF-pattern SJTC, which were discussed in the introductory section of this chapter.

Therefore, it can be deduced from the results that the 5 mA nominal current rated UHF-pattern SJTC is expected to be destroyed completely should a switch- or ESD-induced ETO occur and be coupled directly into a line connected to the HE. The ESD-induced event occurs much faster than the switch-induced ETO event; therefore, it would destroy the HE faster.

7.2.3.2 Discussion of *Case 2* Simulation Results

Tables 7.5 and 7.10 show that implementation of a TVS device(s) greatly reduces the current, voltage and power dissipation by the HE, whereas Tables 7.6 and 7.11 show that higher electrical parameters are measured on the TVS device(s). The results show that the current that takes the HE branch is lower compared to the current through the TVS device(s) and this is because TVS devices, in their "on" state, present a lower impedance compared to the HE. Similarly, since more current flows through the branch with lower impedance, higher power dissipation is observed in the TVS device(s) than on the HE. The voltage across the TVS device(s) is also reduced to a lower (clamping) level, which applies to the SJTC.

The results obtained for the response of both the HE and the multi-stage protection element indicate that implementation of the TOPDs in a multi-stage technique has a better protection capability than when the TOPDs are implemented individually.

7.2.3.2.1 Zener Diode and MOV Implemented Individually as the only Protection Device

Response to IEC 61000-4-5 switching standard ETO

Lower current conduction was measured on the HE when the Zener diode was implemented as the only TOPD than when the MOV was implemented. Consequently, lower heat absorption (power dissipation) was measured on the HE. Furthermore, lower current conduction and heat absorption (power dissipation) were measured on the Zener diode than on the MOV. This behaviour of the models used in this work was expected, since the Zener diode has a single *p-n* junction, whereas the MOV has multiple *p-n* junctions, which enables it to conduct more current and dissipate more power than the Zener diode. A higher voltage was measured across the HE when the Zener diode was implemented as the only TOPD than when the MOV was implemented.

Response to IEC 61000-4-2 ESD standard ETO

Higher current conduction was measured on the HE when the Zener diode was implemented as the only TOPD than when the MOV was implemented. Consequently, higher heat absorption (power dissipation) was measured on the HE. Furthermore, lower current conduction and higher heat absorption (power dissipation) were measured on the Zener diode than on the MOV. A lower voltage was measured across the HE when the Zener diode was implemented as the only TOPD than when the MOV was implemented.

7.2.3.2.2 Zener Diode and MOV Implemented in a Multi-stage Protection Circuit

Response to IEC 61000-4-5 switching standard ETO

Implementation of the TOPM compared to the individual implementation of the Zener diode and MOV shows that lower current conduction on the HE was achieved; hence, lower power dissipation was measured on the HE. Consequently, higher current and power dissipation were measured on the TOPM. Lower voltage was measured across the HE.

Response to IEC 61000-4-2 ESD standard ETO

Implementation of the TOPM compared to the individual implementation of the Zener diode and MOV shows that lower current conduction on the HE was achieved; hence, lower power dissipation was measured on the HE. Consequently, higher current and power dissipation were measured on the TOPM. However, the power dissipated by the TOPM is lower than that dissipated by the Zener diode. Lower voltage was measured on the HE.

7.3 Experimental Measurement Results and Discussion

7.3.1 Experimental Measurement Results

7.3.1.1 Experiment 1: Establishing the Electrical Characteristics of the TVS Devices

Figures 7.7 and 7.8 present the electrical characteristics of the Zener diode and MOV respectively. From the results obtained, it was observed that the Zener diode offers lower clamping characteristics than the MOV. Furthermore, the measured results correlate with the datasheets.

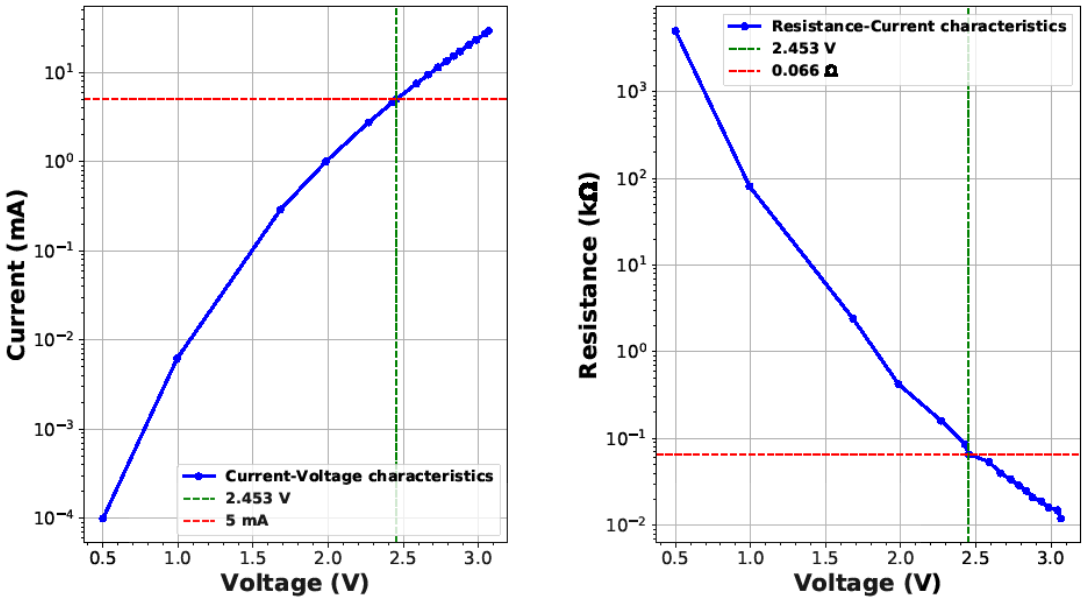

Figure 7.7: Electrical characteristics of Zener diode

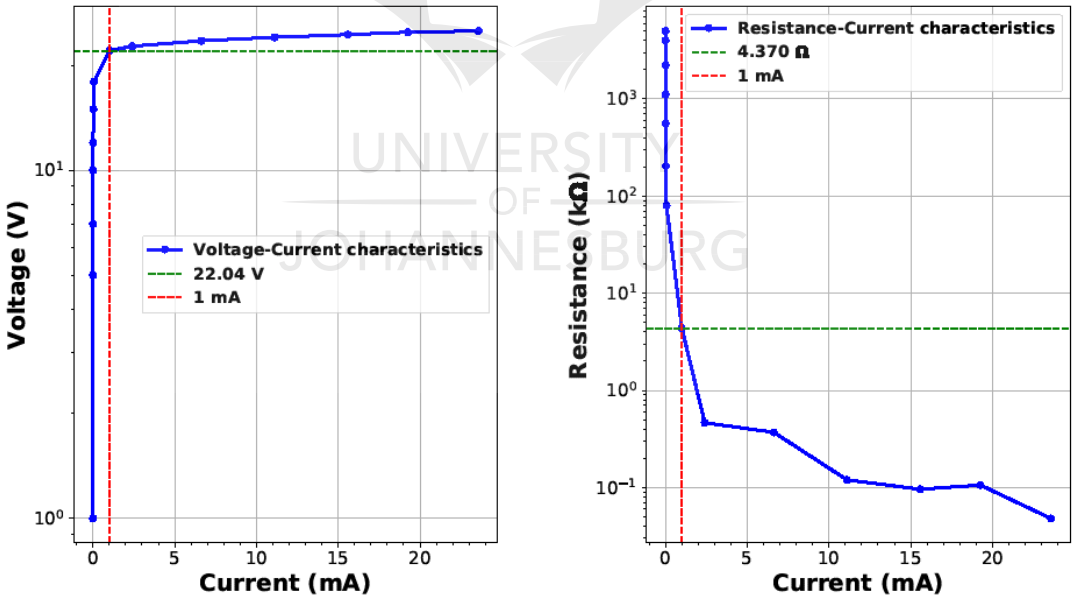

Figure 7.8: Electrical characteristics of MOV

7.3.1.2 Experiment 2: Extraction of the RLC Components of the 5 mA UHF-pattern SJTC Input Circuit

The DC resistance of the 5 mA nominal current rated UHF-pattern SJTC was measured as 89.16808 Ω. Table 7.12 presents the resistance (Ω) and reactance (Ω) at particular frequencies (Hz). Using the Octave program presented in Appendix E, the extraction values for the SJTC equivalent circuit parameters were found to be $L_H = 1.3806$ µH and $C_H = 267.7$ pF. From the validation of the equivalent circuit of the SJTC HE, the current was measured as 12.15 mA and the voltage as 1.112 V.

Table 7.12: Resistance and reactance of SJTCs measured at different frequencies

SJTC	Frequency (kHz)	Resistance (Ω)	Reactance (Ω)
5 mA UHF-pattern. Measured at 450 mV input.	10	89.99	0.06053
	20	90.00	0.1156
	50	90.01	0.2891
	100	90.03	0.5716
	200	90.06	1.131
	500	90.22	2.765
	1000	90.67	5.350
	2000	91.88	9.813

7.3.1.3 Experiment 3: Creating the Switching ETO Voltage Signal

Figure 7.9 presents the experimentally measured IEC 61000-4-5 switch-induced ETO, which was created using an arbitrary waveform generator. The ETO signal was downscaled to meet the maximum voltage peak of 10 Vpp, which is specified by the waveform generator. The waveform has a rise time of 4.9 µs and a decay time of 70.6 µs.

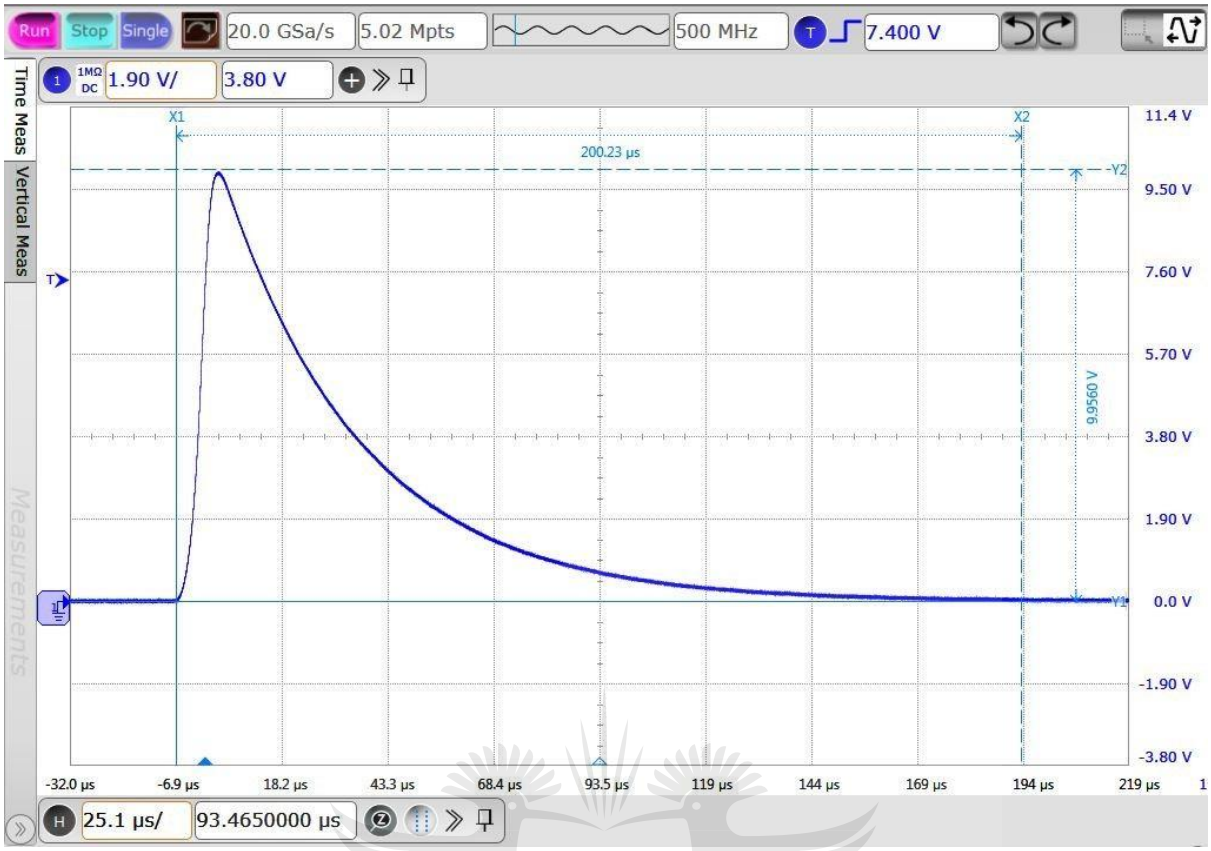

Figure 7.9: Experimentally measured IEC 61000-4-5 switch-induced ETO

7.3.1.4 Experiment 4: Determining the Response of the SJTC HE to Switching ETO Voltage Signal in the Absence and Presence of TVS Device(S)

Figure 7.10 presents the response of the HE without the protection element implemented, whereas Figure 7.11 presents the response of the HE with the protection elements implemented. The spike in Figure 7.10 is the IEC 61000-4-5 switch-induced ETO, presented in Figure 7.9, superimposed into a sine signal carrying line between the voltage source and the equivalent circuit of the HE. Since ETOs are random events, the position of the spike may differ per cycle.

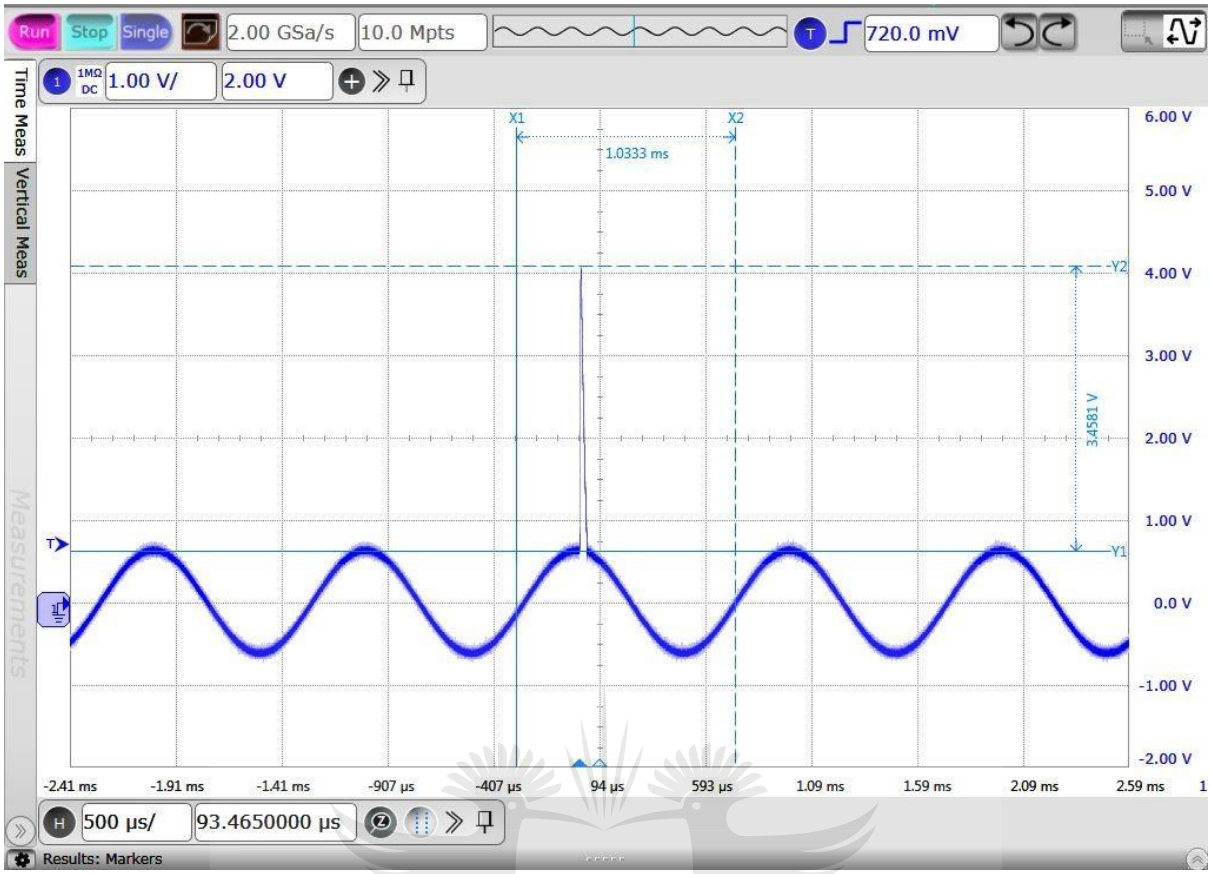

Figure 7.10: Response of the SJTC HE equivalent circuit without the protection element implemented

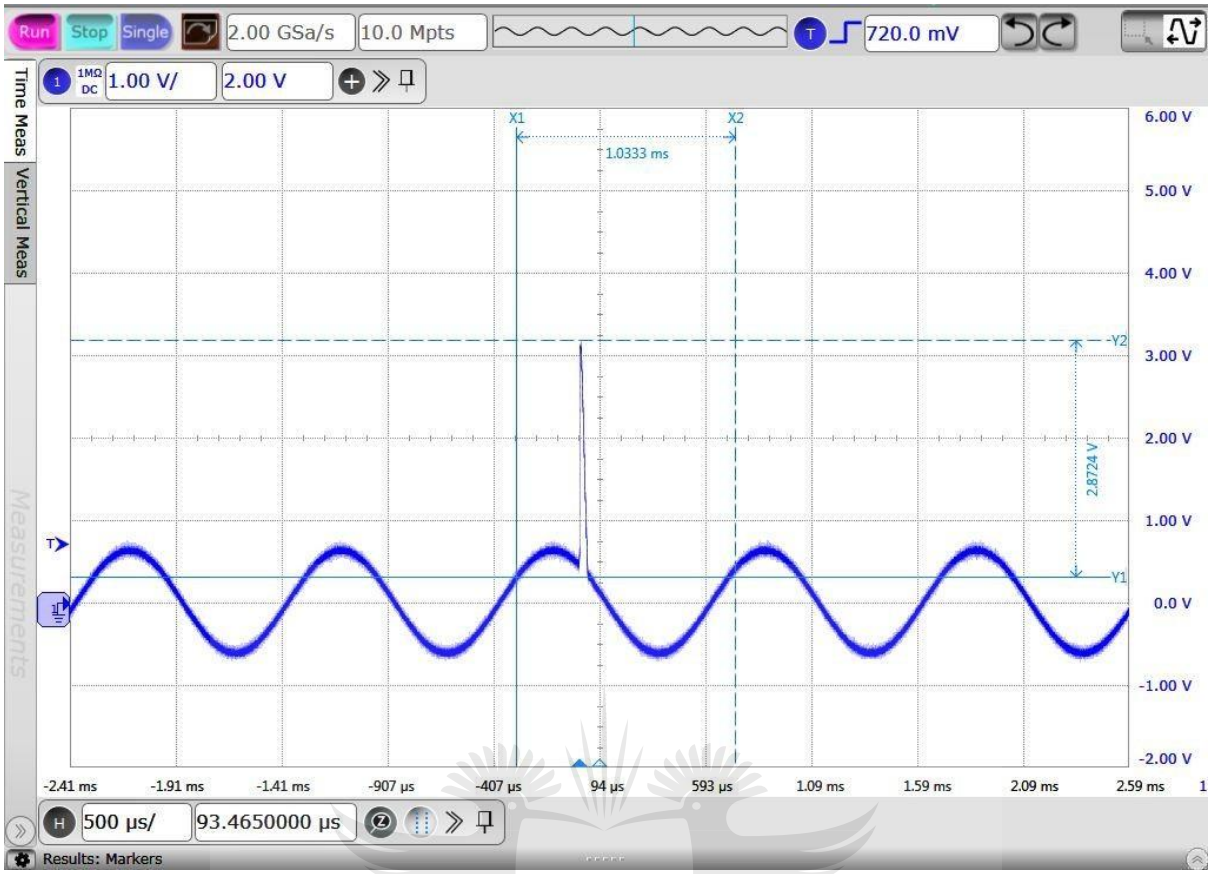

Figure 7.11: Response of the SJTC HE equivalent circuit with the protection element implemented

7.3.2 Discussion of Experimental Measurement Results

7.3.2.1 Experiment 1: Establishing the Electrical Characteristics of the TVS Devices

From the results obtained, the electrical characteristics of the test devices, it was observed that the Zener diode offers lower clamping characteristics than the MOV. Furthermore, the measured results correlate with the datasheets.

7.3.2.2 Experiment 2: Extraction of the RLC Components of the 5 mA UHF-pattern SJTC Input Circuit

From the measurements obtained from the validation of the equivalent circuit of the SJTC HE, which are relatively close to the maximum permissible input current and voltage of the 5 mA UHF-pattern SJTC, it can be deduced that the extracted values of inductance and capacitance of the HE characterise the dynamic performance of the SJTC in question.

7.3.2.3 Experiment 4: Determining the Response of the SJTC HE to Switching ETO Voltage Signal in the Absence and Presence of TVS Device(s)

The results obtained (presented in Figure 7.10) for the response of the equivalent circuit of the HE without the protection element show that the transient signal reaches a maximum value with a magnitude higher than the safe operating margin of the HE; thus, if a real SJTC had been connected, the HE would possibly be destroyed by the ETO signal superimposed on the line. This shows that a protection circuit must be implemented.

For the response of the equivalent circuit of the HE with the protection element, it can be seen, by comparing the response of the HE in Figure 7.10 with the one in Figure 7.11, that the protection circuit lowers the maximum value of the ETO signal. However, it is still higher than the safe operating margins of the SJTC and would still possibly damage the HE. Therefore, alternative methods such as implementing protection circuits on the sub-volt level must be considered. The MOV used in this work has a higher turn-on voltage, and even when used with a Zener diode in a multi-stage protection circuit, the Zener diode kept the voltage at a lower level than the turn-on voltage level of this particular MOV model tested; therefore, the MOV remain in the "off" state.

7.4 Conclusions

This chapter presented the results and findings of this research project. The mathematical models of the standard ETO sources used in this work and the response (current, voltage and power dissipation) of the HE of a 5 mA rated SJTC were developed and presented as part of the verification of the simulation models. The results obtained indicated close agreement between the simulation and mathematical models and for this reason it was assumed that the simulation and mathematical models for *Case 1* and *Case 2* would follow a similar trend. Therefore, only simulation models were considered for these cases. The experimental measurement results were also presented.

CHAPTER 8: CONCLUSIONS AND RECOMMENDATIONS

8.1 Introduction

NMISA keeps, develops and maintains high-accuracy precision AC-DC transfer measurement standards, which ensure realisation and traceability of the SI units for AC current, voltage and power through calibration services. Thermal converters, which are the key components in the AC-DC transfer measurement system, are susceptible to damage or destruction from ETOs, which may result from internal system operation or from human error. ETOs are inherent to electrical or electronic systems, especially those that rely on semiconductor components. However, the subject has been under study since the mid-1900s and protection solutions in the form of techniques (such as clamp-type) and components (such as TVS devices) have been developed. The idea behind this research project was to conduct a research study to identify the most likely sources of ETOs and develop a conceptual ETO protection solution through mathematical and simulation analysis supported by a range of experimental tests.

This chapter presents a general summary of the dissertation.

8.2 Summary of Research Findings

Firstly, it can be established through the literature study conducted during this study that ETO problems (discussed in this work) in the AC-DC transfer measurement systems have not been addressed before this study.

A mathematical model representing the temperature distribution along an HE of the SJTC was developed using the heat equation and the boundary conditions.

The mathematical models for the IEC 61000-4-5 switching and IEC 61000-4-2 ESD standard ETO sources were developed and validated using simulation models.

PSpice simulation models were developed and analysed for when the TOPDs were implemented individually, and for when these were simultaneously integrated into a multi-stage protection element.

The following experimental measurements were also performed as part of this work scope:

- Electrical characteristics of the TVS devices used in this work were established using a DC signal from a calibrator output.
- Using an LCR meter, the RLC components of the 5 mA nominal current rated SJTC were extracted in order to build an equivalent circuit of the SJTC HE.
- A switch-induced ETO signal was created using the arbitrary function of the waveform generator.
- The response of the equivalent circuit representing the dynamic performance of the SJTC to switch-induced ETO signal was determined for the absence and presence of TVS device(s).

8.2.1 Simulation Results

8.2.1.1 *Case 1* Simulation Results

The results indicate that the HE has a greater possibility of being damaged if an ETO event (switch- or ESD-induced) leads to its signal being coupled onto the measurement system composed of the sine-wave signal source connected to the HE of the 5 mA nominal current rated UHF-pattern SJTC. Therefore, protection devices or circuits should be implemented across the HE to ensure that harmful ETO signals are diverted away from the HE.

8.2.1.2 *Case 2* Simulation Results

The results indicate that implementation of protection device(s) across the HE has a greater possibility of protecting the HE against ETOs discussed in this work. Implementing both TVS devices simultaneously is a much better approach than individual implementation, and this can be supported by the results obtained. As expected in the model behaviour, the MOV offers better current conduction and power dissipation than the Zener diode, but when used together in a multi-stage circuit, they offer much better current and power dissipation than when used individually. However, the protection devices used in this work cannot protect the 5 mA nominal current rated UHF-pattern SJTC against the ETOs discussed. This is because the safe power operating margins of this SJTC are in the milliwatt range, which is very low and not enough to turn on the TVS devices considered.

ETOs used in this work are burst signals, which means they eventually decay to zero. The results also indicate that the magnitudes of the electrical parameters on the HE return to normal operating margins once the ETO dies out. This shows that implementing a protection device that can remove the ETO signal from the HE normal operating signal precisely will not interfere with the measurement system. Therefore, the protection circuit should be further improved.

8.2.2 Experimental Measurement Results

The experimentally measured results obtained for the response of the equivalent circuit of the HE without the protection element show that the transient signal reaches higher values, which have magnitudes greater than the input ratings and could possibly destroy the HE. This shows that a protection circuit must be implemented.

For the response of the equivalent circuit of the HE with the protection element, the results show that implementation of the protection devices has the potential of protecting the HE against ETOs. However, the protection level offered is still higher than the safe operating margins of the SJTC and would still possibly damage the HE. Therefore, alternative methods such as implementing protection circuits on the sub-volt level must be considered. The results for the response when the MOV was implemented as the protection device were not included, since the MOV used in this work has a higher turn-on voltage, and even when used with a Zener diode in a multi-stage protection circuit, the Zener diode keeps the voltage to a level that is lower than the turn-on voltage level of this MOV. The MOV never turned on.

8.3 General Conclusions

This dissertation presented the literature review on electrical metrology, transient overloads (overcurrent and overvoltage) and transient overload protection devices. ETOs in the AC-DC transfer measurement system were identified, as were possible protection or mitigation techniques and devices. The study indicated the potential to develop a working hardware prototype as a protection measure against ETOs in the AC-DC transfer measurement system. A conceptual TOPD circuit for AC-DC transfer measurement system was implemented and the solution was validated through mathematical and simulation models, and experimental measurement analyses. The study also established the effect of TOPD circuit on the performance of the AC-DC transfer measurement system.

8.4 Recommendation for Future Research

Since the SJTC used in this work has very low ratings, a typical protection device capable of protecting the SJTC against IEC 61000-4-5 standard ETO must have slightly more than one-volt clamping voltage to be able to turn on and retain that voltage level. However, commercial TVS devices (such as the Zener diode and MOV) with such low-value parameters do not exist. The Zener diode has the lowest clamping voltage (approximately 2.4 V), lower than that of the MOV, which is still high for a 5 mA nominal current rated SJTC. Therefore, it is recommended that other TOPD alternatives be considered to offer better and non-discrete protection. Furthermore, the development and improvement of the equivalent circuit models representing the TVS devices should be considered. Lastly, it is recommended that a working and non-discrete hardware transient overload protection circuit be developed and integrated into the AC-DC transfer measurement system to ensure the safety of the AC-DC transfer measurement standards and the quality of the AC-DC difference measurements.

LIST OF REFERENCES

[1] T. E. Kgakatsi, E. Golovins, J. Venter, and D. V. Nicolae, "Protection against transient overvoltage in precision AC-DC transfer measurement system," in *Fifth Conference on Sensors, MEMS, and Electro-Optic Systems.*, vol. 11043, 2019.

[2] "IEEE recommended practice on characterization of surges in low-voltage (1000 V and less) AC power circuits," *IEEE Std C62.41.2-2002*. New York, 2003.

[3] "IEEE guide for the application of surge-protective devices for use on the load side of service equipment in low-voltage (1000 V or less, 50 Hz or 60Hz) AC power circuits," *IEEE Std C62.72-2016*. 2016.

[4] "Electromagnetic compatibility (EMC) Part 4-2: Testing and measurement techniques — Electrostatic discharge immunity test." SABS Standards Division, Pretoria, 2009.

[5] B. G. Streetman and S. Banerjee, "Solid state electronic devices," in *Prentice Hall series in solid state physical electronics*, 7th ed., Essex, England: Pearson Education Limited, pp. 179–276, 2016.

[6] "DC low frequency and radio frequency." [Online]. Available: http://www.nmisa.org/technical/electricity-and-magnetism/Pages/Radio-Frequency-and-DC-Low-Frequency.aspx.

[7] T. E. Lipe, "Operations and reference manual for the NIST automated AC-DC calibration systems and software," *NIST Special Publication 250-61*, 2004.

[8] "Fluke 792A AC/DC transfer standard Instruction Manual." 1990.

[9] H. Fujiki, Y. Amagai, and H. Sasaki, "Development of thin-film multi-junction thermal converters - Establishing metrological traceability system for AC voltage standard," *Synth. English Ed.*, vol. 8, no. 3, pp. 113–137, 2015.

[10] BIPM, "The International System of Units (SI)," 2019. [Online]. Available: https://www.bipm.org/utils/common/pdf/si-brochure/SI-Brochure-9-EN.pdf.

[11] A. H. Silcocks, "Measurement of a.c. values," in *Electronics Testing & Measurement*, Palgrave, London: Macmillan Engineering Evaluations, pp. 109–114, 1972.

[12] F. L. Hermach, “Thermal converters as AC-DC transfer standards for current and voltage measurements at audio frequencies,” *J. Res. Natl. Bur. Stand. (1934).*, vol. 48, no. 2, pp. 121–138, 1952.

[13] B. D. Inglis, “Standards for AC-DC transfer,” *Metrologia*, vol. 29, no. 2, pp. 191–199, 1992.

[14] H. Handler, “A hybrid circuit RMS converter,” in *1971 IEEE International Solid-State Circuits Conference. Digest of Technical Papers*, pp. 190–191, 1971.

[15] J. R. Kinard, T. E. Lipe, and E. S. Williams, “Automated thermal voltage converter intercomparisons,” in *Proc. IEEE*, vol. 74, no. 1, pp. 105-107, Jan. 1986.

[16] M. Klonz, “Current developments in accurate AC-DC transfer measurements,” in *IEEE Trans. Instrum. Meas.*, vol. 44, no. 2, pp. 363-366, April 1995.

[17] Thomas F. Wunsch, J. R. Kinard, R. R. Manginell, T. E. Lipe, O. P. Solomon, and K. C. Jungling, “Recent advances in AC-DC transfer measurements using thin-film thermal converters,” in *Proc., Measurement Science Conference*, pp. 1–11, 2001.

[18] Fluke, “Design and evaluation of the 792A AC / DC,” *Application Note A-ENG-N Rev. B*, 2000.

[19] F. L. Hermach, “AC-DC comparators for audio-frequency current and voltage measurements of high accuracy,” *IEEE Trans. Instrum. Meas.*, vol. IM–25, no. 4, pp. 489–494, 1976.

[20] D. Inglis, “Electrical metrology,” *NIST/SIM Metrology School*, 2013. [Online]. Available: https://www.nist.gov/sites/default/files/documents/iaao/NIST_SIM-web-vsn.pdf. [Accessed: 29-Jul-2019].

[21] R. S. M. Ali, “Comparison between two different designs in the AC voltage measurement,” *Meas. J. Int. Meas. Confed.*, vol. 44, no. 9, pp. 1539–1542, 2011.

[22] “Introduction to AC-DC transfer standards,” *Researches of the Electrotechnical Laboratory No.989*. [Online]. Available: https://pdfs.semanticscholar.org/cdd5/0ec4cfd5cf5c6109b63ef9297e90004a218d.pdf. [Accessed: 01 Aug 2019].

[23] D. V. Nicolae and E. Golovins, “Characterization and modeling of an RMS-DC solid-state thermal converter,” in *2016 International Semiconductor Conference (CAS)*, pp. 113–116, 2016.

[24] T. E. Lipe, “50-Ω multijunction thermal converters on fused silica substrates,” in *CPEM Digest (Conference on Precision Electromagnetic Measurements)*, pp. 44-45, 2014.

[25] F. Capell, “Solid state sensor based AC voltage metrology,” in *1988. IMTC-88. 5th IEEE Instrumentation and Measurement Technology Conference*, pp. 334, 1988.

[26] D. Matson, “Using a linear thermal transfer standard for high precision AC/DC transfers,” in *Conference on Precision Electromagnetic Measurements*, pp. 64–65, 1990.

[27] “A guide for establishing primary AC-DC transfer standard using ET2001 ADS system.” Nano-Electronics Research Institute/AIST, pp. 8–17, 2007.

[28] NMISA, “Procedure for calibration of AC-DC voltage transfer standards,” DCLF\U-0005 Rev. 12, 2018.

[29] NMISA, “Procedure for calibration of AC-DC current transfer standards,” DCLF\I-0004 Rev. 7A, 2018.

[30] A. K. Govil, S. Ahmad, B. Pal, and P. C. Kothari, “Development of an automated AC-DC transfer measurement system for voltage and current at low frequencies,” *CPEM Dig. Conference Precis. Electromagn. Meas.*, pp. 590–591, 2008.

[31] F. L. Hermach and E. S. Williams, “Thermal converters for audio-frequency voltage measurements of high accuracy,” *IEEE Trans. Instrum. Meas.*, vol. 15, no. 4, pp. 260–268, 1966.

[32] “EL-1000 series thermal converters substantially reduce AC/DC transfer errors and produce a flat frequency response curve up to 100 MHz.” [Online]. Available: http://www.besttech.com/pressrelease.htm.

[33] A. Haroutunian, M. Halawa, A. Hassan, R. Attyia, and H. A. Mageed, “Comparison of the technical performance for different designs of single junction thermal converters,” in *CPEM Digest (Conference on Precision Electromagnetic Measurements)*, pp. 246–

247, 2008.

[34] V. Bubanja, “The AC-DC difference of single-junction thermal converters,” *J. Eng. Math.*, vol. 38, no. 1, pp. 33–50, 2000.

[35] C. M. Jha *et al.*, “In-chip device-layer thermal isolation of MEMS resonator for lower power budget,” in *Proceedings of IMECE2006*, pp. 1–7, 2006.

[36] N. Lobontiu, “Fluid and thermal systems,” in *System Dynamics for Engineering Students*, Burlington, MA: Elsevier Elsevier Inc., pp. 151–203, 2010.

[37] F. C. Widdis, “The theory of Peltier- and Thomson-effect errors in thermal a.c.-d.c. transfer devices,” *Proc. IEE Part C Monogr.*, vol. 109, no. 16, pp. 328–334, Jun. 1962.

[38] H. Sasaki, K. Takahashi, B. D. Inglis, and M. Klonz, “A numerical simulation of thermoelectric effects in single-junction thermal converters,” *IEEE Trans. Instrum. Meas.*, vol. 48, no. 2, pp. 408–411, 1999.

[39] I. Laird and D. D. C. Lu, “SPICE steady state modelling of thermoelectric generators involving the Thomson effect,” in *ECON 2011 - 37th Annual Conference of the IEEE Industrial Electronics Society*, pp. 1584–1589, 2011.

[40] “IEEE guide on the surge environment in low-voltage (1000 V and less) AC power circuits,” *in IEEE Std C62.41.1-2002*, 2003.

[41] V. Radulovic and S. Skuletic, “Influence of combination wave generator’s current undershoot on overvoltage protective characteristics,” *IEEE Trans. Power Deliv.*, vol. 26, no. 1, pp. 152–160, 2011.

[42] S. Marum, W. Kemper, Y. Y. Lin, and P. Barker, “Characterizing devices using the IEC 61000-4-5 surge stress,” in *Electrical Overstress/Electrostatic Discharge Symposium Proceedings*, pp. 1-9, 2012.

[43] M. H. J. Bollen, E. Styvaktakis, and I. Y. H. Gu, “Categorization and analysis of power system transients,” *IEEE Trans. Power Deliv.*, vol. 20, no. 3, pp. 2298–2306, 2005.

[44] M. Bafleur, F. Caignet, and N. Nolhier, “ESD standards: From component to system,” in *ESD Protection Methodologies: From Component to System*, 1st ed., Kidlington,

Oxford: ISTE Press - Elsevier, pp. 1–19, 2017.

[45] K. Verhaege, "Component level ESD testing," *Microelectron. Reliab.*, vol. 38, no. 1, pp. 115–128, Feb. 1998.

[46] A. Z. H. Wang, "ESD test models," in *On-Chip ESD Protection for Integrated Circuits*, Boston, MA: Springer, pp. 11–34, 2002.

[47] K. Verhaege *et al.*, "Analysis of HBM ESD testers and specifications using a fourth-order lumped element model," *Qual. Reliab. Eng. Int.*, vol. 10, no. 4, pp. 325–334, 1994.

[48] T. J. Maloney, "HBM tester waveforms, equivalent circuits, and socket capacitance," *Microelectron. Reliab.*, vol. 53, no. 2, pp. 184–189, Feb. 2013.

[49] O. Neacsu, O. Beniuga, S. Ursache, and M. Paulet, "Modelling and analysis the current pulse associated with electrostatic discharges," in *EPE 2012 - Proceedings of the 2012 International Conference and Exposition on Electrical and Power Engineering*, pp. 585–590, 2012.

[50] "The prevention and control of electrostatic discharge," *Application Note AN-40-005 Rev.: A*, 2015. [Online]. Available: https://www.minicircuits.com/app/AN40-005.pdf.

[51] A. A. Barna and D. Horelick, "A simple diode model including conductivity modulation," in *IEEE Trans. Circuit Theory*, vol. 18, no. 2, pp. 233-240, March 1971.

[52] R. B. Fair and H. W. Wivell, "Zener and avalanche breakdown in As-implanted low-voltage Si n-p junctions," *1975 International Electron Devices Meeting*, pp. 455-458, 1976.

[53] R. Chundru *et al.*, "An evaluation of TVS devices for ESD protection," in *2011 IEEE International Symposium on Electromagnetic Compatibility*, pp. 62–67, 2011.

[54] "AND8308/D - Interpretation of datasheet parameters for ESD devices," 2016.

[55] S. James, "Investigation of surge propagation in transient voltage surge suppressors and experimental verification," University of Waikato Copyright, 2014.

[56] "Transient voltage suppression diode.," *Technical Note 4048*, 2017. [Online]. Available: http://www.cooperindustries.com/content/dam/public/bussmann/Electronics/Resources

/technical-literature/Circuit Protection/BUS_Elx_App_Notes_TVSA.pdf.

[57] Q. Huang and G. Feng, “Impact of parasitic inductance on effectiveness of TVS diodes,” in *IEEE International Symposium on Electromagnetic Compatibility*, pp. 667–681, 2013.

[58] J. Attia, *Electronics and circuit analysis using MATLAB*. 2010.

[59] E. Lazarescu, C. Rimescu, F. M. Frigura-Iliasa, L. Dolga, H. E. Filipescu, and A. A. Anghel, “CAD project of a class D surge arrester module for domestic and residential low voltage applications,” in *2018 19th International Scientific Conference on Electric Power Engineering, EPE 2018 - Proceedings*, pp. 1-4, 2018.

[60] “Littelfuse varistors - Basic properties, terminology and theory,” *Application Note AN9767.1*, 1999. [Online]. Available: https://www.littelfuse.com/~/media/electronics_technical/application_notes/varistors/littelfuse_varistors_basic_properties_terminology_and_theory_application_note.pdf.

[61] M. Abdel-Salam, N. A. Ahmed, and I. S. Elhamd, “Varistor as a surge protection device for electronic equipments,” in *Proceedings of the IEEE International Conference on Industrial Technology*, vol. 2, pp. 688–694, 2004.

[62] “Transient suppression devices and principles,” *Application Note AN9768*, 1998. [Online]. Available: https://www.littelfuse.com/~/media/electronics_technical/application_notes/varistors/littelfuse_transient_suppression_devices_and_principles_application_note.pdf.

[63] S. E. Ruckman, “Electrical circuits for protection against surge overvoltage of transients,” U. S. Patent 4,571,656, 1986.

[64] R. B. Standler, “Passive overvoltage protection devices, especially for protection of computer equipment connected to data lines,” U. S. Patent 4,586,104, 1986.

[65] K. Casey, “Linear low capacitance overvoltage protection circuit,” U. S. Patent 7,515,391 B2, 2009.

[66] Best Products Limited, “Vacuo junction tubes.” [Online]. Available: http://besttech.com/index.htm.

[67] V. N. Zachovalova, S. Maslan, M. Sira, and J. Streit, “Development of primary standard for ac-dc current transfer difference,” in *CPEM 2016 - Conference on Precision Electromagnetic Measurements, Conference Digest*, pp. 1–2, 2016.

[68] M. Halawa and N. Al-Rashid, “Performance of single junction thermal voltage converter (SJTVC) at 1 MHz via equivalent electrical circuit simulation,” in *UKSim2010 - UKSim 12th International Conference on Computer Modelling and Simulation*, pp. 631–636, 2010.

[69] T. S. Saees, M. Halawa, I. A. Elrahman, and A. S. Eldin, “Electrical modeling and simulation of AC-DC thermal transfer devices to investigate the errors sources,” in *CPEM 2018 - Conference on Precision Electromagnetic Measurements*, pp. 1–2, 2018.

[70] C. Christopoulos, “Electrical circuit components,” in *Principles and Techniques of Electromagnetic Compatibility*, 2nd ed., Boca Raton, United States of America: CRC Press, pp. 55–76, 2007.

[71] Best Technology International, “Insulated UHF-pattern vacuo-junctions.” [Online]. Available: http://besttech.com/catalog5.htm.

[72] “Diode Equivalent Circuit.” [Online]. Available: http://puspc.com/oamr/wp-content/uploads/2013/10/ElectronicsI_partI-II.pdf.

Appendix A: Solution for the Second-order Non-homogeneous Differential Equation Describing the Temperature Distribution in a Single-junction Thermal Converter

For steady-state operations, the equation governing the temperature distribution, *T(x)*, of a HE of the SJTC is given by:

$$A \cdot k \cdot \frac{d^2T(x)}{dx^2} - \alpha_T \cdot I \cdot \frac{dT(x)}{dx} + \frac{I^2 \cdot \rho}{A} = 0 \tag{A.1}$$

Rearranging Eq. (A.1) results in an equation in the form of a second-order nonhomogeneous linear differential equation with the dependent variable being the position, instead of time:

$$\frac{d^2T(x)}{dx^2} - \frac{\alpha_T \cdot I}{A \cdot k} \cdot \frac{dT(x)}{dx} = -\frac{I^2 \cdot \rho}{A^2 \cdot k}. \tag{A.2}$$

Equation (A.2) is missing the term $\frac{d^0T(x)}{dx^0} = T(x)$; therefore, in order to obtain a general solution, it must be reduced in a first-order linear equation and be solved using the integrating factor method.

Now, let $\frac{dT(x)}{dx} = u(x)$, then $\frac{d^2T(x)}{dx^2} = \frac{du(x)}{dx}$, thus, Eq. (A.2) can be expressed in terms of *u* rather than *T*:

$$\frac{du(x)}{dx} - \frac{\alpha_T \cdot I}{A \cdot k} \cdot u(x) = -\frac{I^2 \cdot \rho}{A^2 \cdot k} \tag{A.3}$$

with $p(x) = -\frac{\alpha_T \cdot I}{A \cdot k}$ and $g(x) = -\frac{I^2 \cdot \rho}{A^2 \cdot k}$.

The integrating factor $\mu_{IF}(x) = e^{\int p(x) \cdot dx} = e^{p(x) \cdot x}$.

Multiplying both sides of Eq. (A.3) with $\mu_{IF}(x)$:

$$e^{p(x) \cdot x} \cdot \frac{du(x)}{dx} + e^{p(x) \cdot x} \cdot p(x) \cdot u(x) = e^{p(x) \cdot x} \cdot g(x) \tag{A.4}$$

the left side of Eq. (A.4) is the product rule of differentiation,

$$e^{p(x) \cdot x} \cdot \frac{du(x)}{dx} + e^{p(x) \cdot x} \cdot p(x) \cdot u(x) = \frac{d\left(e^{p(x) \cdot x} \cdot u(x)\right)}{dx}$$

thus, replacing the left side of Eq. (A.4) with this product rule:

$$\frac{d\left(e^{p(x)\cdot x}\cdot u(x)\right)}{dx} = e^{p(x)\cdot x}\cdot g(x). \tag{A.5}$$

Integrating both sides of Eq. (A.5) and solving for *u(x)*:

$$u(x) = \frac{1}{e^{p(x)\cdot x}}\cdot \int e^{p(x)\cdot x}\cdot g(x)\cdot dx$$

$$u(x) = \frac{g(x)}{p(x)} + C_1\cdot e^{-p(x)\cdot x} \tag{A.6}$$

Since $\frac{dT(x)}{dx} = u(x)$, *T(x)* can be determined by integrating the right side of Eq. (A.6) with respect to *x*.

$$T(x) = \frac{g(x)}{p(x)}\cdot x - \frac{C_1}{p(x)}\cdot e^{-p(x)\cdot x} + C_2 \tag{A.7}$$

Substituting $p(x) = -\frac{\alpha_T\cdot I}{A\cdot k}$ and $(x) = -\frac{I^2\cdot \rho}{A^2\cdot k}$ into Eq. (A.7) gives the general solution of a second-order nonhomogeneous linear differential equation describing the temperature distribution of the HE of a SJTC assuming steady-state operation in the audio frequency range and no radiation heat losses:

$$T(x) = \frac{I\cdot\rho}{\alpha_T\cdot A}\cdot x + C_1\cdot\frac{A\cdot k}{\alpha_T\cdot I}\cdot e^{\frac{\alpha_T\cdot I}{A\cdot k}x} + C_2 \tag{A.8}$$

where $C_1 = \frac{T_0 - T_L + \frac{I\cdot\rho}{\alpha_T\cdot A}\cdot L}{\frac{A\cdot k}{\alpha_T\cdot I}\left(1-e^{\frac{\alpha_T\cdot I}{A\cdot k}\cdot L}\right)}$ and $C_2 = \frac{T_0\cdot e^{\frac{\alpha_T\cdot I}{A\cdot k}\cdot L} - T_L + \frac{I\cdot\rho}{\alpha_T\cdot A}\cdot L}{\left(1-e^{\frac{\alpha_T\cdot I}{A\cdot k}\cdot L}\right)}$ are the constants of integration found using the boundary conditions, $T(0) = T_0$ and $T(L) = T_L$, of the HE temperature distribution. Simplifying Eq. (A.8) further gives:

$$T(x) = T_0 + \frac{I\cdot\rho}{\alpha_T\cdot A}\cdot x - \left(T_0 + T_L - \frac{I\cdot\rho}{\alpha_T\cdot A}\cdot L\right)\cdot\left(\frac{1+e^{\frac{\alpha_T\cdot I}{A\cdot k}\cdot x}}{1-e^{\frac{\alpha_T\cdot I}{A\cdot k}\cdot L}}\right). \tag{A.9}$$

Appendix B: Vacuum Thermal Converter's Technical Information

Table B.1: UHF-pattern vacuo-junction thermal converter

Code No.	Range mA	Heater Resistance ohms ±10%	Couple Resistance ohms ±10%	O/C EMF ±12% mV	Maximum Permissible load	Self-Inductance µH	Self-Capacitance pF
U.1	5	90	8	7	250% of Nom.	0.026	0.3

Appendix C: Development of the Standard Waveforms Equations

Appendix C.1: IEC 610000-4-5 Standard

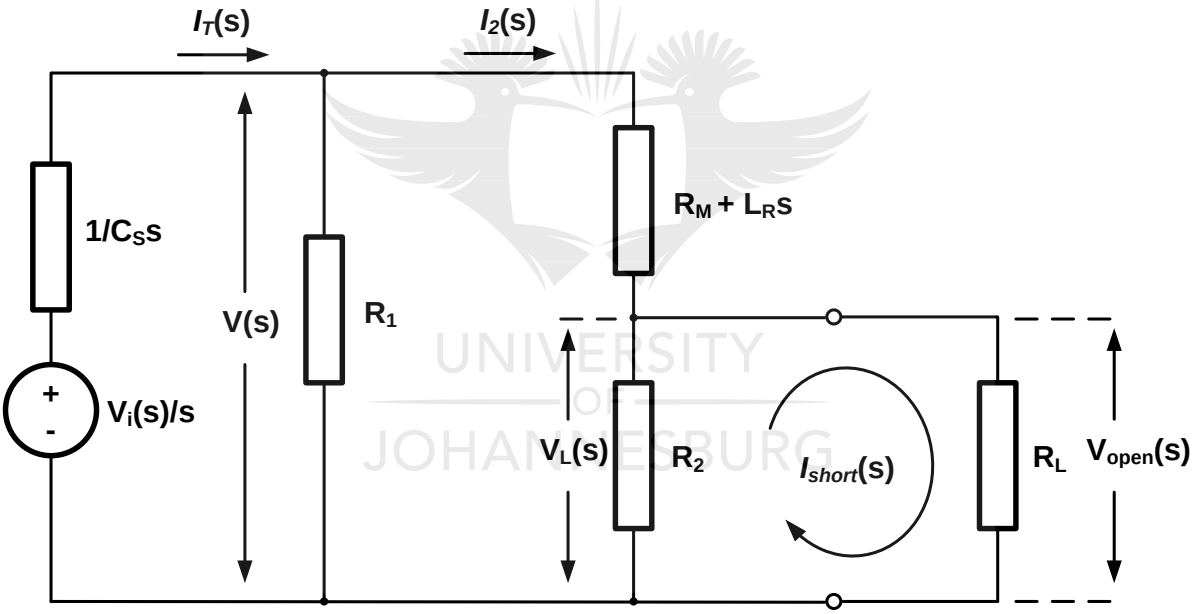

Figure C.1. 1: IEC 61000-4-5 standard combination wave generator circuit in the Laplace domain.

Model parameters: $\frac{V_i(s)}{s} = 530$ (V), $C_S = 8 \times 10^{-6}$ (F), $L_R = 7.2 \times 10^{-6}$ (H), $R_1 = 25$ (Ω), $R_2 = 12$ (Ω), $R_M = 1.11$ (Ω), $R_L = 10^{-3}$ (Ω) and $R_L = 10^{7}$ (Ω) for short circuit current and open circuit voltage measurements, respectively, and $t = 0{,}10^{-8} \ldots 10^{-4}$.

Total impedance:

$$Z_T(s) = \frac{\left(R_1+R_M+\frac{R_2R_L}{R_2+R_L}+L_RS\right)+R_1\left(R_M+\frac{R_2R_L}{R_2+R_L}+L_RS\right)(C_SS)}{(C_SS)\left(R_1+R_M+\frac{R_2R_L}{R_2+R_L}+L_RS\right)} \quad \text{(C.1.1)}$$

Development of the Short-circuit Current

Short-circuit current

The following equations were prepared in accordance with the modelling network shown in Figure C.1.1:

$$I_T(s) = \frac{V_i}{s}\frac{1}{Z_T(s)} \quad \text{(C.1.2)}$$

$$V(s) = I_T(s)\frac{R_1\left(R_M+\frac{R_2R_L}{R_2+R_L}+L_RS\right)}{R_1+R_M+\frac{R_2R_L}{R_2+R_L}+L_RS} \quad \text{(C.1.3)}$$

$$I_2(s) = \frac{V(s)}{R_M+\frac{R_2R_L}{R_2+R_L}+L_RS} \quad \text{(C.1.4)}$$

$$V_L(s) = I_2(s)\frac{R_2R_L}{R_2+R_L} \quad \text{(C.1.5)}$$

$$I_{short}(s) = \frac{V_L(s)}{R_L} \quad \text{(C.1.6)}$$

Taking the ILT of $I_{short}(s)$:

$$i_{short}(t) = 1.2\times10^{-17}e^{-(1.5\times10^5)t}$$

$$-\left(1.2\times10^{-17}\cos\left((1.1\times10^5)t\right)-6.8\times10^2\sin\left((1.1\times10^5)t\right)\right)e^{-(8.0\times10^4)t} \quad \text{(C.1.7)}$$

Development of the Open-circuit Voltage

Open-circuit voltage

$$I_T(s) = \frac{V_i}{s}\frac{1}{Z_T(s)} \quad \text{(C.1.8)}$$

$$V(s) = I_T(s)\frac{R_1\left(R_M+\frac{R_2R_L}{R_2+R_L}+L_RS\right)}{R_1+R_M+\frac{R_2R_L}{R_2+R_L}+L_RS} \quad \text{(C.1.9)}$$

$$I_2(s) = \frac{V(s)}{R_M+\frac{R_2R_L}{R_2+R_L}+L_RS} \quad \text{(C.1.10)}$$

$$V_L(s) = I_2(s)\frac{R_2R_L}{R_2+R_L} \quad \text{(C.1.11)}$$

$$V_{open}(s) = V_L(s) \quad \text{(C.1.12)}$$

Taking the ILT of $V_{open}(s)$:

$$v_{open}(t) = 1.4\times10^{-15}e^{-(1.8\times10^6)t}$$

$$-\left(1.4\times10^{-15}\cosh\left((9.0\times10^5)t\right) - 9.8\times10^2\sinh\left((9.0\times10^5)t\right)\right)e^{-(9.1\times10^5)t} \quad \text{(C.1.13)}$$

Appendix C.2: IEC 610000-4-2 Standard ESD Current

Development of the IEC 61000-4-2 Standard ESD Current

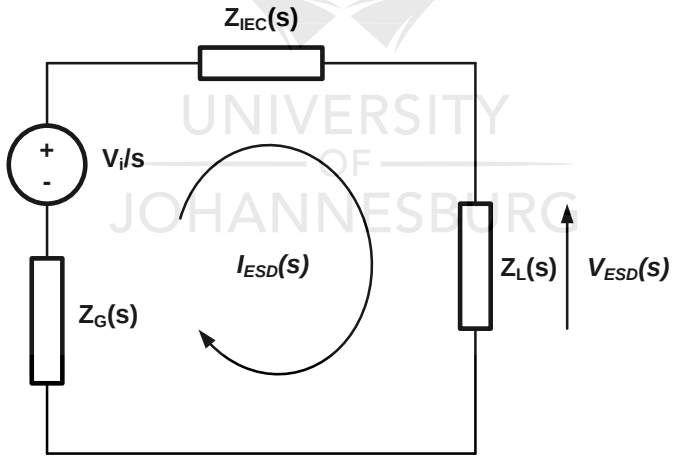

Figure C.2.1: IEC 61000-4-2 standard ESD current generator circuit.

Model parameters: $\frac{V_i(s)}{s} = 8\times10^3$ (V), $C_{IEC} = 150\times10^{-12}$ (F), $C_P = 2\times10^{-12}$ (F),

$C_G = 18\times10^{-12}$ (F), $L_{IEC} = 0.16\times10^{-6}$ (H), $L_G = 1.6\times10^{-6}$ (H), $R_{IEC} = 330$ (Ω),

$R_G = 40$ (Ω), $R_L = 2$ (Ω) for short circuit current measurements, and $t = 0{,}10^{-10}\,..\,10^{-7}$.

Analysing the circuit given in Figure C.2.1, the circuit impedance functions are

$$Z_G(s) = \frac{\frac{1}{C_G s}(R_G + L_G s)}{\frac{1}{C_G s} + R_G + L_G s} \tag{C.2.1}$$

$$Z_{IEC}(s) = \frac{1}{C_{IEC} \cdot s} + \frac{\frac{1}{C_{PS}} R_{IEC}}{\frac{1}{C_{PS}} + R_{IEC}} + L_{IEC} s \tag{C.2.2}$$

$$Z_L(s) = R_L \tag{C.2.3}$$

and the total impedance is

$$Z_T(s) = Z_G(s) + Z_{IEC}(s) + Z_L(s). \tag{C.2.4}$$

The IEC 61000-4-2 standard ESD current in s-domain is

$$I_{IEC}(s) = \frac{V_i(s)}{s} \frac{1}{Z_T(s)} \tag{C.2.5}$$

Taking the ILT of Equation (C.2.5) results in Eq. (C.2.6).

$$\begin{aligned} i_{IEC}(t) = {} & \left(23\sin\left((1.7 \times 10^9)t\right) - 22\cos\left((1.7 \times 10^9)t\right)\right) e^{-(6.7 \times 10^8)t} \\ & - \left(4.0\cos\left((1.6 \times 10^8)t\right) + 24\sin\left((1.6 \times 10^8)t\right)\right) e^{-(9.3 \times 10^7)t} \\ & + 26e^{-(1.9 \times 10^7)t} \end{aligned} \tag{C.2.6}$$

Appendix D: TVS Devices Datasheets

Appendix D.1: Zener Diode Datasheet

Table D.1: Zener diode specifications

Description	V_{Znom}	I_{ZT} for r_{zIT}		I_{ZK} for r_{zIK}		I_R and V_R		Part Number
	V	mA	Ω	Ω	mA	μA	V	1N4728A
Zener diode	3.3	76	< 10	< 400	1	< 100	1	

Appendix D.2: Metal-oxide Varistor Datasheet

Table D.2.1: 20D series metal-oxide varistor electrical specifications

Part No.	Maximum Allowable Voltage		Varistor Voltage (@ 1 mA)			Clamping Voltage @ Test Current (8/20 μs)		Maximum Energy (J)	Maximum Peak Current (8/20 μs)	Rated Power	Typical Capacitance (@ 1 kHz)
Device Marking	ACrms (V)	DC (V)	Min	Vb (Vdc)	Max	Vc (V)	Ip (A)	10/1000 μs	(A)	(W)	(pF)
20D180K	11	14	14.4	18	21.6	39	20	11.0	2000	0.2	40000

Table D.2.2: 20D series metal-oxide varistor dimensional specifications

Symbol	Model
	20D
D (max.)	25.0 mm
H (max.)	28.0 mm
W (±1.0)	10.0 mm
L (min.)	25.0 mm
d (±0.02)	1.0 mm

where D is the width of the varistor disc, H is the height of the varistor disc, W is the width between the centres of the cross-sectional areas of the two parallel varistor wires, L is the length of the varistor wires and d is the diameter of the diameter.

Appendix E: Program Code Used for Extraction of the RLC Components of the SJTC Input Circuit

```
clear, clc, clf
pkg load optim

%Load measurement data file
meas_data_file = 'impedance_data.xlsx';
[filetype sheets] = xlsfinfo(meas_data_file);

%Select sheet
prompt_msg = char(10);
for k = 1:size(sheets)(1)
  prompt_msg = cstrcat(prompt_msg,'[',num2str(k),'] ',sheets{k},char(10));
endfor
prompt_msg = cstrcat('Enter selection number :',prompt_msg,'=');
case_num = input(prompt_msg);

%Load measurement data
[numarr txtarr rawarr limits] = xlsread (meas_data_file,case_num);
f_meas = numarr(1:limits.numlimits(2,2)-1,1);
R_meas = numarr(1:limits.numlimits(2,2)-1,2);
X_meas = numarr(1:limits.numlimits(2,2)-1,3);
R = R_meas(1);
Z_meas = R_meas + j*X_meas;
[f_meas R_meas X_meas];

%Impedance model
Z_subf1 = @(x) R^2 + (2*pi*f_meas).^2*x(2)^4;
Z_subf2 = @(x) (R*x(1))^2 + (2*pi*f_meas*x(1)).^2*x(2)^4 - x(2)^2;
Z_subf3 = @(x) R^2 + (2*pi*f_meas).^2.*Z_subf2(x).^2;
Z_re = @(x) R*Z_subf1(x)./Z_subf3(x);
Z_im = @(x) 2*pi*f_meas.*(x(3)^2 - Z_subf1(x).*Z_subf2(x)./Z_subf3(x));
Z = @(x) Z_re(x) + j*Z_im(x);

%Objective function for optimisation
opt_fun = @(x) (Z(x)-Z_meas).*conj(Z(x)-Z_meas);

%Specify lower and upper bounds on searcheable parameters
C_rng = [1E-12 1E-8];
L_rng = [1E-10 1E-5];
Lc_rng = [1E-10 1E-5];
x_lb = sqrt([C_rng(1) L_rng(1) Lc_rng(1)]);
x_ub = sqrt([C_rng(2) L_rng(2) Lc_rng(2)]);
x0 = (x_lb + x_ub)/2;

%Solution using nonlinear LS fit
opts = optimset('MaxIter',1000,'TolFun',1E-9);
[x_fit, resnorm, residual, exitflag, output] = lsqnonlin(opt_fun,x0,x_lb,x_ub,opts);
```

```
[resnorm exitflag];

%Model function for plotting
df = (max(f_meas) - min(f_meas))/1000;
f = min(f_meas):df:max(f_meas);
Z_subf1 = @(x) R^2 + (2*pi*f).^2*x(2)^4;
Z_subf2 = @(x) (R*x(1))^2 + (2*pi*f*x(1)).^2*x(2)^4 - x(2)^2;
Z_subf3 = @(x) R^2 + (2*pi*f).^2.*Z_subf2(x).^2;
Z_re = @(x) R*Z_subf1(x)./Z_subf3(x);
Z_im = @(x) 2*pi*f.*(x(3)^2 - Z_subf1(x).*Z_subf2(x)./Z_subf3(x));
Z_mod = @(x) Z_re(x) + j*Z_im(x);

%Display of results in CLI
fprintf('\n%s\n','Extracted equivalent circuit parameters:')
fprintf('%s %.1f %s %.1f %s %.1f %s\n','C =',x_fit(1)^2*1E12,'pF, L =',x_fit(2)^2*1E9,'nH,
Lc =',x_fit(3)^2*1E9,'nH');

%Plot results
figure(1)
subplot(1,2,1)
semilogx(f_meas,real(Z_meas),'ko',f,real(Z_mod(x_fit)),'b-'), grid on
xlabel('{\itf}   (Hz)','FontSize',20)
ylabel('{\itR}   (\Omega)','FontSize',20)
title('AC RESISTANCE','FontSize',18)
leg = legend('Measured Data','Best Parameter Fit','Location','SouthOutside');
set(leg,'FontSize',14)
set(gca,'FontSize',14)
subplot(1,2,2)
semilogx(f_meas,imag(Z_meas),'ko',f,imag(Z_mod(x_fit)),'b-'), grid on
xlabel('{\itf}   (Hz)','FontSize',20)
ylabel('{\itX}   (\Omega)','FontSize',20)
title('REACTANCE','FontSize',18)
set(gca,'FontSize',14)
leg = legend('Measured Data','Best Parameter Fit','Location','SouthOutside');
set(leg,'FontSize',14)

pkg unload optim
```